

An Investigation of Phase-Change Effects During Rapid Compression Machine Experiments

Colin Banyon
Marquette University

Recommended Citation

Banyon, Colin, "An Investigation of Phase-Change Effects During Rapid Compression Machine Experiments" (2013). *Master's Theses (2009 -)*. Paper 224.
http://epublications.marquette.edu/theses_open/224

AN INVESTIGATION OF PHASE-CHANGE EFFECTS DURING RAPID COMPRESSION MACHINE EXPERIMENTS

by

Colin Banyon, B.S.M.E.

A Thesis submitted to the Faculty of the Graduate School,
Marquette University,
in Partial Fulfillment of the Requirements for
the Degree of Master of Science

Milwaukee, Wisconsin

December 2013

ABSTRACT

AN INVESTIGATION OF PHASE-CHANGE EFFECTS DURING RAPID COMPRESSION MACHINE EXPERIMENTS

Colin Banyon, B.S.M.E

Marquette University, 2013

Rapid compression machines (RCMs) are well characterized laboratory scale devices capable of achieving internal combustion (IC) engine relevant thermodynamic environments. These machines are often used to collect ignition delay times as targets for gas-phase chemical kinetic fuel autoignition models. Modern RCMs utilize creviced piston(s) to improve charge homogeneity and allow for an adequate validation of detailed chemistry mechanisms against experiments using computationally efficient, homogeneous reactor models (HRMs).

Conventionally, experiments are preformed by introducing a premixed gas of fuel + oxidizer + diluent into the machine, which is compressed volumetrically via a piston. Experiments investigating low-vapor pressure fuels (e.g. diesels, biodiesels, jet fuels, etc.) and surrogates can be conducted by preheating both the charge as well as the machine. This method of fuel loading can lead to pre-test fuel pyrolysis as well as machine seal degradation. Under some conditions loading a fuel aerosol of finely atomized liquid droplets in an oxidizer + diluent bath gas (i.e. wet compression) has been suggested to extend the capabilities of RCM experiments to involatile fuels. This work investigates phase-change effects during RCM experiments, especially for aerosol-fueling conditions, while the methodology can be applied to gas-phase fuel experiments where fuel condensation can occur at the compressed conditions within the boundary layer region.

To facilitate this study a reduced-order, physics-based model is used. This work highlights important machine-scale influences not investigated in previous work, and provides additional detail concerning an aerosol RCM's capabilities and limitations. A transient formulation is developed for the multi-phase transport within the RCM reaction chamber as well as the flow to the piston crevice region during both the compression and delay periods. The goal of this work is threefold. First, an *a priori* knowledge of the stratification present under various conditions can help determine an optimum machine geometry so that discrepancies between experimental data sets and 0D kinetics simulations are minimized for involatile fuels. Second, the model is computationally tractable to prescribe heat loss rates to an HRM during simulations of experiments so that physical effects can be incorporated into simulations using detailed chemistry. Finally, heat loss rates that are prescribed to the HRM are only a function of machine geometry, and are independent of *ad hoc* and empirically derived fits that vary between facilities. Thus a more adequate comparison of data between RCM facilities and with existing literature can be made.

ACKNOWLEDGMENTS

Colin Banyon, B.S.M.E.

I would first like to thank my advisor Scott Goldsborough. His advice and insight have proved invaluable, and almost all of my research skills developed over the last five years can be attributed to his guidance. I am glad to have had the privilege of such a great mentor, and am glad to have gained a valued friend. I truly hope that we have the opportunity to collaborate as my skills grow, and as his projects progress.

Mike Johnson, Steve McConnell, Steve Ciatti, Will Church and Chris Kolodziej from the Argonne Energy Systems Division also have my thanks, both for technical guidance and invaluable words of wisdom.

I would also like to thank my thesis committee, John Borg, Jon Koch and Kyuil Kim for insight into this project in addition to providing a first class education during my time at Marquette University.

I would like to thank my fellow energy systems graduate students at Marquette, especially Alex Polley, Dan Sherwin and Hao Wang. These folks provided many things, but I am most appreciative for the late night company in the lab.

I would also like to thank Ben Gumieny for assistance with this as well as other projects I explored while at Marquette, but mostly for being an outstanding friend throughout my undergraduate and graduate studies and hopefully for much, much longer.

Finally, my Parents for always pushing me to achieve something better...

TABLE OF CONTENTS

Acknowledgments	i
List of Tables	v
List of Figures	ix
Nomenclature	x
1 Background	1
Introduction	1
Energy Conversion	3
Transportation Fuels	5
Internal Combustion Engines	8
Combustion Chemistry Models	12
Chemical Kinetic Mechanism Validation	14
Laminar Flames	16
Flow Reactors	17
Shock Tubes	18
Rapid Compression Machines	19
Thesis Outline	21
2 Rapid Compression Machines	23
Introduction	23
Historical Machine Design	25
Modern Rapid Compression Machines	27
Piston Trajectory Control and Seating	30
Suppression of Fluid Dynamics	32
Boundary Layer Growth	34
Heat Loss Modeling	35

Experimental Approaches	36
Physics-based Models	38
Involatile Fuel Experiments	40
Charge Pre-heating	41
Wet Compression	42
3 Phase-Change Modeling	45
Modeling Approach	45
Reaction Chamber	48
Governing Equations	48
Solution Scheme	51
Species and Energy Flux	55
Boundary Term	57
Pressure Equilibration	58
Dispersed Droplet Evaporation/Condensation	59
Governing Equations	59
Analytic Solutions	63
Piston Gap	64
Governing Equations	64
Gap Velocities	68
Convective Heat Transfer	69
Phase Change	70
Piston Crevice	72
Governing Equations	72
Fluid Shear	74
Convective Heat Transfer	75
Phase Change	76
4 RCM Aerosol Multizone Model Validation and Results	78
Validation Approach	78

Droplet Evaporation Model Validation	80
Detailed Validation Model	80
Single Stagnant Droplet Comparison	81
Wet Compression Comparison	84
Gas-phase Transport Validation	88
Validation Methodology	88
Validation Results	91
Single Component Fuel Results	95
5 Summary, Conclusions and Future Work	102
Summary	102
Conclusions	103
Future Work	104
Appendices	128
A Thermophysical and Transport Properties	129
Specific Heat	129
Energy	132
Equation of State	135
Viscosity	136
Thermal Conductivity	137
Diffusion Coefficient	138

LIST OF TABLES

2.1	Design features of a few rapid compression machines.	29
4.1	Conditions of each validation case for the RCM gas-phase processes.	89
4.2	RCM dimensions used in this study, as well as gas phase model validation. Lettered dimensions correspond to Figure 4.12.	90

LIST OF FIGURES

1.1	U.S. energy use by source and sector including efficiency losses. . . .	4
1.2	Distillation curves of popular fuels used in IC engines.	7
1.3	Mechanisms of transportation internal combustion (IC) engines. . .	8
1.4	Soot and NO _x production regimes of IC engines.	11
1.5	Experimental devices used for acquiring combustion chemistry tar- gets.	15
2.1	The affiliations of the world's RCMs tailored for chemical kinetics studies.	24
2.2	RCM related publications since 1995.	25
2.3	Photograph of the Falk RCM.	25
2.4	Schematic of a generic RCM.	28
2.5	A few creviced piston designs used in RCMs.	33
2.6	Schematic of the multi-zone modeling approach.	39
2.7	A mechanistic schematic of the wet compression process in RCM experiments.	42
3.1	A graphical representation of the MP-MZM communication with an HRM used to simulate detailed chemical kinetics.	46
3.2	A schematic of the reaction chamber computational mesh.	52
3.3	A schematic of the multi-phase flow through the piston gap.	66
3.4	A schematic of the multi-phase flow through the piston crevice. . .	73
4.1	Comaprison of an n-heptane droplet surface area histories for the current droplet evaporation model and the detailed model devel- oped by Zhu and Aggarwal, for a single stagnant droplet over a range of pressures.	81

4.2	Comparison of droplet surface temperature histories for the current droplet evaporation model and the detailed model developed by Zhu and Aggarwal, for a stagnant droplet over a range of pressures. . . .	81
4.3	Comparison of n-dodecane droplet surface area histories undergoing wet compression for the current vaporization model and that of Goldsborough et al. at two global equivalence ratios and a range of initial droplet diameters.	84
4.4	Comparison of n-dodecane droplet surface and far-field temperature histories undergoing wet compression for the current vaporization model and that of Goldsborough et al. at a global equivalence ratio of $\phi=1$ and a range of initial droplet diameters.	84
4.5	Comparison of n-dodecane droplet surface fuel fraction as a function of non-dimensional surface area, for droplets undergoing wet compression for the current vaporization model and that of Goldsborough et al. at a global equivalence ratio of $\phi=1$ and a range of initial droplet diameters.	84
4.6	Comparison of n-dodecane droplet far-field fuel fraction as a function of non-dimensional surface area, for droplets undergoing wet compression for the current vaporization model and that of Goldsborough et al. at a global equivalence ratio of $\phi=1$ and a range of initial droplet diameters.	84
4.7	Comparison of n-dodecane droplet surface area histories undergoing wet compression for the current vaporization model and that of Goldsborough et al. at varied global equivalence ratios.	87
4.8	Comparison of n-dodecane droplet surface temperature as a function of non-dimensional surface area, for droplets undergoing wet compression for the current vaporization model and that of Goldsborough et al. at varied global equivalence ratios.	87

4.9	Comparison of n-dodecane droplet far-field temperature as a function of non-dimensional surface area, for droplets undergoing wet compression for the current vaporization model and that of Goldsborough et al. at varied global equivalence ratios.	87
4.10	Comparison of n-dodecane droplet surface fuel mass fraction as a function of non-dimensional surface area, for droplets undergoing wet compression for the current vaporization model and that of Goldsborough et al. at varied global equivalence ratios.	88
4.11	Comparison of n-dodecane droplet far-field mass fraction as a function of non-dimensional surface area, for droplets undergoing wet compression for the current vaporization model and that of Goldsborough et al. at varied global equivalence ratios.	88
4.12	Schematic of key RCM dimensions at maximum compression, values used in this study as well as for gas phase model validation are available in table 4.2.	90
4.13	A comparison of pure N ₂ simulated pressure traces for the current MZM and a previous multi-zone formulation.	92
4.14	A comparison of a 0.6N ₂ /0.4Ar blend simulated pressure traces for the current MZM and a previous multi-zone formulation.	92
4.15	A comparison of case 2 simulated gas velocities in the piston gap and crevice for the current MZM and a previous multi-zone formulation.	93
4.16	A comparison of case 5 simulated gas velocities in the piston gap and crevice for the current MZM and a previous multi-zone formulation.	93
4.17	A comparison of simulated crevice mole fraction for the current MZM and a previous multi-zone formulation.	94
4.18	A comparison of case 2 simulated gas temperatures for the current MZM and a previous multi-zone formulation.	94
4.19	A comparison of case 5 simulated gas temperatures for the current MZM and a previous multi-zone formulation.	94

4.20	Simulated pressure traces for an n-dodecane $D_0 = 8 \mu\text{m}$ aerosol at $\phi = 0.0, 1.0$ and 2.0 initially at $P_0 = 1$ bar and $T_0 = 350$ K.	95
4.21	Simulated pressure traces for an n-hexadecane $D_0 = 8 \mu\text{m}$ aerosol at $\phi = 0.0, 1.0$ and 2.0 initially at $P_0 = 1$ bar and $T_0 = 350$ K.	95
4.22	Simulated temperatures for an n-dodecane $D_0 = 8 \mu\text{m}$ aerosol at $\phi = 1.0$ initially at $P_0 = 1$ bar and $T_0 = 350$ K.	96
4.23	Simulated temperatures for an n-hexadecane $D_0 = 8 \mu\text{m}$ aerosol at $\phi = 1.0$ initially at $P_0 = 1$ bar and $T_0 = 350$ K.	96
4.24	Simulated gas-phase equivalence ratios for an n-dodecane $D_0 = 8 \mu\text{m}$ aerosol at $\phi = 1.0$ initially at $P_0 = 1$ bar and $T_0 = 350$ K.	97
4.25	Simulated gas-phase equivalence ratios for an n-hexadecane $D_0 = 8 \mu\text{m}$ aerosol at $\phi = 1.0$ initially at $P_0 = 1$ bar and $T_0 = 350$ K.	97
4.26	Simulated reaction chamber non-dimensional temperature gradients for a $D_0 = 8 \mu\text{m}$ aerosol at $\phi = 0.0, 1.0$ and 2.0 initially at $P_0 = 1$ bar and $T_0 = 350$ K.	98
4.27	Simulated reaction chamber non-dimensional gas equivalence ratio gradients for a $D_0 = 8 \mu\text{m}$ aerosol at $\phi = 0.0, 1.0$ and 2.0 initially at $P_0 = 1$ bar and $T_0 = 350$ K.	98
4.28	Simulated reaction chamber thermal boundary layer thickness for a $D_0 = 8 \mu\text{m}$ aerosol at $\phi = 0.0, 1.0$ and 2.0 initially at $P_0 = 1$ bar and $T_0 = 350$ K.	99
4.29	Simulated reaction chamber compositional boundary layer thickness for a $D_0 = 8 \mu\text{m}$ aerosol at $\phi = 0.0, 1.0$ and 2.0 initially at $P_0 = 1$ bar and $T_0 = 350$ K.	99
4.30	Simulated gap and crevice liquid film thickness for a $D_0 = 8 \mu\text{m}$ aerosol at $\phi = 0.0, 1.0$ and 2.0 initially at $P_0 = 1$ bar and $T_0 = 350$ K.	100
A.1	A schematic of the multi-phase flow through the piston crevice.	131

NOMENCLATURE

Roman Symbols

A	area
B	bore
C_f	mean friction coefficient
C_p	constant pressure specific heat
C_v	constant volume specific heat
D	diameter
\mathcal{D}	diffusion coefficient
h	intensive enthalpy
h_{conv}	convection coefficient
Δh_{vap}	vaporization enthalpy
J	molar flow rate due to Fickian diffusion
k	thermal conductivity
LMTD	log-mean temperature difference
MW	molecular weight
N	number of liquid droplets
N_{sp}	number of species in the mixture
n	moles of molecules
Nu	Nusselt Number
P	pressure
Pr	Prandlt Number
Q	heat energy
q	heat flux
r	radius
Re	Reynolds Number
Sh	Sherwood Number
Stk	Stokes Number
T	temperature
t	time
U	internal energy
u	intensive internal energy
v	velocity
V	volume
W	work energy

Greek Symbols

γ	ratio of specific heats (i.e. c_p/c_v)
μ	viscosity
ξ	effective “radial” reaction chamber length scale
ζ	characteristic length
ρ	molar density
τ	fluid shear
χ	mole fraction

Subscripts

c	piston crevice zone
$char$	char
$cond$	conduction
$conv$	convection
d	droplet
ex	gap exit boundary
f	fuel
g	piston gap zone
in	gap inlet boundary
j	species number
jet	fluid jet
l	liquid
mix	mixture
n	computational mesh node number
PC	phase change
$pist$	piston
PR	pressure rezoning
r	reduced
RC	reaction chamber zone
rxn	reaction
s	surface
τ	fluid shear stress
v	vapor
$wall$	wall
x	cross-sectional

Chapter 1

Background

Introduction

This thesis investigates phase-change phenomena that occur during rapid compression machine (RCM) experiments. Rapid compression machines are laboratory devices that can create and maintain a high temperature and pressure environment, for a relatively long period of time (e.g. 100 ms). This environment is well-suited for investigations of a number of processes that affect the combustion of liquid fuels in internal combustion (IC) engines, including fuel spray dynamics [1–3], ignition assistance [4, 5], engine knock [6, 7], turbulent combustion [8, 9] and autoignition [10–13]. While RCMs have been used to investigate a wide variety of phenomena the study of autoignition of involatile fuels is complicated by phase-change effects. This work utilizes a computational approach to better understand these effects and thereby increase fidelity in fuel autoignition data acquired from experiments.

Autoignition data collected from RCM experiments are a prominent source of validation targets for chemical kinetic models that describe fuel pyrolysis and oxidation [14–17]. Chemical kinetic mechanisms are utilized toward the improvement of current, as well as the design of future IC engines by enabling the prediction of ignition timing, rate-of-heat-release (ROHR) and in-cylinder pollutant formation processes. The development of accurate predictive models has been earmarked as essential toward the development of clean, efficient, sustainable combustion technologies [18].

Conventional RCM experiments undertaken to investigate gas-phase

chemistry are typically limited to volatile fuels. For instance, studies have utilized hydrogen [19–21], natural gas-relevant species [22–24], small alkanes [25–28], gasoline surrogates [29–32] and small bio-derived species [33–35]. Typically only a model for heat loss to the reaction chamber walls and to the piston crevice during the experiment (e.g. [36]) is needed to adequately compare the chemical kinetic mechanism with RCM data. Experiments with involatile fuels such as diesel, biodiesel, and jet fuel relevant species are much more challenging, as these fuels must be vaporized before the test conditions are realized. In some cases pre-heating the charge and machine has been a successful method for pre-vaporization (e.g. [37]); however significant pre-heating of the fuel can lead to pyrolysis, while significant pre-heating of the machine can lead to seal degradation.

Recently, the “wet compression” fuel loading approach, which has been successful in shock tube experiments [38], has been suggested to extend the capabilities of RCM experiments to involatile fuels [39]. In this approach a finely atomized fuel aerosol in an oxidizer + diluent bath gas is loaded into the machine. During piston compression the fuel is vaporized and diffusively mixed on a time scale much faster than the decomposition/oxidation chemistry. Thus by the time the charge reaches the compressed temperature and pressure a well-mixed gas-phase experiment proceeds.

While “wet compression” has the potential to extend the capability of RCM experiments, new modeling techniques are needed to adequately compare collected data with chemical kinetic models. A predictive model is required in order to determine the droplet size required to achieve vaporization and mixing by maximum compression, for varying initial conditions so that experimental matrices are realizable. An improved heat loss model is also required to account for phase-change effects and gas-phase compositional stratification that may ensue within the reaction chamber. Such a model can also be used to determine the rates of heat loss to the reaction chamber surfaces and piston crevice while

simulating the chemistry of the experiment. Finally, since this is a novel fuel loading approach, a computational model can offer insight into the limitations and optimum design of an aerosol RCM (aRCM). The reduced-order, physics-based model developed in this work has the capability of satisfying all of these criteria.

This chapter begins with a look into the sources of energy utilized by the United States, and the particular role of petroleum based fuels in IC engines. Next a brief summary of liquid fuels is presented, followed by a short description of current and future IC engines used to convert the fuels' chemical energy into mechanical power. A short discussion of combustion chemistry models is then given highlighting their importance in future engine design, followed by techniques commonly utilized to develop and validate these models. The chapter ends with an overview of this manuscript.

Energy Conversion

A wide variety of engineering technologies have enabled the conversion of useful energy from a broad range of fuel sources or feedstocks [40]. A breakdown of current U.S. energy use by source and sector is shown in Figure 1.1. The combustion of fossil fuels (i.e. coal, natural gas and petroleum) presently provides the majority of consumed energy in the United States. The two largest sectors that make use of these fuels, electricity generation and transportation, are also the most inefficient at converting fuel to useful energy. These inefficiencies are attributed to first law thermal losses and second law restrictions during energy conversion, as well as the energy expended to mine, transport and refine raw fuel sources [41].

The large majority of past and present electricity generated in the United States has been from the combustion of coal in coal-fire power plants and natural

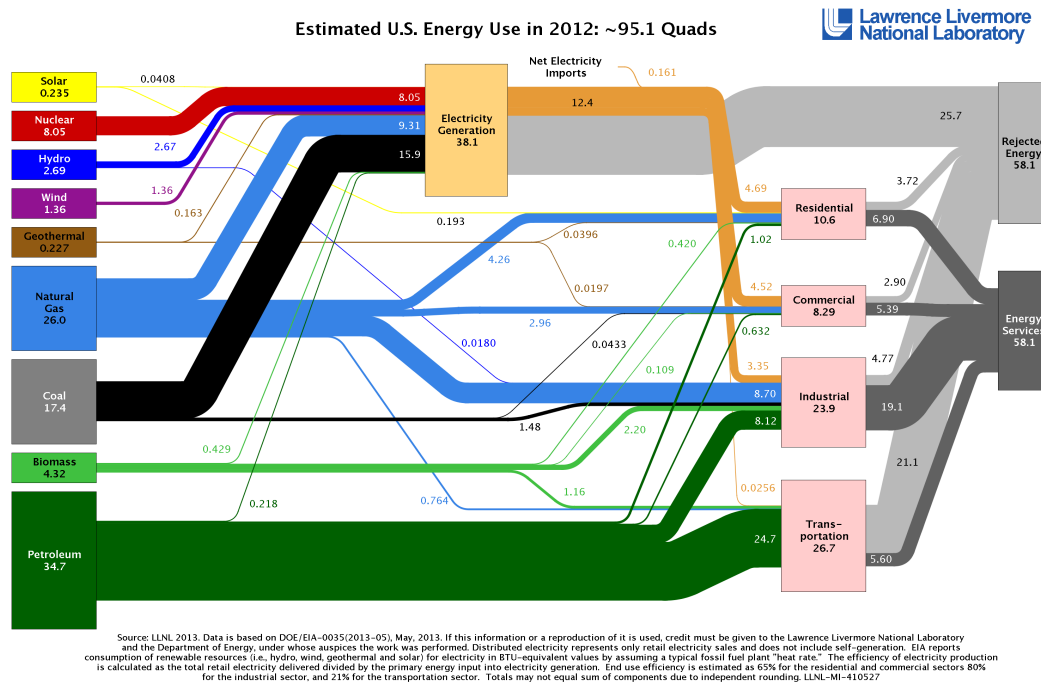


Figure 1.1: U.S. energy use by source and sector including efficiency losses. Figure reproduced from [42], courtesy of Lawrence Livermore National Laboratory.

gas in turbine engines [43]. The limited availability of these fuels in addition to the emission of toxic pollutants and greenhouse gasses such as NO_x , CO_2 , SO_2 and unburned hydrocarbons (i.e. PM, soot or black carbon) has motivated alternative fuels and technologies [41]. Within the last few decades other options have been explored for electricity generation, which include: nuclear fission of uranium, as well as more sustainable options such as the harnessing of natural wind, water and geothermal currents and solar radiation [40].

While stationary power plants have utilized a wide variety of energy conversion technologies and energy sources, the transportation industry has depended on the combustion of liquid fuels in IC engines [40]. Internal combustion engines are well-suited for transportation applications due to small size and low manufacturing cost, as well as the high power output achievable when utilizing energy-dense liquid fuels [44]. This trend is expected to continue in the future [18], even as competing technologies such as hydrogen fuel cells and electrical storage in batteries are developed [45]. The continued usefulness of the

IC engine has motivated a vast amount of research into the improvement of existing designs, with a focus on clean, efficient and sustainable technologies [18]. The fuels used in past and modern IC engines are generally petroleum derived gasoline and diesel, however the use of sustainable bio-derived additives and replacements are becoming more prevalent. The following section explores some of the commonly used and suggested fuels for IC engines.

Transportation Fuels

Real transportation fuels derived from petroleum are chemically complex consisting of thousands of species, which may vary from batch to batch [46]. During refining in the US about 45% of crude oil is converted to gasoline, 21% is converted to diesel and about 9% is converted to jet fuel [46]. Gasoline typically contains C4 to C10 species and is mainly composed of 40-80% alkanes (including normal alkanes and branched iso-alkanes), 15-40% aromatics, 5-20% alkenes and 1-10% cycloalkanes [47]. Diesel contains heavier C10 to C24 species mainly comprised of 25-50% alkanes, 20-40% cycloalkanes and 15-40% aromatics [48], which is a substantially higher concentration of cyclic structures than gasoline. Production jet fuels typically have a looser regulation and the spectrum of carbon lengths and structures can be much broader [49]. However, a recent study was conducted that surveyed the composition of jet fuels worldwide and an average structural composition of 58% alkanes, 21% cycloalkanes and 13% aromatics was found [50]. Other types of structures can exist in these fuels, however in small amounts. These real fuels are intractable to accurately characterize, and developing accurate combustion models for such real fuels is even more challenging.

In order to understand fuel chemistry, fuel surrogates are often used, where extensive work has been undertaken to develop these for petroleum derived

fuels [47–49, 51]. Surrogates are built using a few fuel-relevant species, for which the chemistry is well understood, by matching bulk host properties (e.g. fuel structure, octane/cetane rating, density, vapor pressure, etc.). The chemistry of the surrogate can then be experimentally investigated to gain insight into real fuel behavior (e.g. [29, 33, 52]).

Oxygenated biofuels do not consist of a broad range of species as is the case with petroleum derived fuels. Small alcohols (e.g. ethanol, propanol and butanol) can be derived from biological feedstock and used as a sustainable supplement to petro-fuels [53]. For instance, in the United States ethanol is manufactured from corn and is used as an additive to gasoline. There is much speculation, however, that bio-butanol may be a more suitable additive due to an increased energy density and mixing potential [53]. Fuels derived from organic feedstocks have also shown potential to replace petroleum derived fuels altogether. For instance, biodiesels generated from the transesterification of soybean, algae, rapeseed, camelina, cuphea and palm feedstock (among others) have been demonstrated to serve as additive-blends or complete replacements for petro-diesel [54]. Biodiesels typically consist of a few C16 to C18 methyl-esters, and work is ongoing to understand the oxidation chemistry of these species [55, 56]. The involatility of these fuels however, currently makes significant experimental progress towards a full understanding of their oxidation chemistry challenging and in some cases impossible.

Experimental investigations of the gas-phase oxidation of transportation relevant fuels and species can be difficult. Liquid fuels utilized by transportation IC engines and their surrogates consist of a large amount of involatile species, as is depicted by Figure 1.2. Conventional experiments used for acquiring validation targets for combustion chemistry models, as will be explored later in this chapter, typically require a gas-phase fuel + oxidizer + diluent to obtain meaningful data, whereby the important chemical processes are sufficiently developed from physical processes. This is usually achievable for gasoline

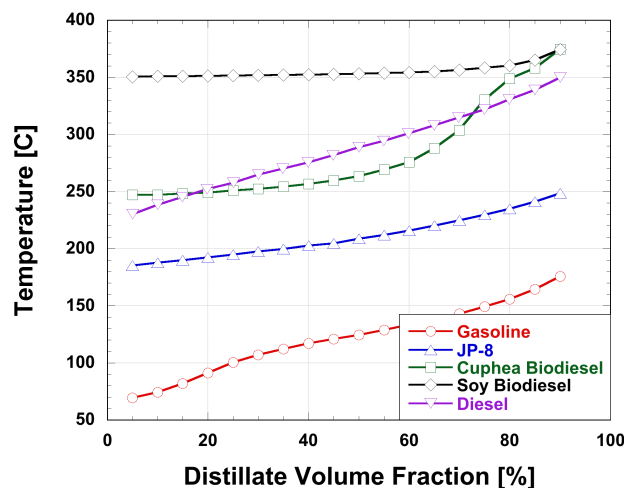


Figure 1.2: Distillation curves for popular fuels used in IC engines including gasoline, JP-8, biodiesel from cuphea and soy feedstock and petro-diesel. Original experimental data reproduced from [57–60], respectively.

surrogates and some gasolines as a high fuel partial pressure can be maintained in the gas phase with minimal pre-test fuel heating [29–32]. For diesel and jet fuels and their surrogates, which require pre-heating to higher temperatures, fuel decomposition may occur before even dilute gas-phase conditions exist.

While a fundamental understanding of the oxidation processes for transportation fuels can be challenging, modern IC engines use combustion strategies that can take advantage of fuel involatility. Flexible combustion strategies are also being developed that can make use of unconventional sustainable fuels in tandem with those derived from petroleum (e.g. [61]). As an understanding of the chemistry of liquid fuels is progressed, future designs will surely be capable of making an even greater use of fuel resources.

Internal Combustion Engines

Three modern combustion strategies for transportation IC engines are shown in Figure 1.3; spark ignition (SI), compression ignition (CI) and homogeneous charge compression ignition (HCCI). Over the past century SI and CI engines have been widely utilized with gasoline and diesel, respectively. In addition, within the last few decades advanced low-temperature combustion (LTC) strategies have been developed such as HCCI [62, 63], which may make use of multiple [64] or modified fuels [65]. Each of the three combustion strategies mentioned have strengths and unresolved challenges regarding engine efficiency, emission output and robustness over a range of operating conditions, and research is ongoing to resolve these.

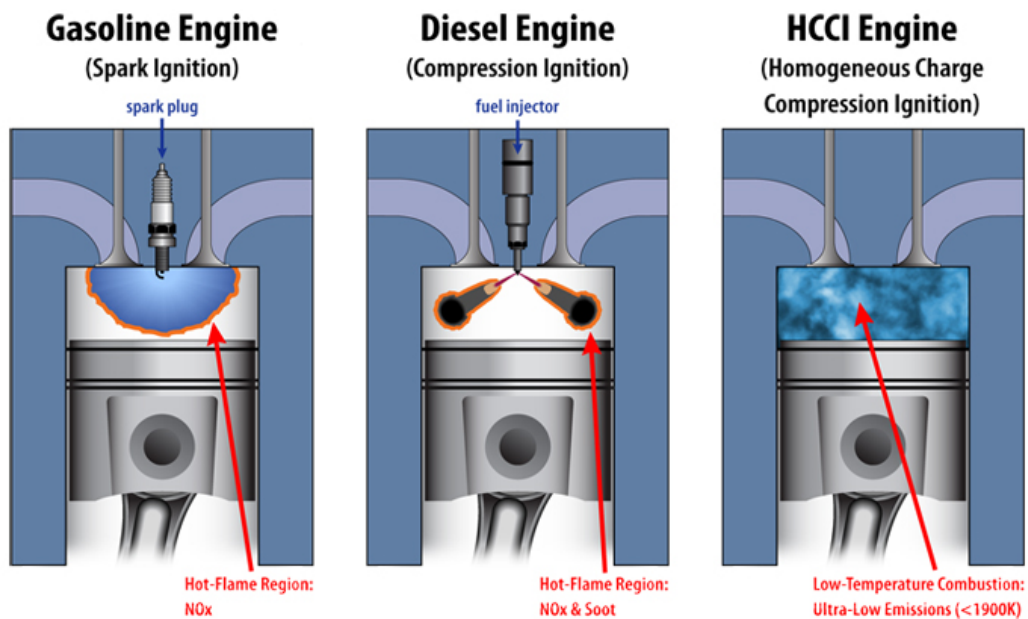


Figure 1.3: A diagram depicting the mechanisms of combustion in transportation internal combustion (IC) engines. (Left) A spark ignition (SI) engine, where a flame kernel is generated via a spark and the flame propagates outward. (Center) A compression ignition (CI) engine, where a heterogeneous reaction occurs at the phase interface. (Right) A homogeneous charge compression ignition (HCCI) engine, where reaction progress is completely controlled by autoignition chemistry. Figure reproduced from [66].

For a conventional SI engine, a premixed fuel + air charge is inducted into the cylinder and compressed to a thermodynamic state below the fuel autoignition conditions. After compression a flame kernel is generated via a spark, where combustion timing can easily be controlled. A reaction front propagates from the spark plug to the cylinder walls, within which the unburned fuel + air is converted to combustion products, until the flame finally extinguishes at the cylinder wall. Typically in an SI strategy the charge is nearly stoichiometric in order to ensure the stability of the ignition and propagation of the flame. Combustion efficiencies using this strategy can be as high as 95-98%, with inefficiencies attributed to piston ring blowby as well as flame quenching at the wall inhibiting the CO to CO₂ conversion [44]. However, in addition to the production of the toxic gas CO, locally high temperatures at the flame front and in the burned mixture promotes the formation of NO_x [67]. Emission of these pollutants into the environment can be reduced by using three-way catalysts in the exhaust after-treatment system [68]. Engine efficiencies for SI strategies while operating at full load (i.e. wide open throttle (WOT)), can be as high as 34% [69]. Engine inefficiencies are mainly attributed to power metering; in SI engines power is metered by choking air + fuel intake into the cylinder using a throttling valve. This process has the effect of a reduced intake and compressed pressure. The thermal efficiency decrease due to the brake mean effective pressure (BMEP) drop is usually referred to as throttling loss [70]. Engine efficiencies can drop to 10-20% as SI engines operate at 10-20% full load. This typically corresponds to roughly 50-60 km/h road speed [69]. Currently strategies to reduce throttling losses are being developed such as variable valve timing (VVT) and lift [71], variable compression ratio [72], downsized high-boost engines [44] and gasoline direct injection (GDI) for stratified charge lean burn [73]. By utilizing a combination of these strategies, SI engines may be able to be manufactured with CI type efficiencies.

Conventional CI engines operate by compressing a mixture of fresh air and

exhaust gasses that have been recirculated into the cylinder (EGR) before fuel is introduced into the cylinder. After the gasses are compressed to high temperature, liquid fuel is directly sprayed into the cylinder using a fuel injector. As the fuel vaporizes a diffusion flame develops near the surface of the spray, and the reaction progress is controlled primarily by the rate of vaporization and turbulent oxidizer mixing. Globally lean charges are almost always utilized in CI engines as high fuel concentrations near the reacting spray surface ensures flame stability. Typically, extremely high combustion efficiencies of up to 99% can be achieved [44]. Unfortunately, high temperatures in the flame front can lead to NO_x formation as in SI engines. In CI engines high fuel concentrations also lead to the production of PM (soot) [74]. While pollutant emissions have historically been a concern for diesel engines, in the last 15 years advances in exhaust aftertreatment systems that make use of catalysts and PM traps have lowered PM emissions by 98% and NO_x emissions by 97% [75]. Engine efficiencies for CI strategies are typically higher than SI at approximately 30%, since they do not suffer from the throttling losses characteristic of SI engines [76].

Figure 1.4 illustrates the fuel loading and combustion temperatures where sooting tendencies and NO_x production are prevalent. As discussed, SI schemes tend to have high NO_x production, while CI technologies can exhibit high NO_x production along with sooting tendency. In recent years a push to minimize toxic and harmful emissions has led to a vast amount of scientific research into lean charge LTC strategies which fall in the green region of the plot. The goal is to improve engine efficiency while simultaneously lowering pollutant emissions. Many other variant strategies of the three discussed here exist to produce high efficiency, clean engines such as premixed charge compression ignition (PCCI) [78] and dilute clean diesel combustion (DCDC) [79]. As one example, HCCI is discussed in detail here.

In HCCI [80] a premixed lean fuel + air is inducted into the cylinder, the charge is compressed to its autoignition conditions. In the most

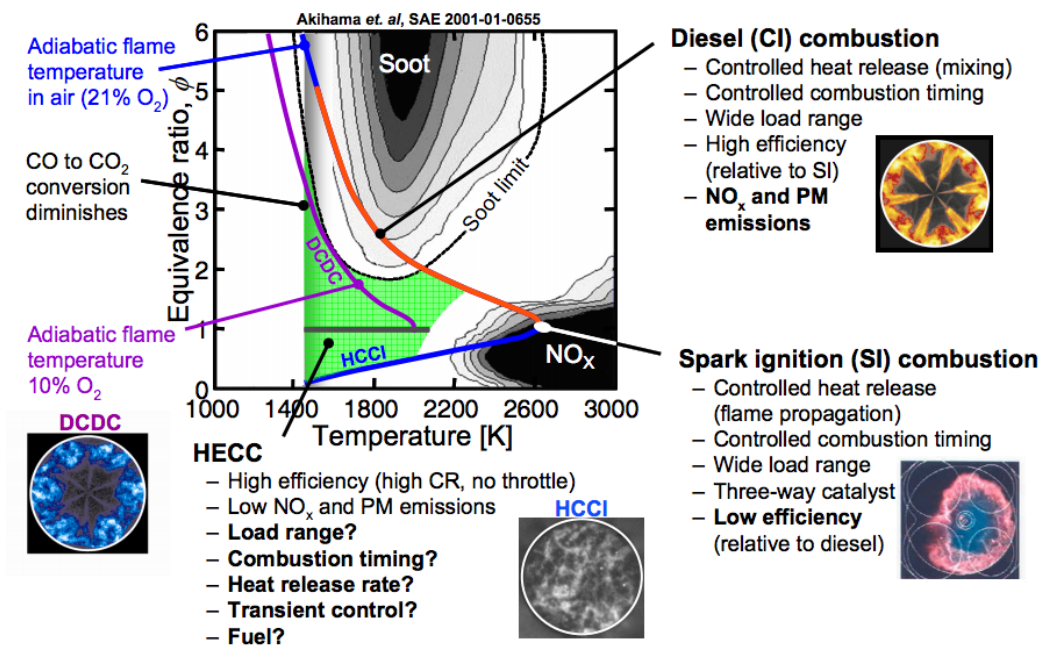


Figure 1.4: Sooting and NO_x production regimes of IC engines. Figure reproduced from [77].

thermodynamically efficient process the fuel quickly autoignites uniformly throughout the cylinder. Unlike SI and CI strategies, there is generally no flame present in HCCI combustion, and typically much lower emissions of NO_x and soot can be achieved [81]. However, since in HCCI the start of combustion (SOC) is controlled by charge temperature and composition, transient loadings are much more challenging as chemical kinetics models are needed to accurately predict combustion phasing and ROHR. Even with these challenges, there are opportunities to develop hybrid engines that can switch between HCCI to SI or CI schemes during cold start, idle or high loads [82]. Comparable engine efficiencies to CI engines can be achieved in HCCI as throttling losses are eliminated, and relatively high compression ratios and short combustion times are realizable [80].

High engine efficiencies combined with low in-cylinder pollutant formation make HCCI a potential choice for next-generation engine technologies. This can only be achieved, however, through a better fundamental knowledge and predictive models for fuel chemistry so that HCCI or similar strategies can be

successfully utilized for a wide range of fuels and engine operating conditions.

Combustion Chemistry Models

Prototyping IC engines that make use of more sustainable fuels or new lean burn, LTC combustion processes can be an expensive and time consuming effort [73]. Accurate *a priori* engineering models that can predict engine fuel consumption as well as pollutant formation are invaluable during the R&D phase of engine design, as these models can drastically reduce the need to build multiple physical prototypes [18]. Engine modeling is an interdisciplinary field combining aspects of CFD, computer science, multi-phase physics, turbulence and chemical kinetics [83]. While this thesis is mainly concerned with the development of chemical kinetic models for transportation fuels, chemical kinetics processes are strongly coupled to in-cylinder fluid dynamics. Computer software has been developed that has the capability to resolve detailed in-cylinder fluid dynamics (e.g. KIVA, Fluent, Converge, OpenFoam) using Reynolds-averaged Navier-Stokes (RANS), Large Eddy Simulation (LES) approaches [84]. However, realistic simulations can be computationally expensive, and when detailed chemistry is added, these simulations can quickly become computationally intractable [85].

At a reduced-order level, simple combustion chemistry models can be ignition delay correlations, where these can be used to characterize ignition timing over a range of conditions for system simulations and engine control algorithms. Ignition correlations are fit to experimental shock tube and RCM data or detailed kinetic simulations using adjustable parameters for temperature, pressure and oxygen concentration [86]. For the accurate prediction of ROHR and in-cylinder pollutant formation additional correlations based on chemical kinetics models for fuel decomposition and oxidation are required. Reduced,

skeletal mechanisms can also be used to calculate ROHR [87], though much more detailed mechanisms are required in order to track pollutant formation processes that depend on numerous intermediate chemical species.

Chemical kinetic models for fuel decomposition and oxidation can be extremely complex, consisting of hundreds of species and hundreds to thousands of elementary reactions [17]. Typically, mechanisms are built in a hierarchical fashion, where reaction pathways and associated rate constants for smaller species are validated based on various experimental targets [88] and expanded to construct mechanisms for larger species. Through advances in quantum chemistry, determination of fundamental reaction mechanisms has the potential to be partially automated [89].

Reaction rates are typically prescribed for the generic reaction, Eq. (1.1), by applying the law of mass action, Eq. (1.2) [67].



$$\text{RR} = \frac{d[\text{prod.}]}{dt} = \frac{d[\text{reac.}]}{dt} = k \prod_{i=1}^N [M_i]^{\nu'_i} \quad (1.2)$$

Here M indicates the species, ν is the stoichiometric coefficient, the index i runs over all N species, RR stands for reaction rate, k represents the reaction rate constant and the bracket notation indicates the molar concentration of the species inside. This equation stems from molecular collision theory, and fundamental reactions takes on the usual meaning (e.g. isomerization, atomic addition, β -scission, uni-molecular decomposition, radical recombination, etc.). Reaction rate constants are usually borrowed from analogous reactions, and tuned to experimental data or high-level electronic structure + transition state calculations. These are generally expressed in modified Arrhenius format, given

by Eq. (1.3).

$$k = AT^b \exp\left(-\frac{E_a}{RT}\right) \quad (1.3)$$

Rate constants can vary greatly over a range of temperatures, pressures and dilution levels, and it is important that rate coefficients are validated over a wide range of conditions to maintain accuracy [67].

Reaction thermochemistry can be prescribed by several methods. High-level computational chemistry simulations (e.g. [90]) or experimental determinations of specific heat are typically the most accurate. Group theory (i.e. Benson’s method [91]) can be used to estimate specific heats for most species, and this process has been automated by the THERM software. Polynomial fits for specific heat can also be obtained from the JANAF or NASA tables.

After validated formulations for chemical kinetics and thermochemistry are obtained, successful predictions for ignition timing, ROHR, and depending on the detail of the mechanism in-cylinder pollutant formations are possible. Several experimental devices are well-suited to validate these mechanisms, a few of these will be discussed in the following section.

Chemical Kinetic Mechanism Validation

While combustion chemistry has been investigated in motored engines, which provide the most realistic environment for operating engines isolation of fundamental chemical phenomena from the complex transport processes is challenging [95]. Because of this, chemical kinetics mechanisms are generally validated against a wide array of idealized experiments that have very well-defined or eliminated fluid dynamics and heat transfer processes. A discussion of a few popular techniques are available in ref. [96]. A limited sub-set

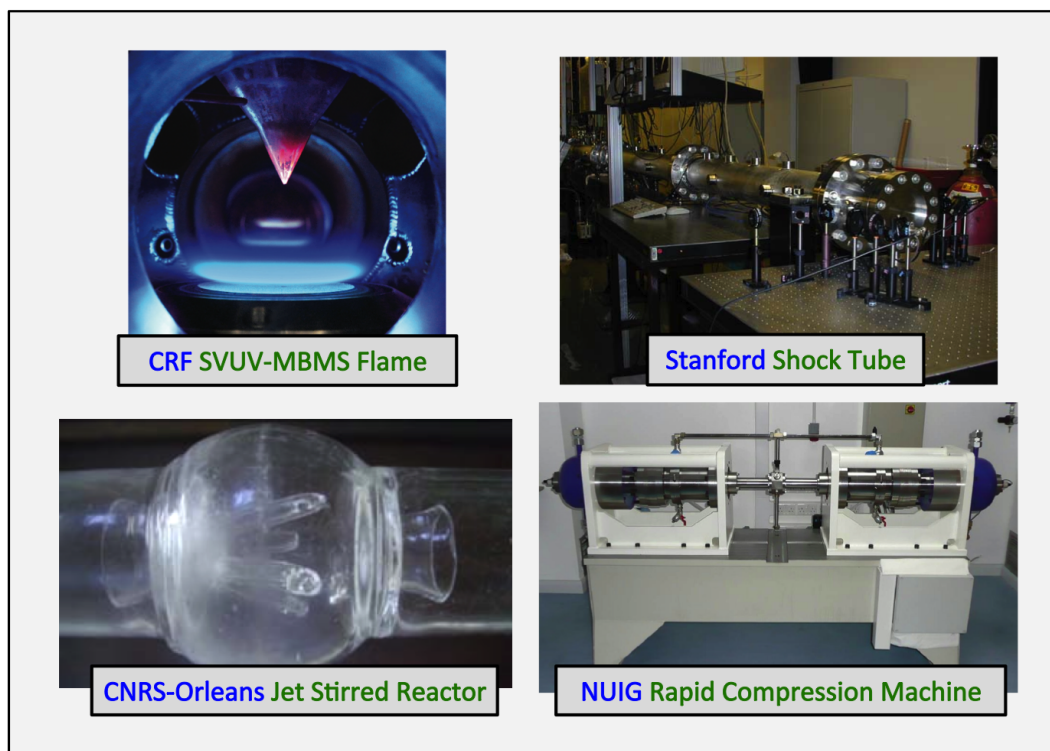


Figure 1.5: Experimental devices used for developing combustion chemistry targets. (Top-left) The low-pressure, flat flame burner at Sandia National Laboratory. (Top-right) The chemical kinetic shock tube at Stanford University. (Bottom-left) A jet stirred reactor at Le Centre National de la Recherche Scientifique-Orleans. (Bottom-right) The rapid compression machine at the National University of Ireland-Galway. Original photos from [83,92–94], respectively.

of these experiments are able to achieve engine-like temperatures, pressures, oxidizer concentrations and equivalence ratios. Combustion chemistry models for use in IC engine simulations are most frequently compared to data collected from flow reactors, shock tubes, RCMs and more recently laminar flames (e.g. [14–17]). Characteristic experimental setups for these devices are shown in Figure 1.5. Each apparatus can access a different regime of temperature, pressure and chemical reaction times, and data sets from some or all of these experiments are required to fully validate a combustion mechanism.

Diverse data sets can be obtained from experimental chemistry apparatuses where, for instance global metrics for reaction progress such as autoignition delay time are sufficient validation targets (e.g. [52]). Autoignition time has been defined in many ways, including the maximum rate of pressure rise and the peak

concentration of OH^* radicals [97], and can be measured experimentally by use of high-speed pressure transducers or optical emission rigs, respectively. Temporal profiles of intermediate species concentrations can be obtained by laser-based diagnostics or physical gas sampling techniques for a more vigorous validation of mechanisms. Provided that the experiment is optically accessible molecular absorption, Rayleigh scattering, laser induced fluorescence (LIF) and anti-Stokes Raman spectroscopy (CARS) have been used to measure intermediate species concentrations [98]. For laser-based techniques to provide adequate data, the photo-chemistry of the species to be measured must be available. Typically data sets for just a few intermediates (e.g. NO^* , OH^* , CH^* , etc.) can be found in the literature [98]. Characterization of additional important species is one area of active research. Gas sampling techniques provide access to concentrations of stable intermediate species and some radicals, where small gas samples are taken during the chemically reactive period for off-line analysis. Off-line analysis can be achieved through the use of gas chromatograph (GC) and mass spectrometry (MS) techniques, however sample degradation due to further reaction or condensation while transportation to the GC/MS can be challenging to suppress. The remainder of this section reviews the typical experimental conditions and commonly obtained data sets for each of the apparatuses designed to collect combustion chemistry validation targets.

Laminar Flames

Laboratory scale flames can acquire highly detailed species concentration data [53]. Typically, for mechanism development and validation, flat pre-mixed laminar flames are used to isolate the fuel chemistry from oxidizer mixing rates. The experiment is conducted by supplying fuel + oxidizer + diluent to the burner plate, where a chemical reaction is initiated. Species concentration data

is collected at varying distances from the burner (corresponding to varying reaction residence times), using laser-based or gas sampling diagnostics.

Low-pressure flames are used (40 Torr) to allow spatial resolution of the reacting zone, where the flame thickness is inversely proportional to pressure [99].

Unfortunately, these pressures are much lower than typical IC engine pressures.

While the experimental pressures for laminar flames are lower than encountered in IC engines, mechanistic insight into fuel combustion chemistry can be obtained as detailed data can be collected from these experiments [100]. Modern flame experiments make use of the high fidelity molecular-beam gas sampling method, where chemistry is effectively quenched during sampling. After molecular-beam sampling at a desired burner distance, the gas is analyzed by a high selectivity time of flight (TOF) MS [99]. Utilizing this method, concentration data can be obtained for short lived radicals as well as resolved selectivity between intermediate isomers. For successful TOF-MS analysis the gas sample is photo-ionized by synchrotron radiation [53,99], though access to necessary facilities such as the Advanced Light Source is currently limited along with combustion relevant data sets.

Flow Reactors

Flow reactors (FRs) and jet stirred reactors (JSRs) are used to investigate low to high temperature (500 – 1500K) gas-phase chemical reactions at pressures up to 15 bar [101,102]. Flow reactor experiments are conducted by first mixing fuel, oxidizer and diluent streams upstream of the reaction vessel, although many flow reactors mix the fuel and oxidizer within the reactor (e.g. the Princeton and Drexel FRs). Diffusive mixing is achieved in FRs, while JSRs make use of turbulent jets to mix the charge. The well-defined gas travels downstream into an electrically heated reaction chamber, with a precisely controlled wall

temperature. Typical mixture residence times in the heated reaction chamber are between 0.1 to 10 seconds, making the device ill-suited for studying rapid chemical phenomena such as an ignition process. Very dilute fuel mixtures are utilized to minimize gas thermal and compositional stratification within the reaction chamber, limiting the range in which validation targets may be obtained. The well-defined gas is sampled as chemical reactions progress, and analyzed by GC/MS systems to obtain species concentration data of stable intermediates.

Shock Tubes

Shock tubes are laboratory devices which can be used to investigate high temperature (1000K – 3000K) and rapidly occurring chemical reactions (0.03 – 5.0 ms) at pressures from sub-atmospheric to 50 bar [103–105]. The device consists of a long metal cylinder with two gas volumes, the driver and driven sections, that are partitioned by a thin diaphragm or rapidly actuating valve. The apparatus is operated by storing high pressure driver gas behind the diaphragm or valve, and loading a fuel charge in the partition downstream. To initiate the experiment the diaphragm is burst or the valve is actuated, and the driver gas rapidly expands into the driven section. As the driver gas expands a traveling shock wave develops. The fuel charge is initially shock heated as the wave travels through the driven section and further heated when a reflected shock from the reaction chamber endwall arrives. The charge is rapidly heated ($\sim 10\ \mu\text{s}$) and the elevated gas temperature and pressure can be maintained for up to $\sim 5\ \text{ms}$.

Most shock tubes are fitted with high speed pressure transducers to obtain shock velocity and time history of the reacting gas. Autoignition data can be inferred from the exothermic ignition. Some shock tubes also have optical access

for the collection of laser-based intermediate speciation data [106]. In addition, sampling techniques can also be used to collect off-line species concentration data by use of GC/MS systems [107].

Recently an aerosol shock tube was developed to extend experiments to involatile fuels [38]. In this setup a fuel aerosol in a oxidizer + diluent bath gas is loaded into the machine instead of a conventional gas-phase mixture. The fuel aerosol is fragmented and heated at the arrival of the initial shock, and the liquid is fully vaporized and diffusively mixed before the arrival of the reflected shock. A gas-phase test then proceeds after the arrival of the reflected shock.

Rapid Compression Machines

Rapid compression machines are laboratory devices used to investigate intermediate temperature (650 - 1100 K), high pressure (up to 90 bar) chemistry, at time scales of up to 150 ms. Rapid compression machines are well-suited to investigate fuel decomposition and oxidation chemistry at engine relevant conditions. Within this device, a traveling piston is used to volumetrically compress a gas mixture to a high temperature and pressure where decomposition and oxidation chemistry can be investigated. Most machines make use of a single piston [39, 108–110], while some use two opposed pistons such as the NUIG RCM shown in Figure 1.5. Most machines utilize a high pressure pneumatic system to drive the piston and a hydraulic system to actuate piston motion and control the piston trajectory. By this method, rapid compression times (~ 20 - 80 ms) are realizable. The hydraulic system can be used to “lock” the piston when maximum compression is reached, achieving a constant volume during the chemically active period (some machines use a more novel approach for piston actuation and attenuation [111, 112]).

Modern RCMs utilize creviced piston geometries to suppress in-cylinder fluid

dynamics during the experiment. While the use of these pistons has improved charge homogeneity, characterizing heat loss from enthalpic flows to the crevice and conductive transport to the reaction chamber walls remains challenging. Heat loss models are used to account for these losses while comparing simulations of chemical kinetics. These models are typically 0D variable volume homogeneous reactor models (HRMs), where the volume of the reaction chamber can be expanded to emulate machine heat loss (or compressed to emulate chemical heat release effects [113]). The rate of volume change to the HRM can be prescribed using experimentally derived corrections [109] or by use of a physics-based model for heat loss [36].

Rapid compression machines are fitted with pressure transducers, and a single pressure trace is the common data set obtained from the experiment. From this data fuel autoignition delay times can be inferred. Some machines are fitted with optical access to make laser-based diagnostics available [114]. A few facilities also make use of gas sampling modules for off-line analysis by GC/MS [114].

As with shock tubes, recent efforts to extend RCM experiments to involatile fuels by the use of an aerosol fuel charge have been made [39, 115]. In this wet compression approach, a fuel aerosol is loaded into the machine and volumetrically compression heated. In a well-designed experiment complete fuel vaporization and mixing could be achieved by maximum compression. This process is more challenging than in shock tube experiments though, as the physics of the vaporization process is different. In shock tube experiments the traveling shock wave fragments fuel droplets and accelerates vaporization and mixing times [38]. Droplet fragmentation does not occur in RCM experiments, and much smaller droplet sizes are therefore required to achieve sufficiently short vaporization time [116, 117]. In-cylinder compositional stratification may be problematic for these experiments as varying rates of evaporation and condensation occur in the thermal boundary layer near the cool reaction chamber surfaces. The gas-phase stratification may also be intensified as these

compositional gradients can drive gas-phase fuel diffusion to the unvaporized regions near the reaction chamber walls. Increased thermal stratification within the reaction chamber may result as varying rates of vaporization and fuel condensation near the reaction chamber walls exist. To this point there has been no effort to investigate the effects of device-scale multi-phase physics during RCM experiments.

Heated, pre-vaporized experiments using heavy fuels can also suffer from phase-change phenomena during the test period as the high pressure can cause some of the heaviest components to condense near or on the internal RCM surfaces. This can lead to difficulties interpolating the experimental result, as the thermodynamic state is altered. These phenomena are investigated in this work where a physics-based, reduced order model is developed. The modeling framework has already been demonstrated for gas phase experiments [36, 113], so that effects of crevice flows, heat loss and thermal stratification within the reaction chamber can be adequately simulated. Here, compositional stratification due to phase change is studied. The framework is computationally efficient so that it can be coupled with an HRM where the chemical kinetics of the fuel + oxidizer + diluent mixture can be simulated. Where insight can be derived regarding the design of aRCMs.

Thesis Outline

The investigation of multi-phase effects during RCM experiments is undertaken here using a computational approach. A multi-phase multi-zone model (MP-MZM) is developed and applied to typical conditions utilized in RCM experiments with a focus on heavy fuel components. The outline of this manuscript is as follows. First, review of current and future RCMs is presented in the next chapter. Chapter 3 then provides the details of the formulation used

in the new MP-MZM model. Chapter 4 covers the validation of the model and various sub-models utilized by comparison against detailed simulation results, after which results investigating phase-change effects that might occur during aerosol-fueled experiments are presented. While the new model has the capability of prescribing departures from ideal, adiabatic conditions for simulations of the chemical kinetics that occur during the experiment, this is not demonstrated in the current work. The manuscript concludes with a summary of the work, and findings from the study. A discussion of future work is also provided.

Chapter 2

Rapid Compression Machines

Introduction

The design of historical, modern and future RCMs are the focus of this chapter. More specifically this work is concerned with the ~ 24 machines, worldwide, tailored for setting chemical kinetic validation targets. A complete “lock and key” RCM can be purchased from Marine Technology [118], however most of the RCMs in operation have been customly developed and built by universities as well as government and corporate research labs. Figure 2.1 shows the affiliations of machines currently in operation. The material presented in this manuscript is meant to be sufficiently generalized to be applicable accross all of the experimental platforms in existence. Thus, this chapter acts as an overview to discuss the caveats between facilities in order to highlight the generality of the new MP-MZM.

Within the last two decades RCMs have become more prevalent for the acquisition of transportation-relevant, fuel chemical kinetic validation targets. This is depicted by Figure 2.2, which illustrates the amount of literature recently published on RCM-related data, modeling and experimental methods. Since 1995 several new machines have been constructed along with new experimental methods which extend the capabilities of current devices (e.g. optical access, gas sampling modules, improved piston crevice designs and aerosol fuel loading). Within the last 10 years there has been a large increase in the amount of experimental data collected from RCMs in addition to the amount of chemical kinetics mechanisms that are validated based on RCM data for validation. A significant amount of research has also been conducted to fundamentally

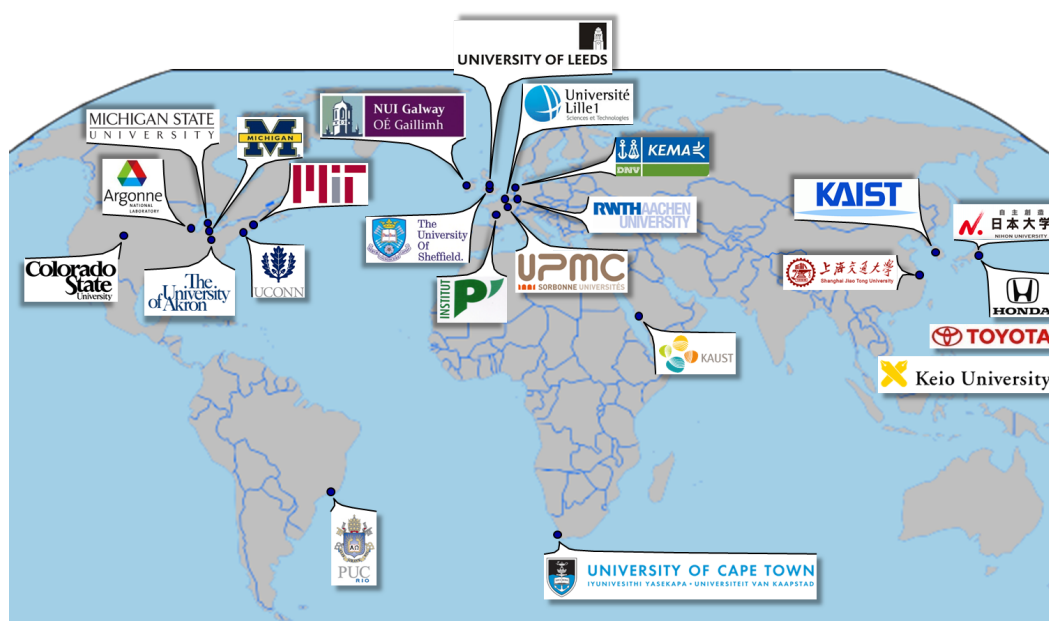


Figure 2.1: The affiliations of the world's RCMs tailored for chemical kinetics studies. Image reproduced from [119].

understand the physics of RCM experiments, so that a more adequate comparison of collected data and combustion chemistry models can be made.

This chapter begins with a historical review of RCMs. Where some of the early challenges associated with RCM experiments, while the importance of some key RCM design features common in modern machine designs are identified. Although some of these challenges have been addressed over the years, opportunities to improve data fidelity and expand machine capabilities are still present. The following section reviews the design of a few modern RCMs, where the unique solutions to experimental challenges of each facility are presented. Approaches utilized to account for non-ideal conditions in RCM experiments are then discussed. The chapter ends with a discussion of some design features that future RCMs may include.

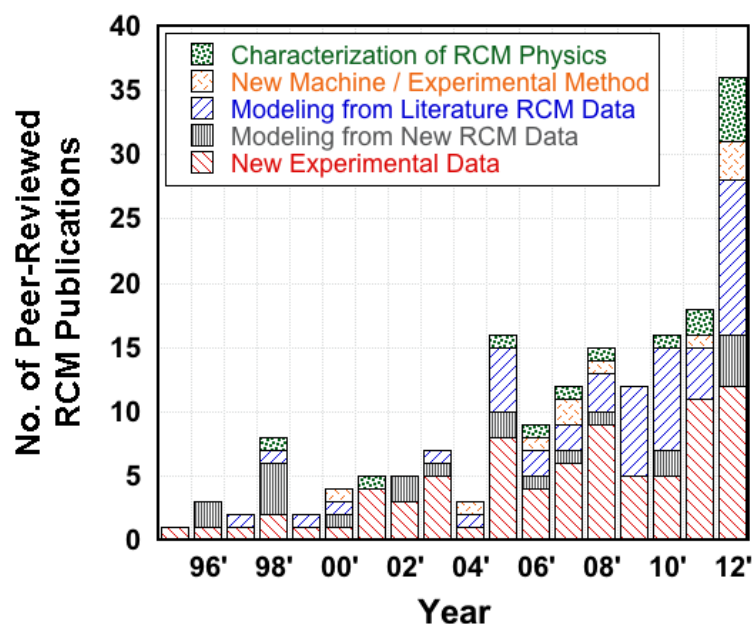


Figure 2.2: RCM related publications since 1995 surveyed from Combustion and Flame, SAE, Energy and Fuels, Fuel, Proceedings of the Combustion Institute, The International Journal of Chemical Kinetics and The Journal of Chemical Kinetics A, which include [8–17, 19–37, 39, 51, 52, 86, 97, 112–117, 120–256].

Historical Machine Designs

The idea of investigating fuel chemistry in an RCM has existed for about 100 years. Early devices which were crude by today's standards, were used to investigate temperature and pressure dependence on fuel autoignition.

Experimental setups utilized of piston-cylinder geometries that were driven by falling weights and pulleys.

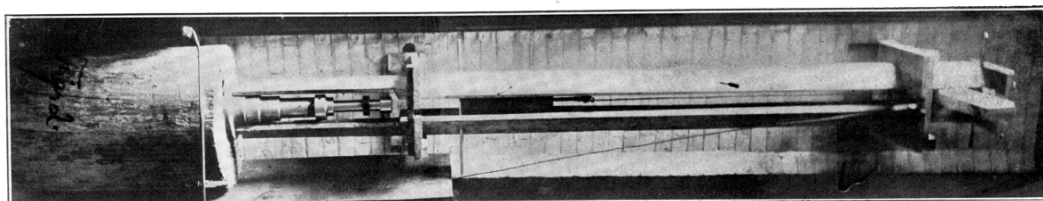


Figure 2.3: A photograph of the fourth RCM built by Falk. Image reproduced from [257].

The first RCM was constructed by Falk at Columbia University in 1906 [258], a photo of which is shown in Figure 2.3. This device was driven by a falling weight so that it achieved a reported “instantaneous compression.” No additional mechanisms were used to keep the piston seated at maximum compression. The reaction chamber therefore did not maintain constant volume at the end of the compression stroke. A flat piston was used with hemp seals and Lanoline lubricant. Falk was able to characterize the autoignition temperature of the H_2/O_2 [258] system as well as other gas mixtures [257] with his RCM.

In 1914 Dixon et al. built the first optically accessible RCM [259]. This RCM consisted of a steel piston and a glass cylinder. The piston was driven by a swinging pendulum, allowing the machine to have an adjustable stroke. With this machine Dixon was able to capture flame images, and even estimate flame speeds. Dixon suggested that the ignition process was not as instantaneous as Falk had first proposed. Dixon subsequently built a machine similar to Falk’s, but with an improved design, and with this updated Falk’s H_2/O_2 results [260].

A few years later an RCM was built by Tizard and Pye that was capable of measuring the ignition delay time for IC engine relevant fuels [261]. The machine used a novel setup for driving the piston and locking it at maximum compression. The piston was driven by a fly wheel with a crank arm and connecting rod, similar to that of a motored engine. The connecting rod and crank arm could be engaged by use of a clutch. A two-piece connecting rod was used, and the connection would become rigid at top center, locking the piston in place. In-cylinder pressure was recorded using a pressure indicator, and from this time history plots of cylinder pressure could be obtained. Tizard noticed from his pressure traces that heat loss from the test gas had a significant impact on the thermodynamic state before ignition, and that RCM experiments are generally not adiabatic. He attributed this to fluid motion and heat loss to the cylinder walls, and even developed a crude model to account for the in-cylinder heat loss.

Even from these early experiments non-ideal conditions that effect RCM

experiments could be observed where these can be challenging in order to overcome to collect autoignition data. Since these early experiments, advances in electronic control systems have helped to control piston trajectories, achieve faster compression times and ensure a constant reaction chamber volume after maximum compression. Advances in laser-based diagnostics (e.g. PLIF and Rayleigh scattering) and CFD have been used to characterize and understand the in-cylinder dynamics, including stratification and fluid motion. From these results updated piston geometries can be used to suppress convective motion inside the reaction chamber, and drastically reduce the amount of thermal stratification previously observed. A review of the novel approaches modern machines utilize to overcome these experimental challenges is presented below.

Modern Rapid Compression Machines

A review of modern RCM design is presented here, where descriptions are provided for the machines located at the University of Connecticut (UConn) [10], the National University of Ireland-Galway (NUIG) [262], the University of Lille-Science and Technology (Lille) [111], the University of Michigan (UM) [112], Argonne National Laboratory (ANL) [184] and the Massachusetts Institute of Technology (MIT) including the one built by Park and Keck [110] and the other built by Tanaka et al. [148]. This review is limited to these RCMs as they have used as the basis for many most of the others that exist worldwide. For instance, the opposed-piston RCM originally built by Shell in the 1960's [262] and modernized [254] by NUIG served as a model for the machine at the University of Leeds [108], and more recently at Colorado State University and King Abdullah University of Science and Technology [118]. The RCM originally built at Case Western Reserve University (CWR) [109] motivated the

designs for the machines at UConn, the University of Akron [263] and Michigan State University (MSU) [39]. The machine developed at ANL was originally designed as a opposed-piston clone of the Park and Keck MIT RCM, however major modifications to the machine have recently implemented [264].

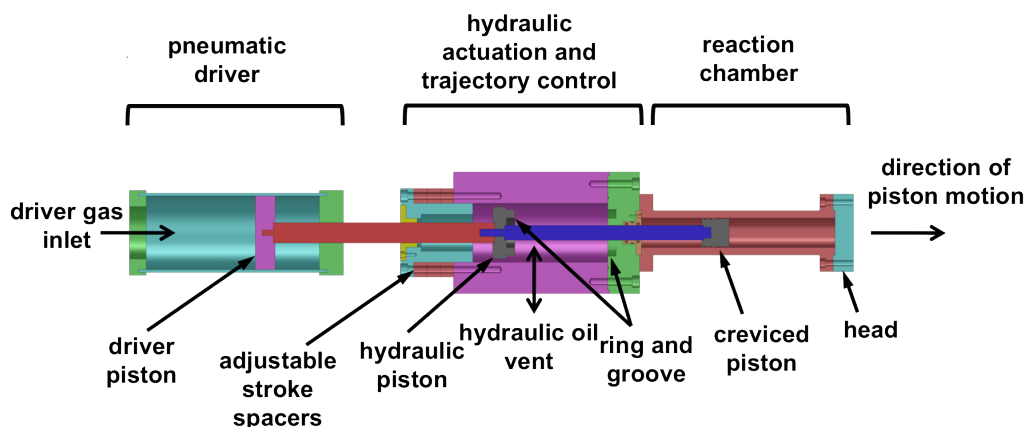


Figure 2.4: Schematic of a generic pneumatically RCM, which closely resembles the machine at the University of Connecticut.

Table 2 lists the primary design features and operational regimes typically utilized for these select machines. In this Table P_{max} corresponds to the highest reported compressed gas pressures, CR are the machine compression ratios, τ_{comp} are compression times, the crevice ratio is defined as the ratio of the piston crevice volume to the total RCM volume, and the surface area to volume ratio of the reaction chamber is evaluated at compressed conditions.

Figure 2.4 presents a schematic illustrating the main components of a generic RCM that utilizes a hydraulic system for piston activation and piston control. Most machines employ a pneumatic driver section which is used to accelerate the piston and compress the reacting gas mixture. A secondary mechanism, such as a hydraulic reservoir and piston, are used to actuate the experiment and control the piston trajectory. Also depicted in this Figure is the reaction chamber where chemical reactions can be investigated.

Table 2.1: Design features of a few rapid compression machines.

Facility	P_{\max} [bar]	CR	τ_{comp} [ms]	t_{50} [ms]	Crev. Ratio	SAV Ratio [cm ⁻¹]	Traj. Control	Gas Samp.	Opt. Access
NUIG	50	12 - 18	15.3	2.3	0.145	1.8 - 2.0	hydraulic	✓	✗
UConn	70	7 - 15	30 - 45	4.8	0.166	1.7 - 2.2	hydraulic	✓	✓
Lille	40	9.8	20 - 70	6.8	0.034	1.9	cam	✓	✓
ANL	70	9 - 18	20	5.8	0.014	1.6 - 1.9	hydraulic	✗	✗
UM	25	16 - 37	80 - 100	3.5	N/A	1.0	deformation	✓	✓
Park and Keck	40	3 - 20	15 - 18	3.4	0.034	1.5 - 2.7	hydraulic	✗	✗
Tanaka et al.	70	19 max	10 - 30	1.0	0.034	1.5 - 2.7	hydraulic	✗	✓

Piston Trajectory Control and Seating

Many RCMs utilize a hydraulic system for experiment actuation, and piston trajectory control, though the machines UM and Lille, which will be discussed at the end of this subsection do not. For a graphical description of this methodology and configuration the reader is referred to Figure 2.4. In this design a high-pressure gas (~ 20 bar) is stored behind a large diameter (i.e. 15 - 20 cm) driver piston, connected to hydraulic and creviced pistons via a connecting rod. A large diameter for the pneumatic piston is utilized to maximize the driving force exerted on the creviced, reaction chamber piston. The hydraulic piston, which is located midway along the shaft, resides in a reservoir filled with high-pressure hydraulic oil. When fully retracted, the pressurized hydraulic system keeps the piston seated at maximum volume in the reaction chamber, sometimes referred to as Bottom Dead Center (BDC), during pressurization of the pneumatic driver and before an experiment is started. To actuate piston motion, high-pressure hydraulic oil is vented from the reservoir, while the initial piston trajectory is partially controlled by the geometry of the venting ports (due to the rate at which fluid leaves the reservoir). Another factor controlling the piston trajectory is the geometry of the hydraulic piston and chamber, where fluid dynamic drag and thus the rate at which the piston travels through reservoir can be changed by varying the geometry. For instance, some RCMs utilize a hydraulic piston that is chamfered on the back-end to reduce the amount of fluid drag (e.g. [39]). Others use a larger gap between the piston and the bore of the hydraulic chamber. In particular, the NUIG hydraulic chamber is designed with a converging throat to control piston speed.

An efficient mechanism for piston arrest is also key in RCM designs. The majority of charge temperature and pressure rise occurs within the last 10% of compression, and a very rapid rise in temperature is desired in later stages of the stroke since the mixture will be very reactive under these conditions. Rapid

compression during the end of the stroke is achieved by a sharp deceleration of the piston; if this is not achieved the gas experiences a high residence time at elevated, but sub-compressed temperatures. If this occurs, fuel decomposition and oxidation chemistry can begin at pre-compressed conditions, making experimental conditions challenging to characterize succinctly.

Rapid piston deceleration is achieved in many designs by a ring on the hydraulic piston which fits into a groove in the hydraulic chamber wall where the clearance is very small (e.g. 0.4 mm). Near the end of compression the hydraulic ring enters this groove, pressurizing the hydraulic oil in the groove. The clearance between the ring and groove is small so that the pressure-driven flow exiting the groove is small, thereby slowing the piston until it eventually comes to rest as the hydraulic piston fully seats. If the piston is not sufficiently decelerated as the ring fully seats into the groove, piston “bounce” or recoil can occur resulting in a reaction chamber volume expansion at maximum compression. Additionally, piston creep can also be problematic if the configuration is not optimized. Currently, little work has been undertaken to fully understand the hydraulic mechanisms for piston speed control and deceleration and thereby optimize the hydraulic design. Typically, an iterative approach is used to adjust the clearance between the hydraulic piston ring and groove after the RCM has been built.

The UM and Lille RCMs do not use hydraulic systems for piston control. The Lille RCM utilizes a pneumatically driven sliding cam mechanism to actuate, control and arrest the reaction chamber piston. In this design a mechanical cam and connecting rod guide the piston stroke, and mechanically lock the piston position at maximum compression. The UM machine uses a pneumatically driven sabot which is much more compact, and relies on an interference fit between the sabot and reaction chamber walls to rapidly arrest the sabot and seal the reaction chamber. Very rapid deceleration rates are achieved, though substantial mechanical vibration can result. With this approach the sabot is plastically deformed during its arrestment, and a new

sabot must be frequently used due to degradation. The use of the novel sabot geometry, which different from other reaction chamber piston designs, also ensures charge homogeneity by reducing in-cylinder fluid motion.

Suppression of Fluid Dynamics

A torroidal “roll-up” or “corner” vortex is generally generated during the compression process in piston-cylinder devices [39]. The physics of the vorticular structure and it’s formation have been well-characterized by experimental [109] and computational investigations [251, 252, 254, 255]. This formation is undesired in RCM experiments, since the advective motion transports cooler gasses near the reaction chamber walls into the hotter, i.e. charge core gasses. The entrainment of cool into the reaction chamber core gasses causes thermal stratification within the charge, and the desired well-defined experimental reaction temperature is degraded.

In RCM a crevice piston is typically utilized to suppress the formation of a roll-up vortex during compression. Creviced pistons are typically constructed with a machined tapered gap and opened volume around the circumference of the piston. During compression the tapered gap “swallows” the boundary layer gasses near the reaction chamber walls where vorticular structures are formed. During these experiments the boundary layer gasses are trapped inside the piston crevice region and do not emerge after compression. Detailed CFD simulations have confirmed that the mass flow process from the reaction chamber, through the tapered gap and to the crevice is driven by a small, but finite, pressure differential between the reaction chamber and crevice [36]. The use of these pistons can drastically suppress the roll-up vortex formation, and charge homogeneity is greatly improved. Enthalpic losses, however, from the

reaction chamber to the piston walls can be large and must be taken into account in order to properly define the reaction temperature when evaluating the experiments, as well as chemical kinetics simulations.



Figure 2.5: A few creviced piston designs used in RCMs. In these schematics the pistons have been normalized to a 50.8 mm bore to highlight differences in the crevice geometry.

Significant work has been undertaken in order to optimize crevice geometries for various RCM facilities [251, 252, 254, 255]. This has resulted in the use of different gap and crevice geometries. Representative geometries are shown in Figure 2.5; most RCMs make use of one of these. The sabot utilized by the UM RCM is not discussed here, however this arrangement could be considered (and modeled) within the computational framework described for this thesis. The UConn geometry utilizes a long and narrow crevice volume. The NUIG piston has a much shorter and radially larger crevice geometry. The MIT crevice geometry is much smaller than the other configurations.

Boundary Layer Growth

If a creviced piston is properly utilized in an RCM convective heat losses are suppressed in the reaction chamber, and charge homogeneity is drastically improved. Heat loss from the reaction chamber gasses to the cooler walls is still problematic. Since in modern RCMs fluid dynamics are suppressed, the main mechanism of heat transfer is conduction. Typically, compression times are sufficiently short so that thermal stratification in the reaction chamber gases can be minimal. However, the thermal boundary layer grows as the experiment proceeds, and can have a detrimental affect on the homogeneity of the test charge. The propagation of the boundary layer into the reaction chamber gasses is even more problematic for experiments using fuels that exhibit negative temperature coefficient (NTC) behavior. In this situation the gas in the thermal boundary layer can be more reactive than the core gasses, where the accelerated chemical pressure rise observed in the thermal boundary layer compresses the core gases and can lead to pressure stratified convective motion and even knock in some conditions. The bootstrapping effect characteristic of NTC experiments drives an increased amount of reaction chamber mass to the crevice, and this can be difficult to take into account.

The rate and extent of heat conduction from the reaction chamber gas to the RCM surfaces is controlled by thermophysical properties of the test charge as well as the machine geometry. The thermal diffusivity of the gas ($\alpha = k/\rho c_p$) is the primary parameter. Since the properties of the charge varies from shot to shot, compressed reaction chamber geometries are used here to compare a machines propensity to be affected by thermal stratification due to heat conduction to the machine surfaces. The geometric parameter of interest is the compressed surface area to volume ratio (SAV) of the reaction chamber. Machines with a higher SAV will tend to transfer heat to the walls faster than a machine with low SAV. Values for SAV are provided in Table 2.

Heat Loss Modeling

Although modern RCM experiments can provide an engine relevant environment suitable for chemical kinetic experiments, prescribing a well-defined reaction chamber test condition can still be challenging. Determining the temperature of the reacting gas is critical to the proper interpretation of these experiments, as chemical kinetic rates display an exponential dependence on temperature.

Unfortunately, RCMs are not typically equipped with temperature measurement systems that have response times rapid enough to provide resolved measurements during the transient experiment. Rayleigh scattering techniques have been used for some investigations [109], though these suffer from quantitative inaccuracies. A new method has been demonstrated, which employs quantum cascade lasers to perform absorption measurements, where gas temperatures are inferred from line broadening data [139, 265]. However, these experiments can be complex to implement and characterize. Because of this, in-cylinder temperatures are typically inferred from experimental pressure traces.

The most rigorous comparisons of chemical kinetic models can be achieved through detailed CFD simulations [249]. These simulations are computationally expensive and especially intractable when reacting flows are considered with kinetic mechanisms that realistically represent real fuels. As such, RCM experiments are generally modeled using a single, 0D volume where detailed chemical kinetics are simulated (i.e. a homogeneous reactor model (HRM)). Since fluid motion during the experiment can be suppressed using properly designed piston crevices, an HRM can provide reasonably adequate detail to compare developed ignition mechanisms to experimental data [266]. Chemical reactions in the cooler crevice gasses are typically inhibited due to high convective velocities which cause low temperatures in this region. Conductive and enthalpic losses from the reaction chamber to the walls and the crevice region, respectively, are emulated in the HRM by an isentropic expansion.

However, thermal stratification due to heat diffusion from the hot reaction chamber gasses to the cooler RCM surfaces is not adequately captured by an HRM framework. Fortunately, in most cases the volume of gases in the thermal boundary layer is small compared to the total reaction chamber, and non-NTC chemistry is inhibited in the cooler gas. The effects of thermal boundary layer growth, and pressure reduction due to convection within the crevice still need to be taken into account however.

While HRMs provide a computationally efficient means to model the chemistry of RCM experiments, however adequately accounting for the effects of heat loss is a non-trivial process. A detailed discussion of some methods that have been previously used is presented next.

Experimental Approaches

The “adiabatic core” model has been widely used to model the RCM reaction chamber. In this formulation the core gases are modeled as a homogeneous reacting mixture, and heat loss to the thermal boundary layer and crevice region may be accounted for.

For RCM experiments ignition delay times are customarily reported in Arrhenius type format as a function of compressed gas temperature. The compressed charge temperature can be prescribed by an isentropic compression relation (i.e. Eq. (2.1)) assuming the adiabatic core hypothesis is valid, and also that the time scale of compression is faster than that of the chemical kinetics.

$$\ln \left(\frac{P_c}{P_0} \right) = \int_{T_0}^{T_c} \frac{1}{T} \frac{\gamma}{\gamma - 1} dT \quad (2.1)$$

In Eq. (2.1) γ is the ratio of charge specific heats, P_0 & P_c are the initial and compressed pressure, respectively, and T_0 & T_c are the initial and compressed

temperature. Compressed temperature can be numerically determined from Eq. (2.1), where the initial conditions are experimentally measured along with compressed pressure. The measured compressed pressure takes into account adiabatic core heat losses to the creviced pistons as well as to the reaction chamber surface, and a close approximation to the core gas temperature is obtained.

A similar approach is implemented to prescribe an effective reaction chamber volume history to the HRM. To obtain an HRM volume profile a non-reactive charge with matched thermophysical and transport properties is experimentally compressed at the same conditions as a reactive charge. The non-reactive pressure trace is used to find the effective volume history of the HRM that accounts for piston compression, enthalpic and conductive reaction chamber losses via Eq. (2.2).

$$V_{HRM}(t) = V_{HRM,c} \left(\frac{P_c}{P(t)} \right)^{\frac{1}{\gamma}} \quad (2.2)$$

Discrete HRM volume history data are then tabulated and used as input to the HRM solver. Less precise methods have been used to prescribe the HRM volume history, where the chemically active period is discretized into two or three sections where constant expansion rates are utilized [266].

Some inconsistencies occur in the adiabatic core formulations when compared to experimental or simulated fluid dynamics models, this is mainly attributed to the assumption that the boundary layer and crevice gases instantaneously reach thermal equilibrium with the reaction chamber surfaces. Regardless the above formulation has been extremely useful for determining heat loss for experiments with volatile fuels, while improvements are needed to sufficiently characterize a broad range of experiments. For instance, reaction chamber heat losses for fuels that exhibit multi-stage ignition phenomena (i.e. cool flame behavior) cannot be adequately accounted for by this method. The chemical heat release and

pressure rise of the first-stage ignition accelerates the rate of enthalpic and conductive heat losses, also bootstrapping effects in the thermal boundary layer are neglected. For these fuels the heat loss during the delay between the low-temperature heat release and main ignition event cannot be characterized by a non-reactive pressure trace. This method is also degraded for low-volatility fuels, where fuel condensation may occur in the thermal boundary layer during the chemical delay period. While condensive heating effects will be included in the measured pressure trace, gas-phase compositional stratification in the reaction chamber will occur. The lean gas-phase conditions at the wall will drive species diffusion from the core gasses to the thermal boundary layer where condensation will occur. Improved experimentally based modeling and data sets would need to be obtained to adequately prescribe a varying composition to the HRM.

Physics-based Models

In the past Newtonian cooling formulations (i.e. Eq. (2.3)) have been formulated to prescribe heat transfer rates to the HRM as opposed to volumetric expansion rates. This is easily implemented in most chemical kinetics codes (e.g. Chemkin, Cantera, etc.) by specifying only a heat transfer coefficient.

$$\frac{d}{dt} [U_{HRM}] = h_{conv} A_s (T_{wall} - T_{HRM}) \quad (2.3)$$

Scaling arguments have been used to obtain an effective convection coefficient, and have been shown to provide very poor agreement with high-order simulations or the reaction chamber. Newtonian cooling formulations have shown to consistently predict accelerated rates of temperature decay in the reaction chamber, and have widely been abandoned in favor of the experimental

technique described above.

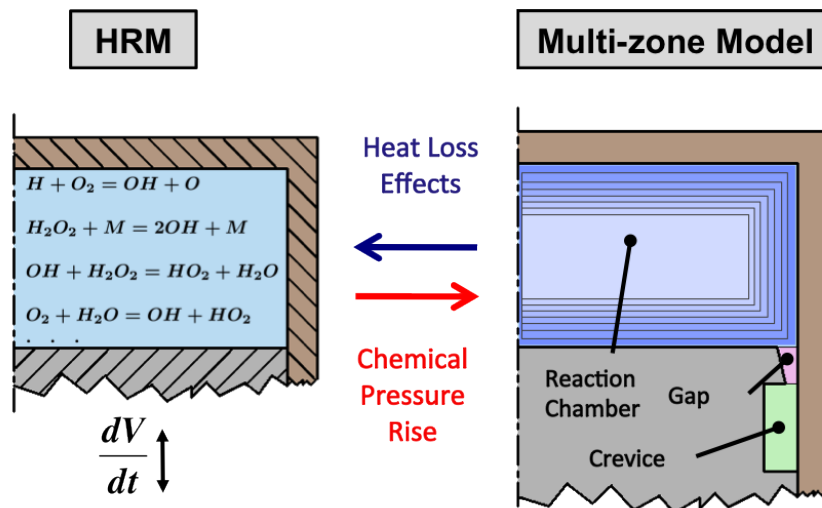


Figure 2.6: Schematic of the multi-zone modeling approach.

More recently a computationally-efficient multi-zone model (MZM) has been adopted to RCMs [36, 113]. In this approach a physics-based subroutine is integrated into an HRM code to prescribe the effective volumetric expansion/compression rates which emulate adiabatic core heat transfer. This reduced-order approach discretizes the RCM into several zones, or control volumes, where conservation of mass, momentum and energy are applied to calculate rates of heat loss from the adiabatic core. The effective HRM expansion is then prescribed via Eq. (2.4), where the terms on the right-hand side (RHS) of the equation are calculated in the MZM reaction chamber.

$$\left(\frac{dV}{dt}\right)_{HRM} = -\frac{V}{\gamma} \left[\frac{1}{P} \frac{dP}{dt} - \frac{1}{N} \frac{dN}{dt} + \frac{1}{c_p T} \frac{1}{N} \sum_{j=1}^{N_{sp}} u_j \frac{dn_j}{dt} \right] \quad (2.4)$$

This equation is derived from the MZM adiabatic core energy equation and ideal gas equation of state (EOS). Although this expression adds complexity over the widely used isentropic expansion equation, thermochemistry effects can be more

accurately captured by this expression.

One advantage to this approach is that the effects of chemical exothermicity on charge heat transfer can be accounted for, by sending rates of chemical heat release to the MZM. This is especially important for fuels that experience cool flame type behavior (e.g. n-alkanes). A graphical description of this modeling approach is shown in Figure 2.6. Also inputs to the MZM are only a function of machine geometry and do not vary from shot to shot, eliminating the need to conduct non-reactive experiments.

The Goldsborough et al. model [36,113] is currently able to account for boundary layer growth in the reaction chamber, mass transfer to the piston crevice, piston seal blowby and chemical heat release effects. The work presented in this manuscript extends the capabilities of this model, and will be discussed further in the following chapter.

Involatile Fuel Experiments

As was discussed in chapter 1, many transportation fuels typically used in IC engines exhibit a low-vapor pressure. Investigating the gas-phase ignition chemistry of these types of fuels in an RCM can be challenging. Conventional RCM experiments with liquid fuels have been conducted by pre-heating the charge and rapid compression machine, however pre-heating can primarily access dilute and low-pressure experimental condition, e.g. $X\%O_2$ and X bar, respectively. A fuel loaded as a dense, finely atomized aerosol has been suggested to extend the limits of these experiments [115]. This novel wet compression technique, however, requires more advanced models for RCM experiments to compare combustion chemistry mechanisms, so that the two-phase processes can be properly taken into account. This section describes in more detail how these

experiments are conducted, and the requirements of a model that can be used to adequately compare data to chemical kinetics mechanisms.

Charge Pre-heating

Pre-heating the fuel charge and RCM reaction chamber have effectively been used to investigate liquid fuels with relatively low boiling points such as gasolines and gasoline surrogates. Pre-heating can be achieved in an external mixing chamber, where a diluent is first loaded into the mixing chamber and liquid fuel is metered in with a syringe. The fuel + diluent mixture is allowed to reach phase equilibrium and is either magnetically or diffusively mixed. Before the test, the oxidizer is added and then the mixture is sent through heated plumbing into the heated RCM reaction chamber, where the experiment is conducted. Methods where the charge is directly vaporized and mixed in the RCM reaction chamber have also been employed, but there is generally higher uncertainty for these experiments.

Typically, the charge and RCM reaction chamber are only heated to ~ 100 C due to issues associated with pretest fuel decomposition and mechanical seal degradation of the machine at higher temperatures. For gasoline relevant fuels a broad range of experimental pressures and equivalence ratios can be reached, e.g. x, y , respectively. For jet fuel, diesel and biodiesels only very dilute, low-pressure cases can be achieved, which are far from the conditions characteristic of operating IC engines. To extend the limitations of these experiments wet compression experiments have been suggested.

Wet Compression

In the wet compression method, fuel is directly loaded into the machine as suspended liquid droplets, so that pre-vaporized conditions are no longer needed. This approach can extend RCM experiments to liquid as well as gelled or solid fuels, granted that a sufficient amount of pre-test atomization can ensure rapid rates of vaporization. A schematic for wet compression experiments is shown in Figure 2.7, and is described below. It should be noted that the physics during the delay period are similar for both pre-heated and wet compression experiments, where phase change (i.e. condensation) can occur near the walls of the reaction chamber.

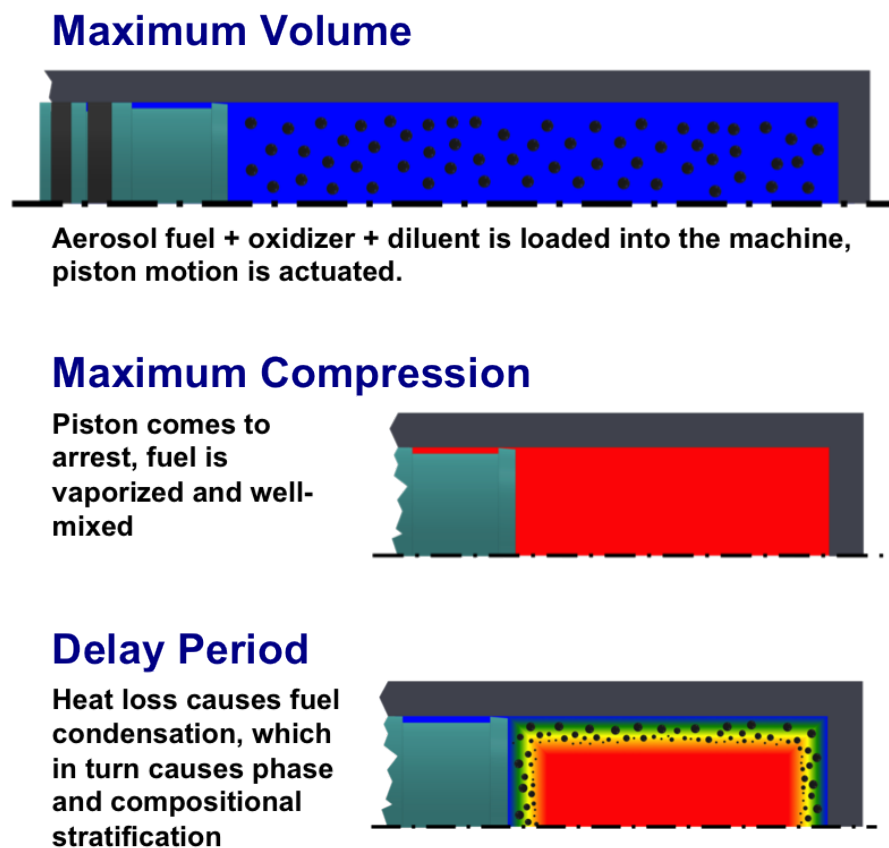


Figure 2.7: A mechanistic schematic of the wet compression process in RCM experiments.

Experiments are conducted by first loading the machine with a finely atomized (i.e. $D=4 - 8 \mu\text{m}$) fuel aerosol suspended in an oxidizer + diluent bath gas. Several methods are available to achieve such a fine fuel atomization and load the aerosol into the RCM. After the homogeneous, dense aerosol is loaded into the machine piston, the motion is actuated.

As the gas-phase is volumetrically compressed by the piston heat is transferred to the liquid droplets and vaporization ensues. Small droplets, with a high SAV, are ideal for rapid heat transfer, vaporization and diffusive oxidizer mixing rates. Previous computational studies have been conducted to investigate the physics of this process [116, 117], though little to no experimental data is currently available.

In a well-designed experiment the fuel is completely vaporized and well-mixed via rapid fuel diffusion by the end of compression, so that gas-phase chemical kinetics can be investigated. During the chemically active delay period phase-change effects are hypothesized to affect the thermal, phase and compositional stratification within the reaction chamber. As the thermal boundary layer propagates into the adiabatic core gases fuel condensation may occur near the wall. Preferential boiling/condensation in multi-component fuel surrogates could cause compositional stratification in both the gas and liquid phases across the reaction chamber as well as locally. The gas phase compositional gradient may enhance the stratification by driving a diffusive fuel flux to the cool walls of the reaction chamber.

The main goal of the current study is to assess the non-ideal, two-phase effects in the reaction chamber described above for a typical fuel surrogates over a range of conditions. This is achieved by extending the RCM MZM developed by Goldsborough et al. to include the effects of multi-phase physics. This will aide with machine and experimental design, as well as give insight into the

physical limitations of these experiments. This reduced-order modeling approach is adopted to be computationally efficient so that the new model could also be used to pass volumetric expansion rates to an adiabatic core HRM for the comparison of chemical kinetics mechanisms to RCM wet compression experimental data. The details of the model formulation are the subject of the next chapter.

Chapter 3

Phase-Change Modeling

Modeling Approach

The formulation for the new multi-phase, multi-zone model (MP-MZM) has been developed by extending the reduced-order RCM model of Goldsborough et al. [36] to include phase-change and compositional stratification effects.

As can be seen in Figure 3.1 the model splits the RCM into three computational zones; the reaction chamber, a crevice volume and a tapered gap. The reaction chamber is further discretized into a one-dimensional mesh, where the species continuity and energy equation are solved at each volume element for both the gas and liquid phases. The 1D mesh ensures that the surface area to volume ratio of the reaction chamber is maintained throughout the piston compression and ensuing delay period. The effects of piston motion are modeled as a mesh compression process, where an arbitrary piston trajectory may be prescribed. Since convective velocities are assumed to be minimized in the reaction chamber by the use of creviced pistons, energy and species transport are modeled across the mesh via a diffusion limited process.

Flow to the piston crevice is determined by assuming pressure equilibrium across the three zones and solving the transient species and energy equation in the tapered gap. In this region fluid velocities are high, so that convective heat and species transfer along the piston circumference and cylinder wall are modeled using scaling arguments for developing, turbulent flow. The transient species, momentum and energy equations are then solved in the piston crevice. Here Nusselt correlations along with Reynolds and Sherwood analogies are used to model convective heat transfer, fluid shear and species transport to the walls.

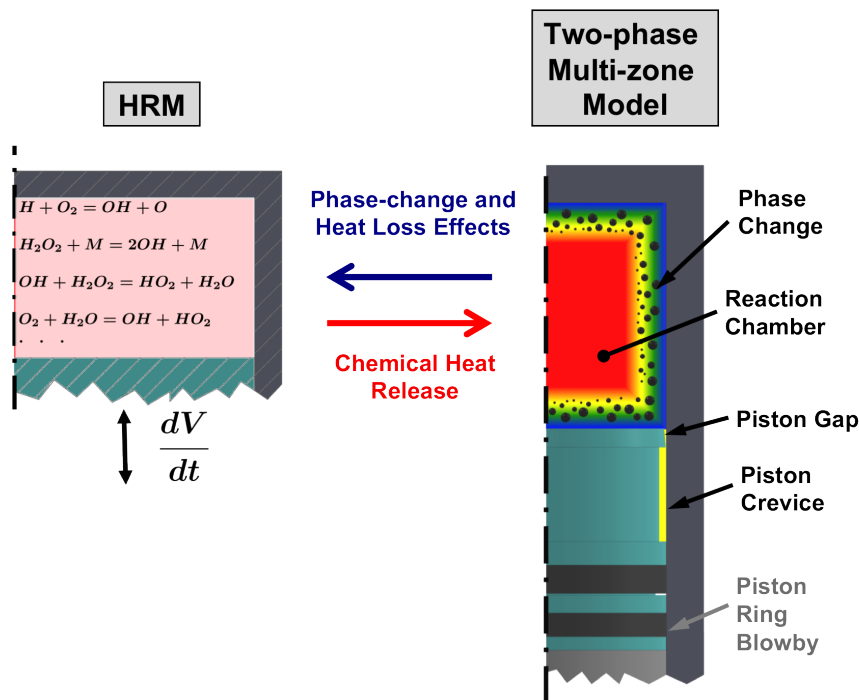


Figure 3.1: A graphical representation of the MP-MZM communication with an HRM used to simulate detailed chemical kinetics.

Dispersed liquid-gas interactions are not taken into account in the gap and crevice regions, where work is ongoing to take these effects into account. An additional computational zone is included in the single-phase MZM behind the piston seals (i.e. downstream of the crevice) to account for gas blowby, which has been found to be important for accurate comparisons between MZM simulation results and experimental pressure traces. However for this study blowby modeling has been neglected, as the MP-MZM is not compared to experimental data sets.

The MZM modeling approach was recently validated against spatially resolved CFD simulations as well as experimental pressure traces for gas-phase experiments, where good agreement was observed for both reacting and non-reacting conditions under single-stage as well as multi-stage conditions. Here the focus is on incorporating phase-change and associated effects, e.g. species diffusion transport, in order to investigate phenomena that may occur with experiments utilizing heavy, involatile fuels.

For this work, attention is focused on utilizing a formulation that has the

capability to simulate large chemical kinetic mechanisms, as opposed to resolving the complex multi-phase physics, e.g. droplet migration and induced fluid dynamics. For instance, computationally-efficient scaling arguments for convective heat transfer and fluid shear have been applied in the piston gap and crevice regions to retain tractability over Navier-Stokes approaches utilizing turbulence models (e.g. RANS and LES). Also, closed form solutions for droplet vaporization and condensation have been used to retain numerical stability within the code as well as reduce simulation times. Errors associated with resolving the fluid dynamics and phase-change physics by the use of these reduced-order approximations is expected to be modest; this assessment will be explored further in the following chapter. The utility of this model however, is assessed by the ability to predict a well-defined experimental gas temperature and composition that may be passed to a chemical kinetics solver in addition to providing confidence in the adiabatic core modeling approach by modeling the extent of RC stratification. The tuning of the rate expressions used by the reduced-order sub-models presents an opportunity for future work as more experimental data sets and high-level simulation results become available for involatile fuel/aerosol RCM experiments.

The remainder of this chapter explores the mathematical formalism of the new MP-MZM, where a section is devoted to each computational zone. First the multi-phase RC model is discussed, which is then followed by a description of the piston gap and crevice sub-models.

Reaction Chamber

Governing Equations

In the new MZM the reaction chamber is modeled as a fully transient, two-phase mixture of liquids and gases. The species continuity, momentum and energy equations Eqs. (3.1-3.3) are written below for the gas mixture in the RC. The gas mixture continuity can also be trivially obtained by summing Eq. (3.1) over all species in the mixture. The governing equations for the RC liquid phase are introduced later in this chapter.

$$\frac{\partial}{\partial t}[\rho_j] = -(\nabla \cdot \rho_j \vec{v}) - (\nabla \cdot \vec{J}_j) + \dot{n}_{PC,j} N_d'' \quad (3.1)$$

$$\frac{\partial}{\partial t}[\rho v] = -(\nabla \cdot \rho \vec{v} \vec{v}) - (\nabla P) - (\nabla \cdot \vec{\tau}) \approx 0 \quad (3.2)$$

$$\begin{aligned} \sum_{j=1}^{N_{sp}} \frac{\partial}{\partial t}[\rho u]_j = & - \sum_{j=1}^{N_{sp}} (\nabla \cdot \rho_j h_j \vec{v}) - (\nabla \cdot \vec{q}) - \sum_{j=1}^{N_{sp}} (\nabla \cdot h_j \vec{J}_j) + \dot{Q}_{rxn}'' \\ & + \dot{W}_{pist}'' - \dot{Q}_{PC} N_d'' \end{aligned} \quad (3.3)$$

Thermal, compositional and phase stratification are modeled symmetrically across the reaction chamber (from the adiabatic core gases to the reaction chamber surfaces) in a single dimension, i.e., effective radial direction. Heat diffusion through the RC gas is allowed as thermal gradients develop from the hot adiabatic core gases to the cooler reaction chamber walls, while convective velocities across the RC are assumed to be minimal due to the use of creviced pistons. Condensation of low-vapor pressure fuels, in the thermal boundary layer also generates gas-phase composition gradients within the reaction chamber which drives species diffusion. The species and energy transport due to this effect are taken into account in Eqs. (3.1) and (3.3).

Pressure equilibrium is spatially assumed throughout the RC volume, as well

as between the RC and gap and crevice volumes due to high sonic velocities. Detailed simulations have shown that a small, but finite pressure gradient exists across the piston gap from the RC to crevice region during piston compression, especially for geometries that have a small gap clearance (e.g. $l_g < 0.2$ mm) [36, 251, 252]. Capturing the effect of this small differential is important to accurately characterize the rate of mass transfer and thus enthalpic losses from the reaction chamber to the piston crevice, and this was successfully achieved in the previous formulations of the MZM [36, 113]. Unfortunately it was not possible to implement a similar approach in the current model due to issues associated with numerical instability under multi-phase conditions. The errors associated with modeling the multiple zones in the RCM as pressure equilibrated are assessed in the next chapter.

The MP-MZM formulation assumes that the creviced piston design is completely effective at suppressing gas motion inside the reaction chamber i.e., the roll-up vortex, and the bulk gas velocity in the RC is set to a constant, null value. Combined with the assumption and pressure equilibrium in the RC this leads to a trivial solution of the momentum equation, Eq. (3.2). The bulk fluid velocity term in Eqs. (3.1) and (3.3) accounts for the flow from the reaction chamber to the gap region. This velocity is discontinuously non-zero at the RC-gap boundary; further details of how the velocity is calculated are provided in the following section.

The effects of piston compression, chemical reaction and phase change are included in the governing equations as source/sink terms. The rate of boundary work done on the gas is distributed evenly over the entire RC and is prescribed using a piston trajectory as input, as will become apparent shortly. Chemical heat release can also be modeled in the adiabatic core by communication with an HRM where chemical kinetics are simulated; however, changes in species concentration are not fed back to the MZM. A more detailed formulation may also be developed, where varying rates of chemical reactions are calculated

across the RC. In this thesis, however, chemical reactions are computationally suppressed, and models to account for the exothermicity effects of fuel decomposition and oxidation during the experiment are planned to be explored in forthcoming studies. The source terms for species and energy fluxes into/out of the gas phase due to vaporization/condensation are prescribed from an analysis of the local transport to/from the liquid mass. Here analytic expressions for energy and species transport are utilized where the locally average gas and liquid thermodynamic states are employed as boundary conditions.

To determine proper, time-dependent boundary conditions for droplet vaporization/condensation, “bulk” liquid governing equations are applied across the reaction chamber volume. The liquid species continuity, momentum and energy equation are given by Eqs. (3.4-3.6), respectively. An equation for droplet number density (i.e. RC spatial aerosol density distribution) is given by Eq. (3.7), where droplets are allowed to be transferred to the gap region from the RC.

$$\frac{\partial}{\partial t}[\rho]_{j,l} = - \left(\nabla \cdot \left(\frac{\chi_l}{\chi_v} \right) \rho_{j,v} \vec{v} \right) - \dot{n}_{PC,j} N_d'' \quad (3.4)$$

$$\frac{\partial}{\partial t}[\rho v]_l \approx 0 \quad (3.5)$$

$$\sum_{j=1}^{N_{sp}} \frac{\partial}{\partial t}[\rho u]_{j,l} = - \sum_{j=1}^{N_{sp}} \left(\nabla \cdot \left(\frac{\chi_l}{\chi_v} \right) \rho_{j,v} h_{j,l} \vec{v} \right) + \dot{Q}_{PC} N_d'' \quad (3.6)$$

$$\frac{\partial}{\partial t}[N_d''] = - \left(\nabla \cdot \frac{1}{\rho_l V_d} \left(\frac{\chi_l}{\chi_v} \right) \rho_v \vec{v} \right) \quad (3.7)$$

The liquid phase flux equations are formulated under the assumption that suspended droplets are sufficiently small to closely follow the gas-phase streamlines (i.e. $Stk \ll 1$). The effect of this assumption is that liquid velocities are equivalent to gas-phase velocities, and aerosol concentrations remain constant along a gas-phase streamlines from the RC to the gap. Another effect of the low Stokes number assumption is that local droplet advective velocities are

negligable near the phase interface, the effects of this will be discussed later in this chapter. Future work could be conducted to investigate the effects of large Stokes number, aerosol dynamics inside the RCM as validation data for aerosol experiments becomes available.

Eqs. (3.4-3.7) are applied to the “bulk”, RC liquid phase in the same sense that Eqs. (3.1-3.3) are applied to the “bulk”, gas phase in the RC. Combined, both sets of conservation equations are sufficient to model the phase, thermal and compositional stratification throughout the RCM RC, as well as the time-dependant condition of the adiabatic core region. The gas and liquid phase conservation equations are coupled due to the phase-change source/sink terms. Closure of the conservation equations is achieved by resolving the sub-RC-scale local droplet physics, which is discussed later in this chapter.

Solution Scheme

Solutions to the gas-phase governing equations are obtained by discretizing Eqs. (3.1) and (3.3) over a one-dimensional mesh of finite volume elements. The volume elements are configured as concentric cylinders, where mesh element geometries that exhibit the same SAV as the reaction chamber have been shown to most adequately match the stratification profiles in detailed CFD simulations [36]. A single computational mesh is used, where each volume element contains all of the physical information of both phases. Conceptually it is easier to construct a separate but identical mesh for each of the phases, where communication between the gas and liquid mesh is achieved through the phase change source/sink terms. This is shown in Figure 3.2, where the fluxes and cell volume, averaged properties are graphically depicted.

To obtain a spatially discretized set of governing equations for the gas and

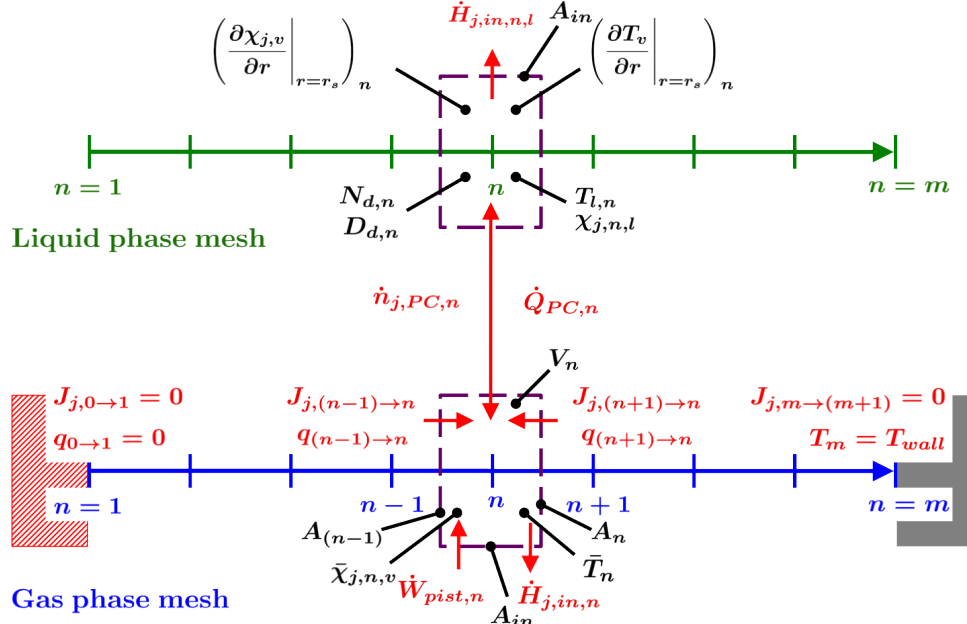


Figure 3.2: A schematic of the reaction chamber computational mesh.

liquid phases, the flux equations discussed in the previous section are integrated over an arbitrary volume element. This results in the gas-phase integrated species continuity and energy equation given by Eqs. (3.8) and (3.9), respectively.

$$\frac{\partial}{\partial t} \left[\int \rho_j \, dV_n \right] + \sum_{k=1}^{N_{surf}} \oint \left[(\rho_j \vec{v} \cdot \hat{n}_{k,n}) + (\vec{J}_j \cdot \hat{n}_{k,n}) \right] d\vec{S}_{k,n} = \dot{n}_{PC,j,n} N_{d,n} \quad (3.8)$$

$$\begin{aligned} \frac{\partial}{\partial t} \left[\sum_{j=1}^{N_{sp}} \int \rho_j u_j \, dV_n \right] + \sum_{k=1}^{N_{surf}} \oint \left[\sum_{j=1}^{N_{sp}} (\rho_j h_j \vec{v} \cdot \hat{n}_{k,n}) + (\vec{q} \cdot \hat{n}_{k,n}) + \sum_{j=1}^{N_{sp}} (h_j \vec{J}_j \cdot \hat{n}_{k,n}) \right] d\vec{S}_{k,n} \\ = \dot{Q}_{rxn,n} + \dot{W}_{pist,n} - \dot{Q}_{PC,n} N_{d,n} \end{aligned} \quad (3.9)$$

In addition, the volume integrated liquid-phase species continuity, energy and droplet population equation are given by Eqs. (3.10-3.12), respectively.

$$\frac{\partial}{\partial t} \left[\int \rho_{j,l} \, dV_n \right] + \sum_{k=1}^{N_{surf}} \oint \left[\left(\frac{\chi_l}{\chi_v} \right) \rho_{j,v} \vec{v} \cdot \hat{n}_{k,n} \right] d\vec{S}_{k,n} = -\dot{n}_{PC,j,n} N_{d,n} \quad (3.10)$$

$$\frac{\partial}{\partial t} \left[\sum_{j=1}^{N_{sp}} \int [\rho u]_{j,l} dV_n \right] + \sum_{k=1}^{N_{surf}} \oint \left[\sum_{j=1}^{N_{sp}} \left(\frac{\chi_l}{\chi_v} \right) \rho_{j,v} h_{j,l} \vec{v} \cdot \hat{n}_{k,n} \right] d\vec{S}_{k,n} = \dot{Q}_{PC,n} N_{d,n} \quad (3.11)$$

$$\frac{\partial}{\partial t} \left[\int N_d'' dV_n \right] + \sum_{k=1}^{N_{surf}} \oint \left[\frac{1}{\rho_l V_d} \left(\frac{\chi_l}{\chi_v} \right) \rho_v \vec{v} \cdot \hat{n}_{k,n} \right] d\vec{S}_{k,n} = 0 \quad (3.12)$$

Here the time rate change of the conserved quantities are evaluated by applying the Reynolds transport theorem. The fluxes at the boundaries of each volume element are evaluated using the divergence theorem. The path integrals shown in the flux terms of the volume integrated, governing equations are summed over each of the k flux boundaries of the volume element, where $\vec{S}_{k,n}$ is the flux boundary surface area vector and $\hat{n}_{k,n}$ is an outward pointing directional vector for the k_{th} flux boundary of the n_{th} volume element. Special attention to this detail is provided here because these discrete flux boundaries do not necessarily correspond to geometric surfaces of the volume element. For the one-dimensional heat and species diffusion from the core gases to the wall, however, this is indeed the case. Heat and species diffusive fluxes are calculated between each volume element and it's two nearest neighbors, where the flux boundary is taken as the geometric interface between the two elements.

The flux boundary for the bulk gas and liquid flows to the gap is more empirically implemented. Detailed simulations suggest that gas is transported from the entire RC volume to the gap region as opposed to only gases in the thermal boundary layer, where high temperature gap and crevice regions have been reported [36, 251, 252]. For the formulation used in this thesis, bulk gas-phase velocities are disallowed between intra-RC volume elements, so that only fluid with a geometric boundary in common with the gap-RC interface would be allowed to be transferred to the gap region. To retain proper correspondence with detailed CFD results for the gap and crevice regions, each volume element in the mesh is given a virtual flux boundary to the gap region, where bulk, pressure-driven flows are resolved. Geometrically, the gap flux

boundary is orthogonal to the direction of radial RC transport, and heat and species are not conducted to the from the RC to the gap.

The discretized conservation equations for an arbitrary volume element that account for all allowed rates of transport are given for the gas phase by Eqs.

(3.13) and (3.14).

$$\frac{\partial}{\partial t}[n]_{j,n} = -\dot{n}_{j,in,n} \hat{g} - \sum_{k=1}^{N_{surf}} [J_j A]_{n,k} \hat{r} + \dot{n}_{PC,j,n} N_{d,n} \quad (3.13)$$

$$\begin{aligned} \sum_{j=1}^{N_{sp}} \frac{\partial}{\partial t}[nu]_{j,n} = & - \sum_{j=1}^{N_{sp}} [\dot{n}_{in} h]_{j,n} \hat{g} - \sum_{k=1}^{N_{surf}} \left[q + \sum_{j=1}^{N_{sp}} [hJ]_j \right]_{n,k} A_{n,k} \hat{r} \\ & + \dot{Q}_{rxn,n} + \dot{W}_{pist,n} - \dot{Q}_{PC,n} N_{d,n} \end{aligned} \quad (3.14)$$

Similarly, the cell average liquid phase governing equations are given by Eqs.

(3.15-3.17).

$$\frac{\partial}{\partial t}[n]_{j,n,l} = - \left(\frac{\chi_{l,n}}{\chi_{v,n}} \right) \dot{n}_{j,in,n} \hat{g} - \dot{n}_{PC,j,n} N_{d,n} \quad (3.15)$$

$$\sum_{j=1}^{N_{sp}} \frac{\partial}{\partial t}[nu]_{j,n,l} = - \left(\frac{\chi_{l,n}}{\chi_{v,n}} \right) \sum_{j=1}^{N_{sp}} [\dot{n}_{in} h_l]_{j,n} \hat{g} + \dot{Q}_{PC,n} N_{d,n} \quad (3.16)$$

$$\frac{\partial}{\partial t}[N_d]_n = - \frac{1}{\rho_{l,n} V_{d,n}} \left(\frac{\chi_{l,n}}{\chi_{v,n}} \right) \dot{n}_{j,in,n} \hat{g} \quad (3.17)$$

Energy and species flows through the RC mesh and to the gap region are denoted by the directional vectors \hat{r} and \hat{g} , respectively. The methodology to account for the terms representing pressure-driven energy and species flows to the gap volume is presented in the following section. The source terms in the species continuity and energy equation for both phases due to phase change are discussed later in this chapter, where the sub-grid, droplet vaporization/condensation physics are resolved, and conservation equation closure is achieved. The remainder of this section is devoted to the methodology used to prescribe heat and species diffusion rates across the mesh, as well as the

boundary term for piston work.

Species and Energy Flux

As noted earlier, heat conduction is resolved between the nearest neighbor mesh nodes, where this statement is mathematically described by Eq. (3.18).

$$\sum_{k=1}^{N_{surf}} [qA]_{n,k} = q_{(n-1) \rightarrow n} A_{(n-1)} + q_{(n+1) \rightarrow n} A_n \quad (3.18)$$

Heat conduction rates are calculated by applying Fourier's law of conduction (i.e. Eq. (3.19)) to the mesh in the effective radial direction.

$$q = -k \frac{\partial T}{\partial r} \quad (3.19)$$

The combination of Eqs. 3.18 and (3.19) after evaluating the temperature gradient in Eq. (3.19) numerically over each neighboring element produces Eq. (3.20).

$$\begin{aligned} \sum_{k=1}^{N_{surf}} [qA]_{n,k} = & -k_{(n-1/2)} A_{(n-1)} \left(\frac{T_{(n-1)} - T_n}{\xi_n - \xi_{(n-1)}} \right) \\ & - k_{(n+1/2)} A_n \left(\frac{T_{(n+1)} - T_n}{\xi_{(n+1)} - \xi_n} \right) \end{aligned} \quad (3.20)$$

The thermal conductivities in Eq. (3.20) are evaluated at the heat flux boundary. The cell average gas temperatures are used to compute the mesh temperature gradient. The characteristic length scale ξ is used to numerically calculate the inter-cell temperature gradient, where this dimension is an effective distance between volume element centers.

A zero-gradient boundary condition is applied to the interior-most reaction chamber cell, which is given by Eq. (3.21). A constant wall temperature Dirchlet

boundary condition is applied at the opposite end of the computational mesh, i.e. at the exterior boundary of the outer-most cell, given by Eq. (3.22).

$$q_{(0 \rightarrow 1)} = 0 \quad (3.21)$$

$$T_m = T_{wall} \quad (3.22)$$

Experimental times are assumed to be sufficiently short and the thermal mass of the RCM RC is assumed to be sufficiently large so that the assumption of a constant wall temperature throughout is thought reasonable. However, this assumption may degrade under certain condition. For example a poorly designed RCM pre-heating system may cause internal temperature gradients within the reaction chamber walls, making a well-defined wall temperature difficult to prescribe. These effects are neglected for this study.

A formulation for Fickian species diffusion, given by Eq. (3.23), is prescribed analogously to the heat conduction formulation. Discretization of Eq. (3.23) over the RC mesh yields an equation for species diffusion rates into an arbitrary volume element given by Eq. (3.24).

$$J_j = -\mathcal{D} \frac{\partial \rho_j}{\partial r} \quad (3.23)$$

$$\begin{aligned} \sum_{k=1}^{N_{surf}} [J_j A]_{n,k} = & -\mathcal{D}_{(n-1/2)} A_{(n-1)} \left(\frac{\rho_{j,(n-1)} - \rho_{j,n}}{\xi_n - \xi_{(n-1)}} \right) \\ & - \mathcal{D}_{(n+1/2)} A_n \left(\frac{\rho_{j,(n+1)} - \rho_{j,n}}{\xi_{(n+1)} - \xi_n} \right) \end{aligned} \quad (3.24)$$

As with heat conduction a zero-gradient boundary condition is applied at the core node, where this is given by Eq. (3.25). A similar boundary condition is applied at the opposite end of the mesh, as shown by Eq. (3.26), so that species diffusion into the solid RC walls is prohibited.

$$J_{j,(0 \rightarrow 1)} = 0 \quad (3.25)$$

$$J_{j,(m \rightarrow m+1)} = 0 \quad (3.26)$$

Boundary Term

The effects of boundary work on the RC gas due to piston motion are emulated by a mesh compression process, which is taken into account by the \dot{W}_{pist} term. In this formulation the work done on the total reaction chamber gases is evenly distributed over the reaction chamber mesh volume elements. The compression work on the n_{th} mesh node is determined from the definition of boundary work given by Eq. (3.27).

$$\dot{W}_{pist,n} = -P \frac{d}{dt}[V]_n \quad (3.27)$$

Here the rate of change of each mesh element is prescribed as a volume weighted fraction of the total RC volume change rate, which is shown by 3.28.

$$\frac{d}{dt}[V]_n = \left(\frac{V_n}{V_{RC}} \right) \frac{d}{dt}[V]_{RC} \quad (3.28)$$

The rate of change of reaction chamber volume is computed using Eq. (3.29) and a prescribed piston trajectory. Piston trajectories are not typically measured in RCM experiments, however, they can be inferred from reaction chamber pressure traces; these usually vary significantly from facility to facility. The trajectory utilized in this study is a time dependent polynomial fit of the CWR trajectory obtained from [109], however the software is flexible to take any functional form for piston velocity as an input.

$$\frac{d}{dt}[V]_{RC} = -\frac{\pi}{4} B^2 v_{pist} \quad (3.29)$$

The combination of Eqs. (3.27-3.30) yields an expression suitable to calculate volume element work rates from an input piston trajectory, Eq. (3.30).

$$\dot{W}_{pist,n} = \frac{\pi}{4} B^2 \left(\frac{V_n}{V_{RC}} \right) P v_{pist} \quad (3.30)$$

In addition a source term is included in the gas-phase energy equation to account for the effects of chemical heat release. The rates of chemical heat release can be obtained from communication with a OD HRM, where the bulk heat release is applied throughout the entire reaction chamber, evenly distributed over the entire MZM RC mesh. The purpose of this is to account for the effects of multi-stage heat release, or exothermicity on the wall heat loss and crevice flows that are enhanced by “pre-ignition heat release”.

Pressure Equilibration

As stated previously the pressure across the gas phase RC mesh is assumed to be uniform, so that solution of the momentum equation is trivial. However as rates of energy and species transport from each mesh element are allowed to vary during the simulation, artificial pressure gradients can evolve across the RC mesh. In the current model this artifact is suppressed through a dynamic mesh rezoning, which is utilized to correct element volumes so that the coupled gas conservation equations and state equation are simultaneously solved. In previous MZM formulations an isentropic compression/expansion step was performed at each time step to achieve this. A slightly different approach is taken here, where the mesh cell isentropic volume change is prescribed as a coupled rate term. This method is outlined below.

The volume change of an arbitrary volume element to achieve pressure equilibrium at each time step throughout the mesh is prescribed by the

isentropic compression/expansion relation Eq. (3.31).

$$\Delta V_{PR,n} = \left(\frac{V_{RC}}{V_{RC} + \sum_{n=1}^m \Delta V_{PR,n}} \right) V_n \left(\frac{P_n}{\bar{P}_{RC}} \right)^{1/(\gamma_n-1)} - V_n \quad (3.31)$$

The above isentropic equation has been normalized so that there is no change in the total mesh volume after rezoning, and here \bar{P}_{RC} is the volume weighted average reaction chamber mesh pressure. The rate of volume change of each mesh volume is then calculated using a first-order backwards differencing scheme, given by Eq. (3.32).

$$\frac{d}{dt}[V]_{PR,n} = \frac{\Delta V_{PR,n}}{\Delta t} \quad (3.32)$$

The pressure rezoning rate is added to the volumetric change rate due to piston motion of each cell, and mesh pressure equilibrium is achieved. The boundary work on each cell due to the dynamic mesh rezoning is added as a source term to the discretized gas energy equation, and is given by Eq. (3.33).

$$\dot{W}_{PR,n} = - \left(\frac{U_{RC,v}}{U_{RC,v} + \sum_{n=1}^m \dot{W}_{PR,n} \Delta t} \right) \frac{1}{2} (P_n + \bar{P}_{RC}) \frac{d}{dt}[V]_{PR,n} \quad (3.33)$$

Where again the work rate is normalized to conserve the total gas-phase reaction chamber energy.

Dispersed Droplet Evaporation/Condensation

Governing Equations

As noted above a diffusion limited, sub-grid droplet vaporization/condensation model is employed to prescribe species and energy transfer rates between the

bulk liquid and gas phases, effectively closing the governing equations for the MP-MZM reaction chamber. The details of this model are discussed in this section.

In this formulation one-dimensional energy and species fluxes from a spherical, single-component liquid droplet are calculated through a quasi-steady, droplet-locally stratified gas phase. The single-droplet calculations are used to determine *average* aerosol phase change rates within each computational zone. Again, the effects of the droplet local, gas-phase stratification are not resolved by the “bulk” MP-MZM governing equations. The quasi-steady conservation of species and energy equations for the local gas-phase domain are given by Eq. (3.34) & (3.35). These equations are quasi-steady in the sense that the local gas domain instantaneously comes to equilibrium with changes in the liquid droplet. This assumption has been shown to produce modest errors under some conditions, these are assessed in the following chapter.

$$r^2 \rho v \frac{d\chi_f}{dr} = \frac{d}{dr} \left[r^2 \mathcal{D}_f \rho \frac{d\chi_f}{dr} \right] \quad (3.34)$$

$$r^2 \rho v \frac{d}{dr} [c_p T] = \frac{d}{dr} \left[\frac{k}{c_p} r^2 \frac{d}{dr} [c_p T] \right] \quad (3.35)$$

Here the subscript f is used to denote the single vaporizing fuel species. Ongoing work is being conducted to extend these equations to a tractable form for an arbitrary number of fuel species, where analytic solutions can be obtained. The formulation used in this study, however, is restricted to a single fuel species to retain computational efficiency. The Fourier conduction and Fickian diffusion terms in these equations are relatively straight-forward, and the bulk motion transport is included as an Eulerian reference frame is chosen for the growing/shrinking droplet. Here the ρv term accounts for transport through the traveling droplet surface boundary.

Additional constraints are needed to formally solve the droplet local governing equations. The first constraint applies is the assured satisfaction of the

local gas mixture (i.e. fuel + oxidizer + diluent) continuity equation at the boundary surface. This is achieved by invoking Eq. (3.36).

$$\rho_s v_s = \rho_{f,s} v_s + J_{f,s} \quad (3.36)$$

The left hand side (LHS) of Eq. (3.36) represents the bulk gas-phase mixture molar flux at the droplet surface. The right hand side (RHS) accounts for the bulk and Fickian species flux away from the droplet, so that the local diluent + oxidizer is effectively stagnant.

The constraint that energy is conserved at the droplet surface is also imposed. This is given by Eq. (3.37).

$$k_g \left. \frac{\partial T}{\partial r} \right|_{r=r_s} = \rho_l (h_{l,f} + \Delta h_{vap,f}) \frac{\partial r_s}{\partial t} \quad (3.37)$$

Where the LHS of Eq. (3.37) corresponds to the conductive heat flux into the droplet from the gas-phase domain, and the RHS is the heat released/absorbed by the liquid droplet due to phase change. It should be noted that species and energy fluxes through the droplet surface due to droplet internal compositional and thermal gradients are neglected in Eqs. (3.36) and (3.37), respectively. Under certain conditions neglecting these terms can produce substantial error, where this will be assessed in the following chapter.

The gas-phase domain species equation is bounded by the two boundary conditions shown below.

$$\chi_f(r = \infty) = \bar{\chi}_f \quad (3.38)$$

$$\chi_f(r = r_s) = \chi_{f,s} = \frac{P_{f,s}}{P} \quad (3.39)$$

The Dirichlet boundary condition shown in Eq. (3.38) specifies the far-field, gas-phase fuel composition. Practically, for this formulation the “infinite radius” is taken as half of the spacing between a droplet and its nearest neighbor, and

the far-field fuel fraction is taken as the bulk average computational volume fuel mole fraction. At the droplet surface the gas-phase fuel fraction is specified by enforcing phase equilibrium at the boundary, where gas kinetic effects are neglected at the phase interface. The models used to specify partial pressure are discussed with the other thermophysical and transport property models in Appendix A.

The gas domain energy equation is spatially bounded by Eqs. (3.40) and (3.41).

$$T(r \leq r_s) = T_l \tag{3.40}$$

$$T(r = \infty) = \bar{T} \tag{3.41}$$

The surface temperature, which is continuous through the surface, is obtained from the integrated bulk liquid phase energy equation for each RC mesh node. The far-field temperature of the gas is obtained in the same way; from the integrated bulk gas-phase equations.

The conservation ODEs are solved using a separation of variables methodology, and a detailed account of this fairly straight-forward process is not offered in this manuscript. For the detailed mathematical rigor used to obtain analytic solutions to the conservation equations constrained by the above boundary conditions the reader is directed to ref. [267], where a succinct analysis is presented.

Analytic Solutions

Solutions to the droplet equations for the rate of energy and species transfer between the phases are given by Eqs. (3.42-3.44).

$$\forall j \neq f : \dot{n}_{j,PC} = 0 \quad (3.42)$$

$$\dot{n}_{f,PC} = \rho_s \mathcal{D}_{f,s} A_s \frac{\ln(1 + B_M)}{r_s} \quad (3.43)$$

$$\dot{Q}_{PC} = k_s A_s \frac{(T_{inf} - T_l)}{r_s} \frac{\ln(1 + B_T)}{B_T} - \dot{n}_{PC}(h_l + \Delta h_{vap}) \quad (3.44)$$

As a result of the single-component fuel assumption, phase change of a single fuel species is allowed (i.e. Eq. (3.42)), and the rates of species vaporization or condensation are given by Eq. (3.43). The transport and thermophysical properties in Eqs. (3.43) and (3.44) are evaluated for the gas-phase mixture at the droplet surface, excluding liquid properties denoted by the subscript l . The areas and radii in Eqs. (3.43) and (3.44) are the time dependent droplet surface area and radius stored in the mesh node where the droplet model is applied. In literature B_M , which appears in Eq. (3.43), is typically referred to as the Spalding mass transfer number. Here it is utilized in molar based form, i.e. Eq. (3.45).

$$B_M = \frac{\chi_{f,s} - \bar{\chi}_f}{1 - \chi_{f,s}} \quad (3.45)$$

A slightly modified solution for the thermal transfer number B_T appearing in Eq. (3.44) is used in this formulation. The modified term is given by Eq. (3.46), and was originally derived for droplets in a locally convective environment in ref. [267]. This modified term is utilized here to better match detailed simulation

results, which are presented in the next Chapter.

$$B_T = (1 + B_M)^{(c_{p,f}/(c_p Le))_{film}} \quad (3.46)$$

In Eq. (3.46), the thermal transfer number is dependent on the Spalding number as well as the gas film mixture specific heat, fuel specific heat and fuel Lewis number. Film properties are evaluated at the “one-third rule” film condition suggested by [267]. For example, the film temperature is determined by $T_s + 0.33(T_{inf} - T_s)$.

Through the droplet analysis Eqs. (3.43) and (3.44) are used to close the multi-phase species and energy equation in the RC mesh. These closure terms for the RC are given by Eqs. (3.47) and (3.48).

$$\dot{n}_{j,PC,n} = \begin{cases} \rho_{s,n} \mathcal{D}_{f,s,n} A_{s,n} \frac{\ln(1+B_{M,n})}{r_{s,n}} & \text{if } j = f, \\ 0 & \text{otherwise} \end{cases} \quad (3.47)$$

$$\dot{Q}_{PC,n} = k_{s,n} A_{s,n} \frac{(T_n - T_{l,n})}{r_{s,n}} \frac{\ln(1 + B_{T,n})}{B_{T,n}} - \dot{n}_{f,PC,n} (h_{f,l,n} + \Delta h_{vap,f,n}) \quad (3.48)$$

Piston Gap

Governing Equations

The piston gap region, which is the volume adjacent to the tapered section on the piston, is modeled as a fully transient 0D “black box” style control volume, where the complex two-phase fluid dynamics are calculated by using reduced-order methods. Since high, turbulent gas velocities are present in this region, the heat transfer to the reaction chamber wall and piston surfaces is assumed to be

controlled by convective transport. A low Stokes number assumption is invoked in a similar fashion as is applied to the reaction chamber, which has the effect making the bath gas and droplet velocities equivalent. The validity of this assumption has yet to be determined due to the lack of simulated or experimental data for aerosol flows within these types of geometries. In contrast to previously developed MZMs, the gap inlet and exit flows are determined by assuming pressure equilibrium between the RC, gap and crevice volumes. The mathematical rigor of this process is described in the next subsection.

A combined equation for gap momentum is applied to the gap volume, which is given by Eq. (3.49). The *tot* notation is used here to denote both the liquid + vapor phases. Also, the *g* notation is used to signify values corresponding to the volumetric gap center, while *in* and *ex* represent variables at the RC-gap and gap-crevice boundaries, respectively.

$$\frac{d}{dt}[n_{tot}v]_g = \sum_{j=1}^{N_{sp}} \left[\sum_{n=1}^m \dot{n}_{j,in,n,tot} v_{in,n} \left(\frac{\chi_{l,n}}{\chi_{v,n}} + 1 \right) - \dot{n}_{j,ex,tot} v_{ex} \left(\frac{\chi_{l,g}}{\chi_{v,g}} + 1 \right) \right] - \tau A_s \approx 0 \quad (3.49)$$

The gap momentum, for both phases, is assumed to be quasi-steady, where this assumption has previously been validated for single-phase flows in [36]. In the previous formulation, however, fluid shear on the RC walls and piston crown were taken into account, where this effect is neglected in the current formulation. Also, a discrete pressure gradient was resolved across the gap length and the momentum equation was solved to determine the rate of pressure driven flows from the reaction chamber to the crevice volume. Again, this pressure differential is neglected in the current formulation, where flow is forced to the gap and crevice regions to ensure pressure equilibrium throughout the three regions. An attempt to account for these effects in the multi-phase simulations was unsuccessful due to unresolvable numerical instabilities produced by the solution scheme. In the formulation used for this study the gap momentum equation is

trivially solved, and offers no new insight into the physics of the experiment.

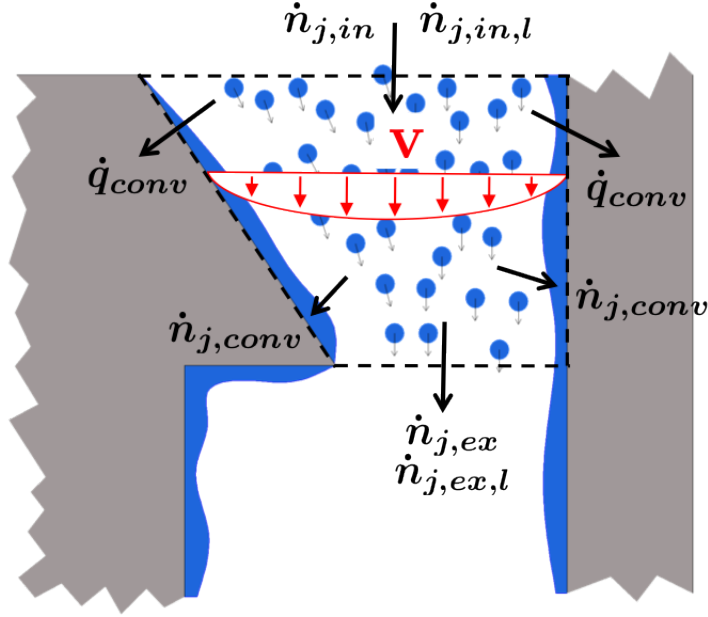


Figure 3.3: A schematic of the multi-phase flow through the piston gap.

The remaining conservation equations are applied to the gap separately for each of the phases. The gas-phase conservation of species and energy are given by Eqs. (3.50) and (3.51), respectively.

$$\frac{d}{dt}[n]_{j,g} = \sum_{n=1}^m \dot{n}_{j,in,n} - \dot{n}_{j,ex} + \dot{n}_{j,PC,g} \quad (3.50)$$

$$\begin{aligned} \sum_{j=1}^{N_{sp}} \frac{d}{dt}[nu]_{j,g} = & \sum_{j=1}^{N_{sp}} \left[\sum_{n=1}^m \dot{n}_{j,in,n} \left(h_{j,n} + \frac{v_{in,n}^2}{2} \right) - \dot{n}_{j,ex} \left(h_{j,g} + \frac{v_{ex}^2}{2} \right) \right] \\ & - \dot{Q}_{conv,g} - \dot{Q}_{PC,g} N_{d,g} \end{aligned} \quad (3.51)$$

The liquid species continuity and energy equation along with the droplet population number equation are given by Eq. (3.52)-(3.54), respectively.

$$\frac{d}{dt}[n]_{j,g,l} = \sum_{n=1}^m \left(\frac{\chi_{v,n}}{\chi_{l,n}} \right) \dot{n}_{j,in,n} - \left(\frac{\chi_{v,g}}{\chi_{l,g}} \right) \dot{n}_{j,ex} - \dot{n}_{j,PC,g} \quad (3.52)$$

$$\sum_{j=1}^{N_{sp}} \frac{d}{dt} [nu]_{j,g,l} = \sum_{j=1}^{N_{sp}} \left[\sum_{n=1}^m \left(\frac{\chi_{v,n}}{\chi_{l,n}} \right) \dot{n}_{j,in,n} h_{j,n,l} - \left(\frac{\chi_{v,g}}{\chi_{l,g}} \right) \dot{n}_{j,ex} h_{j,g,l} \right] + \dot{Q}_{PC,g} \quad (3.53)$$

$$\begin{aligned} \frac{d}{dt} [N]_{d,g} = & \sum_{n=1}^m \frac{1}{\rho_{l,n} V_{d,n}} \sum_{j=1}^{N_{sp}} \left(\frac{\chi_{v,n}}{\chi_{l,n}} \right) \dot{n}_{j,in,n} h_{j,n,l} \\ & - \frac{1}{\rho_{l,g} V_{d,g}} \sum_{j=1}^{N_{sp}} \left(\frac{\chi_{v,g}}{\chi_{l,g}} \right) \dot{n}_{j,ex} h_{j,g,l} \end{aligned} \quad (3.54)$$

Figure 3.3 illustrates the mechanisms of species and energy transport that are modeled in the piston gap region by the MP-MZM. As was discussed earlier, species are transferred to the gap from each RC volume elements, where gas-phase molar flow is determined by invoking pressure equilibrium between the RC and gap and liquid is transferred assuming a low Stokes number, aerosol flow. An exactly analogous methodology is used to transport gas and liquid species from the gap to the crevice region. The energy equation is constructed accounting for the enthalpy exchange of the gap with the RC and crevice regions, and the methodology for including the convective sink term will be described later in this section. The phase-change source/sink terms are evaluated by assuming convective mass transfer in a manner similar to the convective heat loss, and this is described shortly..

Since varying rates of droplet vaporization exist throughout the RC mesh and aerosol from each of these cells is passed to the gap region, a polydispersed situation (i.e. distribution of droplet sizes) exists in the gap region, even though a mono dispersed aerosol is modeled in each RC volume element. The current formulation does not have the capability to model polydisperse aerosols. As such, a single *effective* droplet size for the gap is passed to the sub-grid droplet phase change model, and is prescribed by Eq. (3.55).

$$D_g = \left[\frac{3}{4\pi N_{d,g}} \sum_{j=1}^{N_{sp}} \frac{n_{j,g,l}}{\rho_{j,l,g}} \right]^{1/3} \quad (3.55)$$

The gap droplet diameter is obtained from the “bulk” liquid species equation. While this may introduce discrepancies between the MP-MZM and the true physical process, this approach is taken so that consistency is achieved between the bulk “black box” conservation equations and the sub-grid droplet phase change model. The multi-phase physics in this region is complex and as more validation cases become available the modeled physics in this region can be better refined.

Gap Velocities

Pressure equilibrium is dynamically achieved between the RC, gap and crevice gases where the ideal gas equation of state (i.e. Eq. (3.56)) is utilized to compute the flow rates necessary for this, via Eqs. (3.57) and (3.58), respectively.

$$\frac{1}{P} \frac{dP}{dt} + \frac{1}{V} \frac{dV}{dt} = \frac{1}{n} \frac{dn}{dt} + \frac{1}{T} \frac{dT}{dt} \quad (3.56)$$

$$\dot{n}_{in} = \bar{\rho}_{RC} A_{x,in} v_{in} = n_g \left[\frac{1}{P_g} \frac{dP_{RC}}{dt} - \frac{1}{T_g} \frac{dT_g}{dt} \right] + \dot{n}_{ex} - \dot{n}_{PC} + \dot{n}_{in}^* \quad (3.57)$$

$$\dot{n}_{ex} = \rho_g A_{x,ex} v_{ex} = n_c \left[\frac{1}{P_c} \frac{dP_{RC}}{dt} - \frac{1}{T_c} \frac{dT_c}{dt} \right] + \dot{n}_{ex}^* \quad (3.58)$$

Three key assumptions are made while prescribing the molar gap flow rates. First, inviscid flow the gap the gap is assumed for the purpose of evaluating inlet and exit velocities, where this assumption is relaxed while calculating convective heat transfer rates as will become apparent shortly. The consequences of this assumption are assessed in the following chapter through comparisons to a previous MZM formulation. Also, the volume of gas is assumed to be temporally constant throughout the simulation. While the geometric volume of the gap and crevice region is held constant, the partial occupation of this volume by varying amounts of liquid phase species makes the above statement approximately

correct. This effect is thought to be negligible for the conditions explored here. Finally, the rate of pressure change is taken to be equivalent to the RCM RC in all regions of the model. This approach can be difficult to implement as there is no coupling between small, artificial pressure differences that develop due to numerical errors. Using this formulation, these artificial gradients can evolve between the zones during the solution procedure where this results in physically, nonsensical simulation results.

To reduce the extent of this error across the gap control volume a crude, but effective pressure-velocity scheme is developed. The methodology of this scheme is to correct the molar flow rates given by Eq. (3.57) & (3.58) by coupling the mass flow term to inter-zone pressure gradients. This is achieved by the use of Eq. (3.59) & (3.59) below.

$$\dot{n}_{in}^* = \frac{V_g}{R_u T_g} \frac{d}{dt} [P_{RC} - P_g] \quad (3.59)$$

$$\dot{n}_{ex}^* = \frac{V_c}{R_u T_c} \frac{d}{dt} [P_{RC} - P_c] \quad (3.60)$$

These equations have been derived from the standard form of the ideal gas equation, and effectively give the rate of mass flow to each of the regions if pressure gradients happen to develop at the flux boundaries. The pressure change rate term is evaluated using a numerically stable, high-order backwards differencing scheme.

Convective Heat Transfer

The convective heat transfer within the gap from the gas to the RCM RC walls and piston crown is calculated using a modified Newtonian cooling expression given by Eq. (3.61), which makes use of the gap log-mean temperature-difference

given by Eq. (3.62).

$$\dot{Q}_{conv,g} = [h_{conv}A_s\text{LMTD}]_g \quad (3.61)$$

$$\text{LMTD}_g = \frac{(\bar{T}_{RC} - T_{wall}) - (T_g - T_{wall})}{\ln \left[\frac{T_g - T_{wall}}{\bar{T}_{RC} - T_{wall}} \right]} \quad (3.62)$$

The convection coefficient is evaluated via a Nusselt correlation given by Eq. (3.63).

$$\text{Nu}_g = \frac{h_{conv,g}\zeta_g}{k_g} = 7.54 + \frac{0.028(\zeta_g/l_g)\text{Pr}_g\text{Re}_g}{1 + 0.011[(\zeta_g/l_g)\text{Pr}_g\text{Re}_g]^{2/3}} \quad (3.63)$$

The gap Nusselt correlation is for turbulent, developing flow in an annular geometry [268], where the parameters in Eq. (3.63) are fit based on data found in the same source. Properties are evaluated at the gas-phase film temperature $0.5(0.5(\bar{T}_{RC} + T_g) + T_{wall})$, and the Reynolds number is calculated using an average of the inlet and exit velocities. The characteristic length of the gap ζ_g is taken as the mean hydraulic diameter of the gap. Convective heat transfer from the liquid phase to the RCM surfaces is neglected as the liquid surface area in contact with the RC wall and piston is assumed to be minimal. It is also assumed that the presence of the liquid droplets do not affect the validity of the gas phase Nusselt correlation.

Phase Change

In the gap fuel condensation is assumed to occur on the RCM surfaces as high convective velocities transport gas-phase fuel to the cool walls. The liquid film on the cylinder walls and piston crown is assumed to be in thermodynamic (i.e.

phase) equilibrium at the wall temperature.

For this approach, convective species transfer rates from the bulk gas to the walls are calculated by Eq. (3.64) in an analogous fashion to convective heat transfer rates; by use of a mean mass transfer coefficient.

$$\dot{n}_{j,PC,g} = [h_{m,g} A_s LM\rho D]_g \quad (3.64)$$

Where $LM\rho D$ is the molar density analogy to Eq. (3.62), and the average mass transfer coefficient is evaluated from the Sherwood number, i.e. Eq. (3.65).

$$h_{m,g} = \frac{Sh_g \mathcal{D}_j}{\zeta_g} \quad (3.65)$$

Again, a low Stokes number approximation is made in the gap, and it is also assumed that the presence of liquid particles in the flow do not influence the gas-phase fluid dynamics. In light of these assumptions a mass analogy is used to evaluate the Sherwood number, which is given by Eq. (3.66).

$$Sh_g = Nu_g Le_g^{1/3} \quad (3.66)$$

Heat is removed from the 0D, “black box” gas due to wall condensation via Eq. (3.67).

$$\dot{Q}_{PC,g} = \sum_{j=1}^{N_{sp}} \dot{n}_{j,PC,g} h_{j,g} \quad (3.67)$$

Currently, dispersed fuel condensation is not modeled within the gap. This neglect is due to numerical challenges associated with a strong coupling between droplet phase change species and energy rates and bulk velocities from the RC and to the crevice. Ongoing work may be conducted to resolve these challenges, and investigate dispersed condensation in the gap.

Piston Crevice

Governing Equations

As with the piston gap region, the crevice zone of the MP-MZM is also modeled as a transient 0D “black box” style control volume, where the complex fluid dynamics inside the zone utilizing reduced-order modeling methods. Fluid dynamically, two distinct regions exist in the piston crevice. The first is the high velocity gas exiting the piston gap region, where this is modeled as a gas jet moving along the RCM cylinder wall. The gas jet feeds recirculative vortex structures in the main crevice volume. The advective motion created by the vortex structures enhance convective heat transfer rates from the gas to the piston crevice circumference at different rates than the entering gas jet. Convective heat transfer and fluid shear to the RCM surfaces are calculated in the 0D model using a weighting of these two effects.

As opposed to previously discussed computational zones, the multi-phase momentum equation is evaluated non-trivially by Eq. (3.68).

$$\frac{d}{dt} [n_{tot}v]_c = \sum_{j=1}^{N_{sp}} \dot{n}_{j,ex,tot} v_{ex} \left(\frac{\chi_{l,g}}{\chi_{v,g}} + 1 \right) - \frac{1}{2} (\tau_{jet} + \tau_{pist}) A_{s,c} \quad (3.68)$$

Here the volume centered crevice velocity v_c is characteristic of the recirculative vortex motion, and the gap exit velocity is used to characterize the incoming gas jet are used to evaluate the fluid shear stress on the piston circumference and cylinder wall, respectively. The specific methodology to obtain the fluid shear stresses is addressed later in this section.

The gas-phase species and energy equations are shown by Eqs. (3.69) and

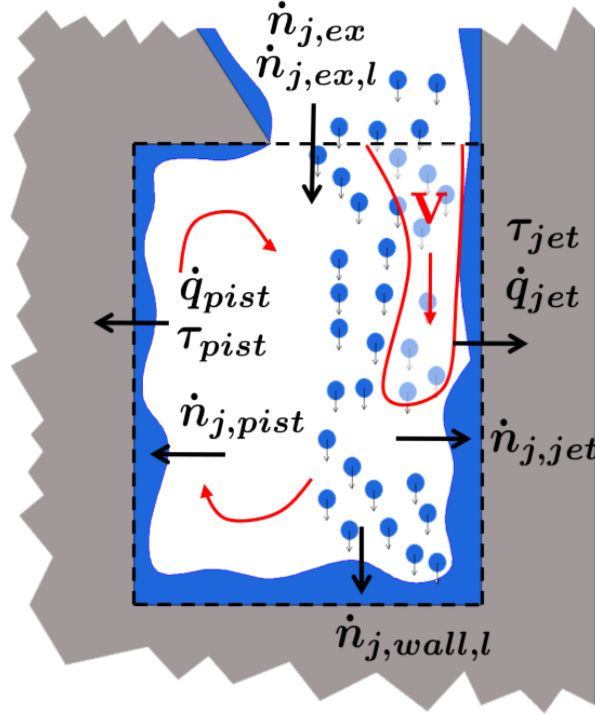


Figure 3.4: A schematic of the multi-phase flow through the piston crevice.

(3.70), and the rates of energy and species transfer are illustrated by Figure 3.4.

$$\frac{d}{dt}[n]_{j,c} = \dot{n}_{j,ex} + \dot{n}_{j,PC,c} \quad (3.69)$$

$$\sum_{j=1}^{N_{sp}} \frac{d}{dt}[nu]_c = \sum_{j=1}^{N_{sp}} \dot{n}_{j,ex} \left(\frac{v_{ex}}{2} + h_{j,g} \right) - \dot{Q}_{conv,c} - \dot{Q}_{PC,c} \quad (3.70)$$

High velocities in the crevice are present so that convection is assumed the controlling mechanism of heat transfer.

The liquid species continuity and energy equations are given by Eqs. (3.71) and (3.72).

$$\frac{d}{dt}[n]_{j,c,l} = \left(\frac{\chi_{l,g}}{\chi_{v,g}} \right) \dot{n}_{j,ex} - \dot{n}_{j,PC,c} - \dot{n}_{j,wall,c,l} \quad (3.71)$$

$$\sum_{j=1}^{N_{sp}} \frac{d}{dt}[nu]_{j,c,l} = \left(\frac{\chi_{l,g}}{\chi_{v,g}} \right) \sum_{j=1}^{N_{sp}} \dot{n}_{j,ex} h_{j,g} + \dot{Q}_{PC,c} - \dot{Q}_{wall,c,l} \quad (3.72)$$

Here a slightly different approach is taken for the phase change effects than is observed in other regions of the model. The aerosol dynamics in the crevice region are especially complex compared to other computational MZM zone, and thus a crude model for phase change is included as a first-cut approximation. This approach can be improved as future work to diligently characterize the gas-phase and multi-phase flows in this region. For the model used here it assumed that the high velocity liquid droplets entering the crevice in the gas jet have significant inertia to impact the surface at the bottom of the crevice, falling out of gas phase suspension and coating the RCM surfaces. Once the liquid phase reaches the wall, heat is transferred to the surfaces so that thermal equilibrium is achieved instantaneously with the machine surfaces. Additionally, fuel condensation from the gas phase is assumed to occur at the RCM surfaces by convective transport.

Fluid Shear

The fluid shear on the cylinder wall due to the incoming jett, and on the piston surface due to vorticular motion, is determined using a mean friction coefficient as shown by Eqs. (3.73-3.74), respectively.

$$\tau_{jet} = \frac{1}{2} C_{f,jet} \rho_g v_{ex}^2 \quad (3.73)$$

$$\tau_{pist} = \frac{1}{2} C_{f,pist} \rho_c v_c^2 \quad (3.74)$$

A friction coefficient correlation for a turbulent jet along a wall is used [269, 270] for the incoming crevice flow.

$$C_{f,jet} = 0.0042 + 0.0021 \log[\text{Re}_{ex}] \quad (3.75)$$

A Reynolds analogy of Eq. (3.63) for flow through an annular geometry is applied to the recirculative flow inside the crevice volume.

$$C_{f,pist} = \frac{24}{\text{Re}_c} \left[1 + \frac{0.008(\zeta_c/l_c)\text{Re}_c}{1 + 0.025[(\zeta_c/l_c)\text{Re}_c]^{2/3}} \right] \quad (3.76)$$

As with the gap volume, it is assumed that the suspended liquid phase does not influence the gas-phase fluid behavior so that using an established correlation for gas-phase flow is valid.

Convective Heat Transfer

Newton's law of cooling is used to prescribe the convective heat transfer rates within the crevice, where this is given by Eq. (3.77),

$$\dot{Q}_{conv,c} = h_{conv,c} A_{s,c} (T_c - T_{wall}) \quad (3.77)$$

As noted above an effective convection coefficient is utilized in this formulation, where the effects of the incoming jet and vorticular flow inside the crevice are equally weighted. This is shown by Eq. (3.78).

$$h_{conv,c} = \frac{1}{2} \left[\frac{C_{f,jet} \text{Re}_{ex}}{2\zeta_{ex}} + \frac{\text{Nu}_c}{\zeta_c} \right] k_c \quad (3.78)$$

A Reynolds analogy employing Eq. (3.75) is used to characterize the effects of the convective jet heat transfer to the cylinder wall. The heat transfer due to the recirculative flows are calculated by employing the same Nusselt correlation for turbulent, annular flow that is utilized by the gap. This is given by Eq. (3.79)

below.

$$\text{Nu}_c = 7.54 + \frac{0.028(\zeta_c/l_c)\text{Pr}_c\text{Re}_c}{1 + 0.011[(\zeta_c/l_c)\text{Pr}_c\text{Re}_c]^{2/3}} \quad (3.79)$$

Phase Change

As in the gap, the gas-phase crevice fuel is assumed to condense on the crevice surfaces as high convective velocities transport gas-phase fuel to the cool walls. The liquid film on the cylinder walls and piston circumference is assumed to be in thermodynamic (i.e. phase) equilibrium at the wall temperature.

For this approach, convective species transfer rates from the bulk gas to the walls are calculated by Eq. (3.80) in an analogous fashion to convective heat transfer rates; by use of a mean mass transfer coefficient.

$$\dot{n}_{j,PC,c} = h_{m,c}A_{s,c}(\rho_{j,c} - \rho_{j,wall}) \quad (3.80)$$

The average mass transfer coefficient is evaluated from the Sherwood number, i.e. Eq. (3.81).

$$h_{m,c} = \frac{\text{Sh}_c \mathcal{D}_j}{\zeta_c} \quad (3.81)$$

A mass analogy is again used to calculate the Sherwood number in the crevice, given by Eq. (3.82).

$$\text{Sh}_c = \text{Nu}_c \text{Le}_c^{1/3} \quad (3.82)$$

Heat is removed from the 0D, “black box” crevice gas due to wall

condensation via Eq. (3.83).

$$\dot{Q}_{PC,c} = \sum_{j=1}^{N_{sp}} \dot{n}_{j,PC,c} h_{j,c} \quad (3.83)$$

Future work may be conducted to relax the high Stokes number complete droplet impingement assumption, and relsolve some of the aerosol dynamics in the crevice.

The equations presented in this chapter now represent the complete aRCM MZM. Validation of this new model is achieved in the following chapter where comparisons are made against high-level CFD simulations. An assessment of the reaction chamber stratification present during aerosol RCM experiments is also provided over a range of conditions.

Chapter 4

RCM Aerosol Multizone Model Validation and Results

Validation Approach

The new MP-MZM model is validated here against detailed, non-reacting, single-fuel CFD simulations, where the focus is on droplet vaporization as well as the in-cylinder gas-phase mass, momentum and energy transport. For the phase-change sub-model the droplet surface area and surface temperature histories are of interest, as this information is used as a metric to investigate how well the coupled mass and energy equations are approximated. The phase-change sub-model utilized by the MP-MZM like many other dispersed, multi-phase software assumes a quasi-steady gas phase, and a zero-gradient temperature model for the liquid phase. These approximations may become invalid under high pressure, gas-phase or large initial droplet diameter conditions [267]. Under these conditions, mass and energy storage in the gas phase as well as temperature gradients within the droplet may develop. These will be referred to as “transient effects” here.

First the droplet formulation utilized by the MP-MZM is validated against a fully transient droplet vaporization model developed by Zhu and Aggarwall [271] for a single stagnant $50\ \mu\text{m}$ droplet at pressures up to 70 bar. Even though the droplets in these validation simulations are larger than those expected to be used in an aRCM, the simulation results are useful for ensuring the MP-MZM model is valid over a wide range of conditions.

Modeling of the two phase physics in an aRCM has two main functions. First, the rate of evaporative cooling or condensive heating of the gas phase is

needed in order to accurately prescribe the gas-phase temperature where chemistry occurs. Second, phase-change modeling allows an adequate prediction of the gas-phase equivalence ratio within the reaction chamber, where chemistry is modeled to occur. Stagnant, single droplet simulations are certainly not sufficient to validate that these are correctly predicted as the gas-phase undergoes compression during evaporation and far-field fuel concentrations for real fuel loadings (i.e. $\phi=1-3$) affect evaporation transport. For this the aRCM MZM droplet model is compared to the detailed droplet wet compression simulations of Goldsborough et al. [116] over a range of global equivalence ratios and initial droplet sizes.

Finally, the aRCM MZM is validated against the original RCM MZM developed by Goldsborough et al. [36] as well as the laminar flow Fluent simulations from the same study. This is to ensure that the reformulated MZM with detailed species tracking, updated energy calculation scheme, fully transient gap and pressure equilibrated crevice is still able to adequately predict rates of heat transfer to the reaction chamber surfaces as well as the crevice dynamics.

This chapter ends with the results of simulations from the new aRCM MZM model. This study investigates the thermal and compositional stratification that occurs in the RCM reaction chamber for non-reacting, single-component fuels at varied initial droplet diameters and global equivalence ratios. Future studies are planned to investigate the effects of preferential boiling and chemical heat release as well. In addition to reaction chamber stratification, adiabatic core pressure traces are simulated, which could be used to validate experimental setups as this data is easily measured. Temperature history for each zone and adiabatic core gas-phase equivalence ratio plots are also presented, where these data could be used to assign a thermodynamic state to reacting mixtures for comparison of kinetic mechanisms with experimental data.

Droplet Evaporation Model Validation

Detailed Validation Model

Detailed droplet vaporization simulations were conducted using a spherically-symmetric, fully transient model developed by Zhu and Aggarwal [271] that was further expanded by Goldsborough et al. [36, 117]. A brief description of this model is presented here, while more details can be found in [36].

The vapor and liquid phase are modeled as symmetric spheres, where transient mass, species, momentum and energy conservation along with an EOS are applied to the liquid and vapor phase. As such thermal and compositional variations are taken into account for both the vapor and liquid phases. A boundary condition of phase equilibrium is applied at the droplet surface, and real gas effects are taken into account utilizing the Peng-Robinson EOS. Spatial pressure variations are allowed across the vapor phase, however convective motion is suppressed (i.e. $Re=0$). For the conditions explored here no pressure gradients were observed. Volumetric compression of the vapor phase is used to simulate wet compression. Global stoichiometrics are prescribed by volumetrically adjusting the initial gas domain size (i.e. higher equivalence ratios are simulated by a closer far-field boundary which corresponds to denser droplet populations). An arbitrary Lagrangian-Eulerian numerical scheme is used to directly solve the governing equations, with a dynamically adaptive mesh. Thermo-physical and transport properties are evaluated locally at each grid point and updated at each time step.

Single Stagnant Droplet Comparison

The performance of the MP-MZM droplet model is compared against the detailed droplet simulations for a single, stagnant n-heptane droplet with an initial diameter of $50\text{ }\mu\text{m}$ at pressures of 1, 10, 30 and 70 bar. Initially the gas phase is pure N_2 and the liquid is pure n-dodecane. The liquid temperature is initially set to 300 K and the vapor temperature is initialized at 500 K. During the simulation, phase change proceeds as heat is conducted from the gas phase to the cooler droplet. The far-field conditions are held constant throughout the droplet lifetime, so that effects of far-field evaporative cooling and fuel saturation are not present in these simulations. The results of the two sets of simulations are displayed in Figures 4.1 and 4.2, where the droplet surface area and surface temperature histories are shown, respectively. An overall fair agreement is observed. For the 1 bar case excellent agreement in the droplet evaporation rate and surface temperature is encouraging though, as this establishes confidence in the validity of the MP-MZM droplet model, coding and solution scheme to reasonably estimate the effects of phase change for dispersed droplets.

In Figure 4.1, two distinct regions of droplet vaporization can be seen, at the start of vaporization where droplet size increases which is followed by typical d^2 (i.e. linear) behavior. Evident here is that the MP-MZM droplet model consistently produces a higher initial droplet growth in addition to accelerated and delayed vaporization times at high and low pressures, respectively. This phenomena is attributed to an overprediction of the initial rise rate of droplet temperature by the MP-MZM, which causes a decrease in density and an increase in liquid volume. Another source of the discrepancies is that in the detailed simulations a portion of the liquid mass is denser near the droplet core than at the surface due to thermal stratification, and the reduced-order model does not resolve the liquid phase thermal stratification. The MP-MZM also calculates accelerated evaporation rates in the d^2 region. This is inferred by a

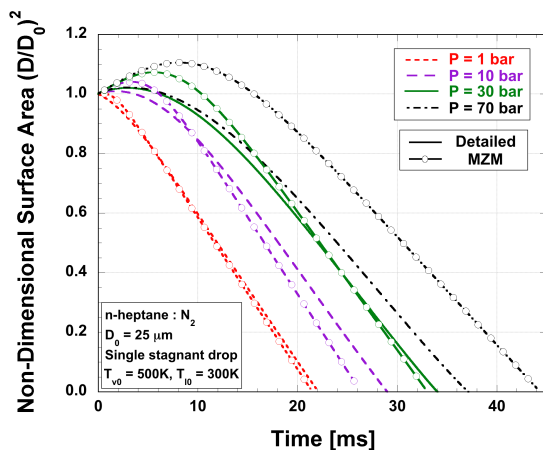


Figure 4.1: Comparison of an n-heptane droplet surface area histories for the current droplet evaporation model and the detailed model developed by Zhu and Aggarwal [271], for a single stagnant droplet over a range of pressures.

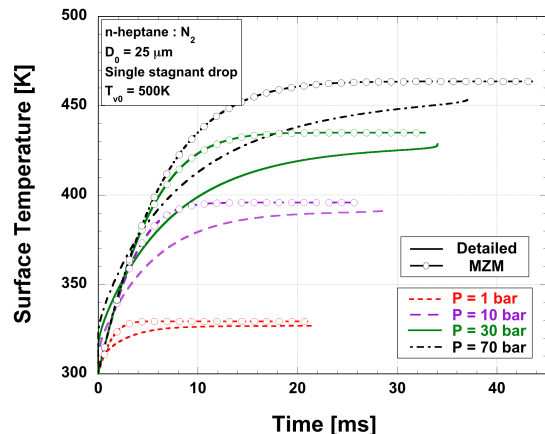


Figure 4.2: Comparison of droplet surface temperature histories for the current droplet evaporation model and the detailed model developed by Zhu and Aggarwal [271], for a stagnant droplet over a range of pressures.

steeper slope in the surface area decay for all but the high pressure case. These different rates are due to an overprediction in equilibrium surface temperatures by the MP-MZM which creates a greater driver for fuel vaporization. This is not observed in the 70 bar case because the model for gas phase diffusion coefficient is not accurate at high pressures in the reduced order model and this slows the rate at which fuel is diffused away from the droplet. An improved diffusion coefficient model could be implemented as future work to improve the fidelity of the MP-MZM. Although RCMs typically do not operate at such high compressed pressures, future investigations may in order to collect data relevant to advanced combustion engines.

The droplet surface temperatures are controlled by competing effects of conduction from the gas phase to the droplet surface, vaporization and sensible enthalpy of mass leaving the liquid phase, and liquid phase conduction from the droplet surface to the cooler center. During the droplet lifetime these effects come to an equilibrium, and eventually a constant surface temperature is realized. The detailed simulations capture all of the droplet transport

mechanisms, while the zero-gradient liquid model utilized by the MP-MZM cannot account for liquid phase conduction. After the initial heating period, internal thermal gradients are minimized as surface temperature reaches a constant value. This suggests that internal conduction has a small influence on equilibrium temperature. Since the same model for vaporization enthalpy is used by both sets of simulations, and droplet evaporation rates are similar as the droplet begins to exhibit d^2 behavior, suggests that energy transport due to vaporization has only a small influence on equilibrium temperature differences. However, enthalpy transfer has a larger effect during the droplet growth period, during which larger discrepancies in evaporation rates exist. Transient thermal effects are seen to become important in the gas phase conduction term as higher pressures are reached, and the quasi-steady gas phase approximation becomes invalid. The quasi-steady approximation becomes less accurate with increased pressures due to a decrease in gas thermal and species diffusivities where energy and mass are stored across the domain faster than can be diffused to and from the droplet, respectively.

The effect of internal droplet temperature gradients can be inferred as the cause of discrepancies between the models during the droplet initial heating/growth period. The rapid surface temperature increase occurs for the 1 bar case where gas thermal diffusivity is relatively high and evaporative mass flows agree. The disagreement in equilibrium temperature is harder to isolate, and is most likely due to a small contribution from all three heating effects. The discrepancy appears to become more severe at higher temperatures indicating that transient gas phase effects may be the most prominent source of disagreement. The discrepancies seen between the MP-MZM and the detailed model are considered acceptable for this study.

Wet Compression Comparison

The performance of the phase change sub-models is also assessed under wet compression conditions by comparing simulation results to the transient model for n-dodecane droplets of 2, 3, 8 and 14 μm diameters, at global equivalence ratios of 0, 0.5, 1 and 2. For both the detailed and reduced order models, wet compression is simulated by gas-phase mesh compression based on a piston trajectory that is characteristic of RCMs and is identical for both models. In addition to the quasi-steady gas phase and the internal droplet zero-gradient approximations utilized by the MP-MZM, another modeling difference exists for real fuel loading (i.e. $\phi \neq 1$) conditions. In the MP-MZM global equivalence ratios are set by adjusting the number of droplets in the reaction chamber, where in the transient model equivalence ratios are prescribed by adjusting the size of the gas-phase domain to emulate a more highly populated aerosol. This is not a discrepancy in and of itself, but a small discrepancy arises when specifying the far-field boundary condition. In the MP-MZM, the far-field boundary condition is taken as the average cell condition, which is not truly correct, but the error is generally small.

For this comparison the initial temperature of the gas and liquid phases are initially set to 350 K, where this temperature corresponds to a pre-heated RCM. Initially the gas phase consists air (i.e. $\text{N}_2 + 3.76\text{O}_2$), and the liquid phase is composed of pure n-dodecane; no fuel initially exists in the gas phase for these calculations. A typical RCM compression ratio of 13.4 and compression time of 15.3 ms are used as in [116]. The results are presented in Figures 4.3 - 4.11, and as can be seen generally a fair agreement is achieved. Figures 4.3 - 4.6 show the results for varied initial droplet diameters and Figures 4.7 - 4.11 show the results for varied global equivalence ratios. The results for varied droplet diameters will be discussed first.

Discrepancies in the simulations are consistent with the previous comparisons,

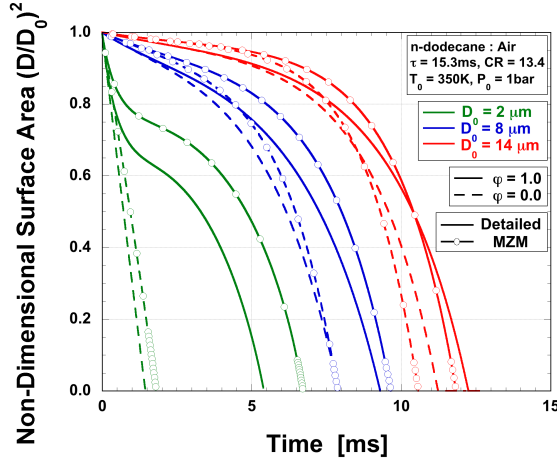


Figure 4.3: Comparison of n-dodecane droplet surface area histories undergoing wet compression for the current vaporization model and that of Goldsbrough et al. [36] at two global equivalence ratios and a range of initial droplet diameters.

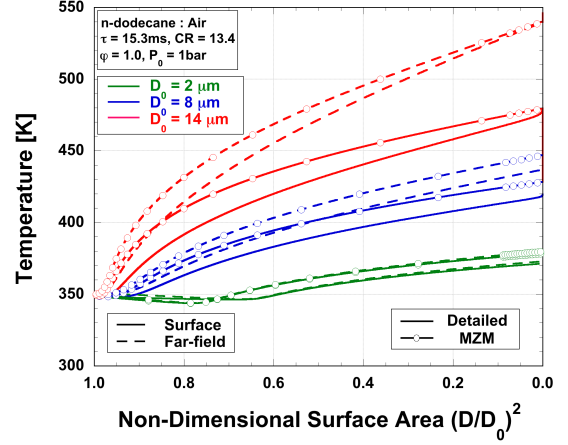


Figure 4.4: Comparison of n-dodecane droplet surface and far-field temperature histories undergoing wet compression for the current vaporization model and that of Goldsbrough et al. [36] at a global equivalence ratio of $\phi=1$ and a range of initial droplet diameters.

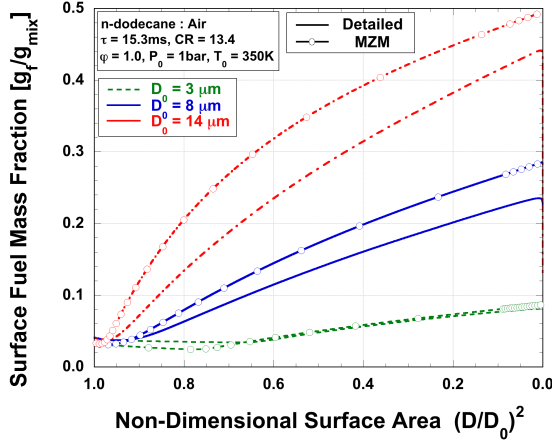


Figure 4.5: Comparison of n-dodecane droplet surface fuel fraction as a function of non-dimensional surface area, for droplets undergoing wet compression for the current vaporization model and that of Goldsbrough et al. [36] at a global equivalence ratio of $\phi=1$ and a range of initial droplet diameters.

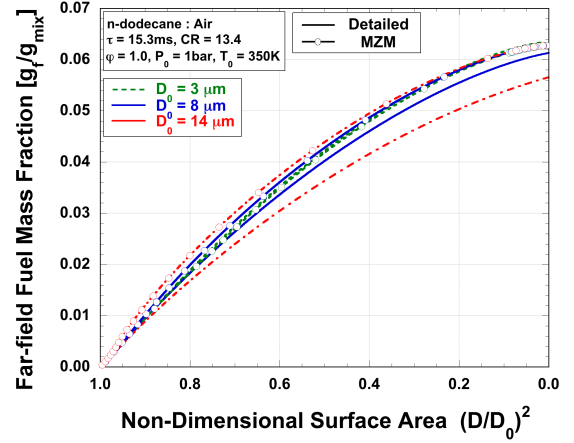


Figure 4.6: Comparison of n-dodecane droplet far-field fuel fraction as a function of non-dimensional surface area, for droplets undergoing wet compression for the current vaporization model and that of Goldsbrough et al. [36] at a global equivalence ratio of $\phi=1$ and a range of initial droplet diameters.

droplet heating rates are again overpredicted for varied droplet diameters undergoing wet compression. This results in similar behavior as seen earlier,

where the initial droplet heating delays vaporization due to volumetric growth, while vaporization rates are overpredicted once a steady temperature is reached. This influence is further observed in Figure 4.5, where fuel mass fractions are overpredicted due to elevated surface temperatures that leads to higher vaporization potentials. The high fuel fraction increases the diffusive mass flux to the far-field, while droplet geometry also has an effect on the mass diffusion process. Initially large droplet diameters control the mass diffusion process, where later in the vaporization these effects become small. In all cases far-field compositions closely match the detailed simulations where these eventually converge to the same mass fraction which corresponds to a stoichiometric equivalence ratio. This is encouraging because correct far field mass fraction predictions are critical to the MP-MZM model. Discrepancies in the far-field composition for the larger droplets is due to large compositional stratification in the gas phase caused by mass storage throughout the domain. The quasi-steady gas-phase model has limited capabilities to capture these trends.

Far-field gas temperatures are also higher for the MP-MZM model at any instantaneous droplet diameter, this is due to initially delayed droplet vaporization. Inspection of both Figure 4.3 and 4.4 simultaneously at times where surface areas match supports this. At these times far-field temperatures closely match, suggesting that delayed droplet vaporization effects dominate the discrepancies, and that evaporative cooling rates are correctly calculated.

Simulation results are presented in Figures 4.7 - 4.11 where varied fuel loadings are used with an initial droplet diameter of $3\ \mu\text{m}$. Comparisons, between the two models demonstrate generally good agreement, although higher temperatures are again predicted by the MP-MZM along with delayed droplet vaporization times. The very good agreement observed in Figures 4.10 and 4.11 for the surface and far-field fuel mass fraction provide confidence that the mass transport is properly simulated for these conditions. The poor agreement in surface and far-field temperatures can be attributed to a combination of the

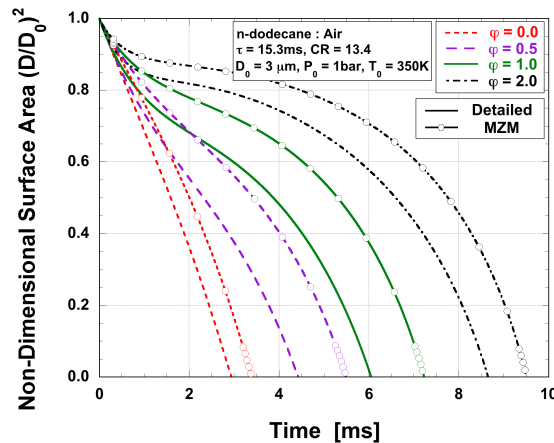


Figure 4.7: Comparison of n-dodecane droplet surface area histories undergoing wet compression for the current vaporization model and that of Goldsborough et al. [36] at varied global equivalence ratios.

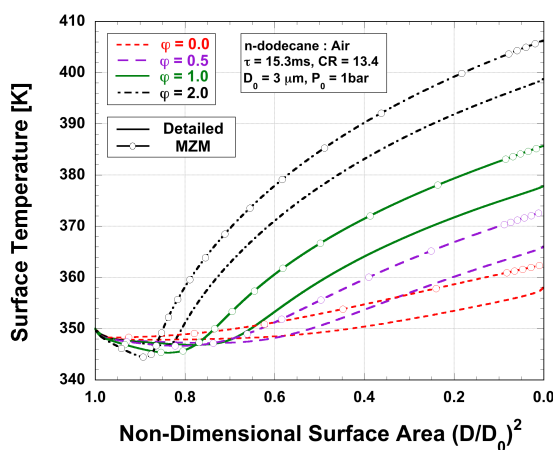


Figure 4.8: Comparison of n-dodecane droplet surface temperature as a function of non-dimensional surface area, for droplets undergoing wet compression for the current vaporization model and that of Goldsborough et al. [36] at varied global equivalence ratios.

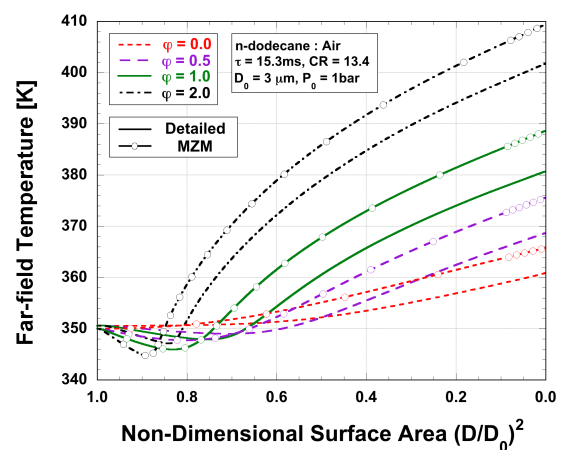


Figure 4.9: Comparison of n-dodecane droplet far-field temperature as a function of non-dimensional surface area, for droplets undergoing wet compression for the current vaporization model and that of Goldsborough et al. [36] at varied global equivalence ratios.

mechanisms discussed above. The higher temperatures once again result in overestimates of the initial growth period, where this leads to delayed vaporization times. However, it can be seen that discrepancies in the surface area slope (e.g. vaporization rate) are minimal after the initial droplet heating period.

This may be caused at the high fuel loadings where far-field saturation effects have more impact on mass diffusion than the droplet surface vapor pressure.

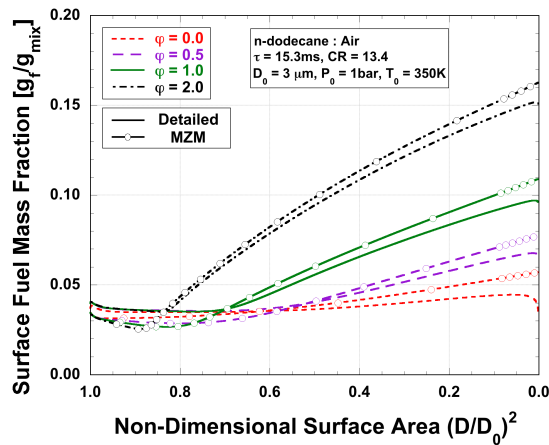


Figure 4.10: Comparison of n-dodecane droplet surface fuel mass fraction as a function of non-dimensional surface area, for droplets undergoing wet compression for the current vaporization model and that of Goldsborough et al. [36] at varied global equivalence ratios.

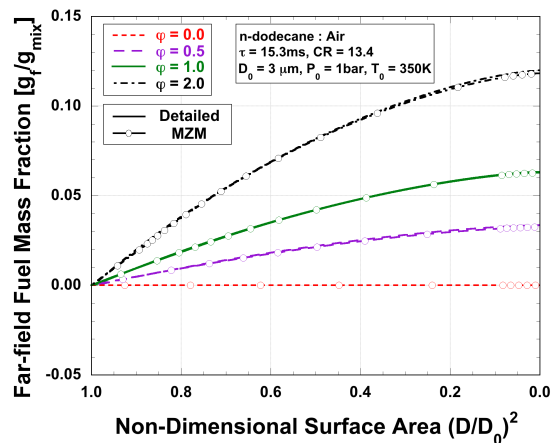


Figure 4.11: Comparison of n-dodecane droplet far-field mass fraction as a function of non-dimensional surface area, for droplets undergoing wet compression for the current vaporization model and that of Goldsborough et al. [36] at varied global equivalence ratios.

Gas-phase Transport Validation

Validation Methodology

The ability of the MP-MZM to accurately predict the gas-phase physics of RCM experiments is assessed in this section by comparing simulation results to results of the original MZM. A discussion of the previously validated MZM was presented in Chapter 2, while differences between the modeling approaches have

been outlined in Chapter 3. A further review of the validation model will not be presented here.

Table 4.1: Conditions of each validation case for the RCM gas-phase processes.

Case	T_0 [K]	P_0 [bar]	Molar Composition [N ₂ /Ar]
1	300	0.426	1.0/0.0
2	300	0.866	1.0/0.0
3	300	1.430	1.0/0.0
4	300	0.381	0.6/0.4
5	300	0.736	0.6/0.4

For this validation step non-reactive conditions, are used where results are compared over a range of initial pressures and two argon + nitrogen diluent compositions. A summary of these test cases is presented in Table 4.1. Cases 1 and 4 as well as 2 and 5 are utilized as they yield nearly equivalent compressed pressures for both neat N₂, as well as the 60% N₂ 40% Ar blends. The addition of argon in the diluent has the effect of achieving higher compressed temperatures than pure nitrogen, due to it's relatively small specific heat. However the lower mixture specific heat of the argon blends and lower density results in an increased gas thermal diffusivity, where heat diffusion rates through the gas to the reaction chamber walls are greater compared to a pure nitrogen test gas. Thus the validation conditions are selected in order to ensure that the new model is valid for a range of conditions that exhibit varied thermodynamic and transport properties that are relevant to RCM experiments.

Computations are performed utilizing a typical RCM geometry and piston compression time. A schematic of the relevant dimensions is shown in Figure 4.12 where the corresponding values used in the calculations are given in Table 4.2. In these simulations, the piston motion is prescribed in a manner similar to that of an operating engine where the dimensions for a crank radius and connecting rod length are specified, and the piston motion is actuated at BDC and comes to

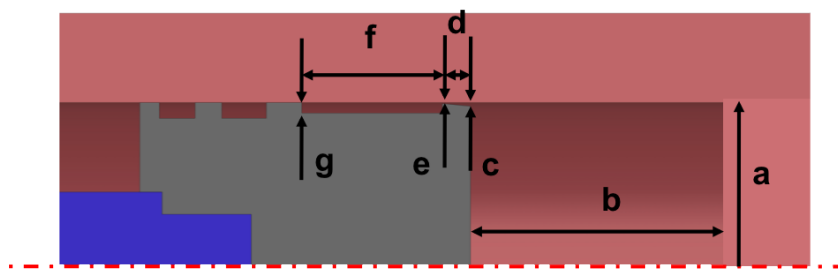


Figure 4.12: Schematic of key RCM dimensions at maximum compression, values used in this study as well as for gas phase model validation are available in table 4.2.

Table 4.2: RCM dimensions used in this study, as well as gas phase model validation. Lettered dimensions correspond to Figure 4.12.

Dimension	Value
a	25.0 mm
b	14.0 mm
c	0.50 mm
d	4.00 mm
e	0.15 mm
f	20.0 mm
g	1.50 mm
stroke	216 mm
compression time	30 ms

rest at TDC. This is done in order to be consistent with the CFD simulations that were used to validate the original MZM. While this piston trajectory is not quite representative of RCM experiments, the computed bulk pressures, temperatures and velocities are fairly similar. Discrepancies between this trajectory model and one characteristic of an operating RCM are considered negligible for this study, as the goal here is only to ensure that the new MZM formulation agrees with previously obtained results.

The reaction chamber mesh is constructed using a slightly different approach compared to previous MZM formulations. Previously the MZM reaction chamber mesh was initially generated using elements of equal volumes across the mesh

where higher spatial resolution is achieved near the wall of the reaction chamber. The current formulation relaxes this constraint and allows for an even higher mesh densities in the boundary layer volume. This is needed because the previous MZM simulations used a mesh cell count of 200, while the current formulation uses only 100 due to increased computational requirements. Improved spatial resolution in the thermal boundary layer is achieved in the current simulations at the expense of resolution in the core gases.

For the MP-MZM a modified approach for calculating thermochemistry is utilized where this is briefly described here with more details available in Appendix A. The single-phase MZM calculates gas-phase energy from the integration of gas-phase specific heat, where the reference states are taken to be in the gas phase. A more general approach is needed in the MP-MZM that ensures consistent reference states for two-phase physics. In the MP-MZM, thermodynamic reference states are taken in the liquid phase and the *total* gas-phase energy is used. This approach enables information about the sensible heating prior to vaporization, vaporization enthalpy at the phase change condition, as well as the sensible energy change during gas-phase heating to be carried by a gas-phase species. For these simulations it is assumed that vaporization of the nitrogen and argon occurs prior to the experiment at each species normal boiling temperature.

Validation Results

Figures 4.13 and 4.14 show the comparison of predicted pressure traces for the pure N_2 and the N_2+Ar blend, respectively. Very good agreement is observed between the MP- and previous MZM for low-pressure cases, though for the high pressure case (i.e. Case 3) there is a noticeable discrepancy. In all cases the

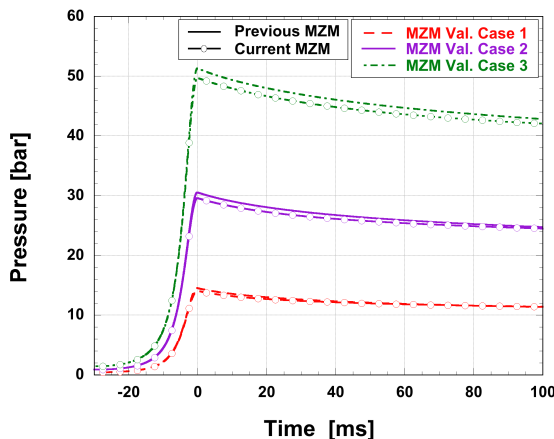


Figure 4.13: A comparison of pure N_2 simulated pressure traces for the current MZM and a previous multi-zone formulation [36].

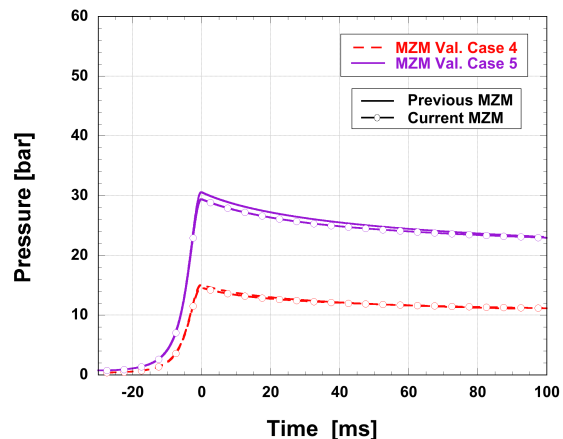


Figure 4.14: A comparison of a $0.6N_2/0.4Ar$ blend simulated pressure traces for the current MZM and a previous multi-zone formulation [36].

MP-MZM formulation underpredicts the compressed pressure, where this becomes more apparent with increasing pressure. The underprediction of RC pressure is attributed to an overprediction of the rate at which gas is transferred to the piston gap and crevice region by the new formulation which assumes pressure equilibrium. This can be seen in Figures 4.15 - 4.17, where the predicted gap exit and crevice velocities for Cases 2 and 5, as well as the mole fractions of gas in the crevice are plotted, respectively. Cases 2 and 5 are highlighted here while Cases 1, 3 and 4 show similar trends.

Here it can be seen that the MP-MZM predicts elevated velocities compared to the SP-MZM. As stated this is due to the assumption of the new model that the three computational zone are in pressure equilibrium, opposed to the previous formulation which solves the momentum equation, where fluid shear in the piston gap region is taken into account. The greater gas velocity to the piston crevice during compression is thought to be the main cause of underpredicted compressed pressures by the new model. Pressure is decreased as gas is transferred to the piston crevice at overpredicted velocities, which thereby results in higher rates of convective heat transfer to the RCM surfaces and thus a

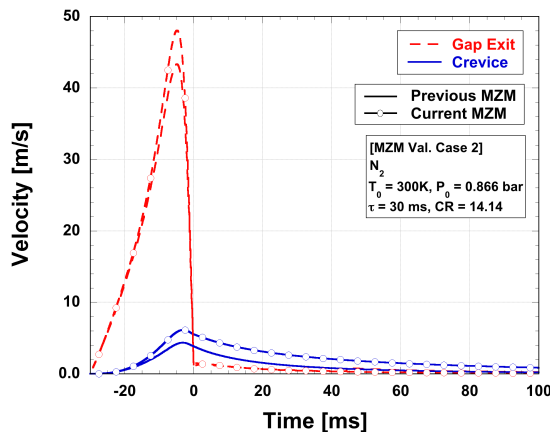


Figure 4.15: A comparison of case 2 simulated gas velocities in the piston gap and crevice for the current MZM and a previous multi-zone formulation [36].

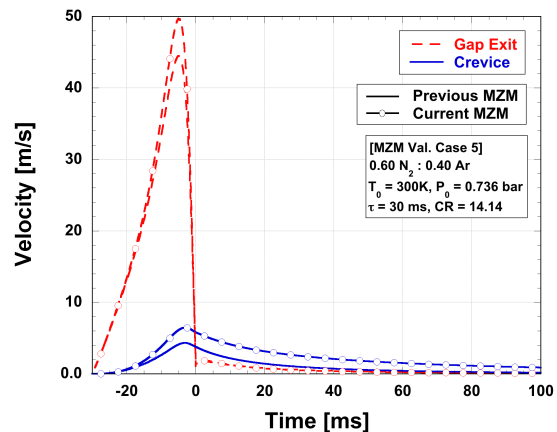


Figure 4.16: A comparison of case 5 simulated gas velocities in the piston gap and crevice for the current MZM and a previous multi-zone formulation [36].

lower zone-equilibrated pressure. This conclusion is further supported by inspection of the average crevice velocities in Figures 4.15 and 4.16 which are indeed increased by neglecting shear losses in the gap. Also, Figure 4.17 shows that the amount of gas in the crevice is overpredicted, where this gas cools quickly due to high convective velocities lowering the RCM pressure.

Figures 4.18 and 4.19 present the gas temperatures computed by both model formulations for Cases 2 and 5, respectively. As with the velocities these plots are presented as representative cases, where the other investigated conditions show similar trends. First, it is noted that good agreement is achieved in the adiabatic core and average reaction chamber temperatures. Differences between the reaction chamber temperatures predicted by the two MZMs are attributed to an over prediction of the amount of gas in the crevice at maximum compression, as well as differences in mesh geometry and resolution.

Significant disagreement is observed in the gap and crevice temperatures, however this disagreement appears to have only a small influence on the reaction chamber. A lower temperature is observed in both the gap and crevice regions for the MP-MZM. This is an effect of neglecting fluid shear in the gap, which

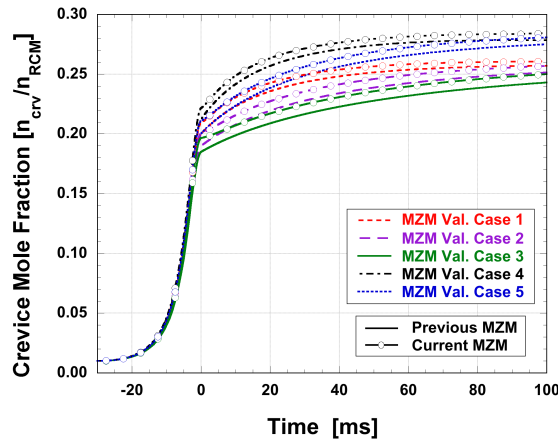


Figure 4.17:

A comparison of simulated crevice mole fraction for the current MZM and a previous multi-zone formulation [36].

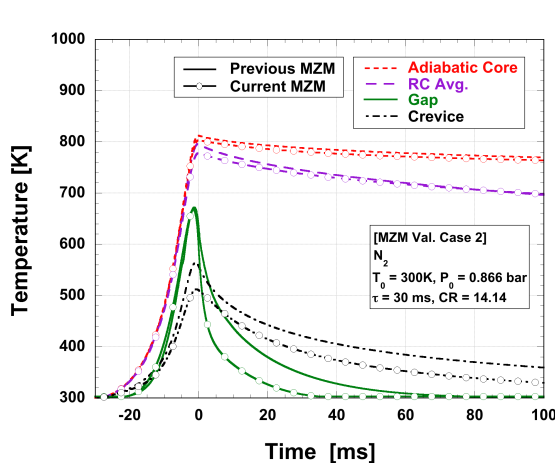


Figure 4.18: A comparison of case 2 simulated gas temperatures for the current MZM and a previous multi-zone formulation [36].

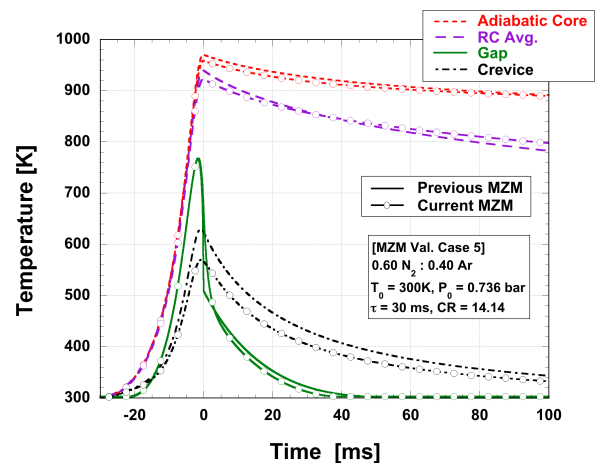


Figure 4.19: A comparison of case 5 simulated gas temperatures for the current MZM and a previous multi-zone formulation [36].

subsequently leads to overpredicted convective velocities in these regions.

Overall it can be seen that the new, MP-MZM does a fairly good job capturing the important gas-phase physics in the RCM.

Single Component Fuel Results

For the current study phase-change effects on RCM experiments are assessed by using the newly developed MP-MZM to simulate aerosol fueled experiments where n-dodecane and n-hexadecane are used as fuels; these are two commonly used petro-diesel fuel surrogates with fairly high boiling points, 216 C and 286 C, respectively. An initial droplet diameter of $8\text{ }\mu\text{m}$ is used in all simulations where this is expected to be experimentally achievable [272] and sufficiently small to ensure complete vaporization before fuel decomposition and oxidation chemistry becomes important. Initially, the mixture and machine are assumed to be heated to 350 K, with the fuel loaded at atmospheric pressure. It is also assumed that the aerosol bath gas is initially saturated with fuel vapor at the pre-heat conditions, based on prior modeling of an aerosol fuel delivery system [272]. Computations are performed here using a machine geometry consistent with Table 4.2, and a motored engine piston trajectory is used, which has been described above.

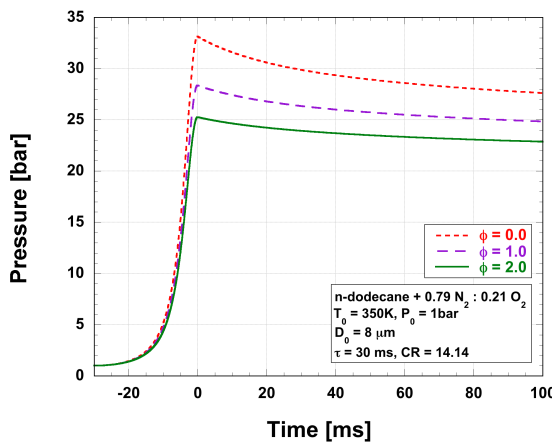


Figure 4.20: Simulated pressure traces for an n-dodecane $D_0 = 8\text{ }\mu\text{m}$ aerosol at $\phi = 0.0, 1.0$ and 2.0 initially at $P_0 = 1$ bar and $T_0 = 350$ K.

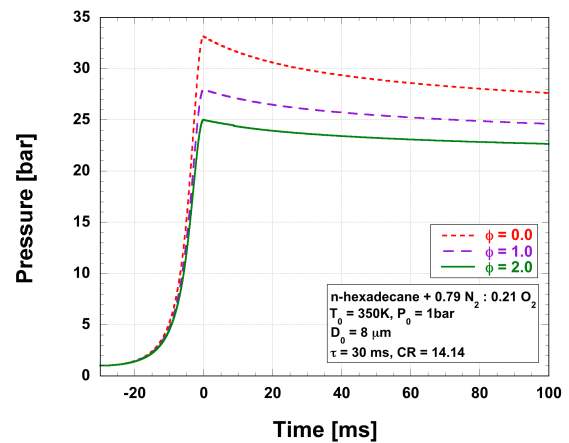


Figure 4.21: Simulated pressure traces for an n-hexadecane $D_0 = 8\text{ }\mu\text{m}$ aerosol at $\phi = 0.0, 1.0$ and 2.0 initially at $P_0 = 1$ bar and $T_0 = 350$ K.

Figures 4.20 and 4.21 show the simulated pressure traces for n-dodecane and n-hexadecane, respectively, at these equivalence ratios, $\phi=0, 1.0$ and 2.0 . Compressed pressures decrease with increasing global equivalence ratios due to evaporative cooling effects. It is interesting to note that the pressure traces for both fuels are almost identical. At their respective normal boiling temperature n-hexadecane has $\sim 30\%$ larger vaporization enthalpy than n-dodecane, where this suggests that evaporative cooling effects should have a greater affect on RC pressure for the n-hexadecane cases. Careful inspection of Figures 4.20 and 4.21 confirms that this is the case for the simulations presented here, and also that a seemingly large perturbation of vaporization enthalpy only has a small effect on RC pressure. It is suspected from this study, which will be supported further, that the fuel is present in such minute quantities, even at high equivalence ratio conditions, that fuel effects on bulk mixture thermophysical and transport properties are very small.

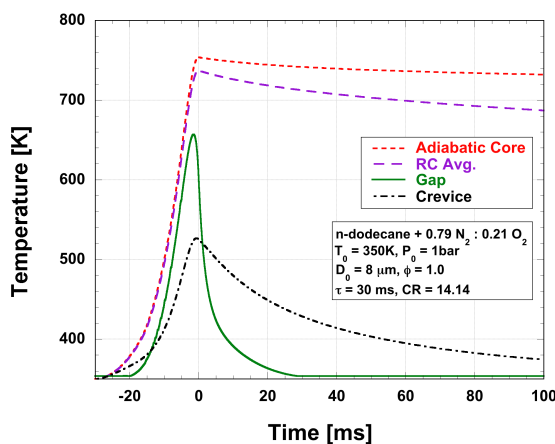


Figure 4.22: Simulated temperatures for an n-dodecane $D_0 = 8 \mu\text{m}$ aerosol at $\phi = 1.0$ initially at $P_0 = 1$ bar and $T_0 = 350$ K.

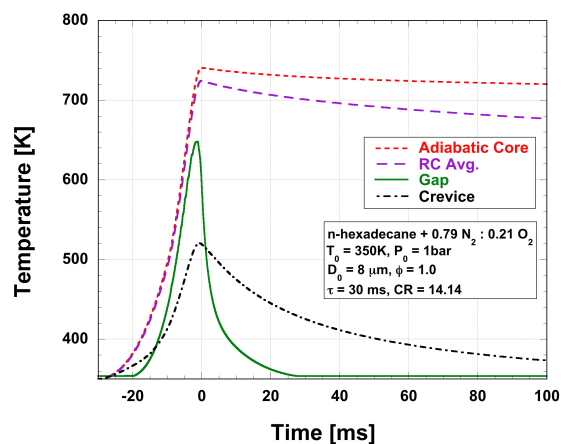


Figure 4.23: Simulated temperatures for an n-hexadecane $D_0 = 8 \mu\text{m}$ aerosol at $\phi = 1.0$ initially at $P_0 = 1$ bar and $T_0 = 350$ K.

The temperatures in each computational zone as well as the adiabatic core for both fuels at stoichiometric fuel loading are shown in Figures 4.22 and 4.23.

As can be seen the effects of the vaporization enthalpy are more prominent when evaluating these results, where n-hexadecane has slightly lower compressed RC, gap and crevice temperatures due to enhanced evaporative cooling during vaporization. The high specific heat of the n-hexadecane, which reduces the mixture thermal diffusivity relative to n-dodecane has a small effect on the rate of decay of the average RC temperature. This is again thought to be due to the small amounts of fuel present in the reaction chamber.

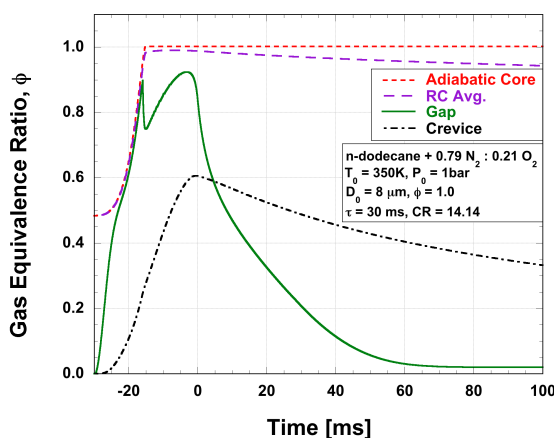


Figure 4.24: Simulated gas-phase equivalence ratios for an n-dodecane $D_0 = 8 \mu\text{m}$ aerosol at $\phi = 1.0$ initially at $P_0 = 1$ bar and $T_0 = 350$ K.

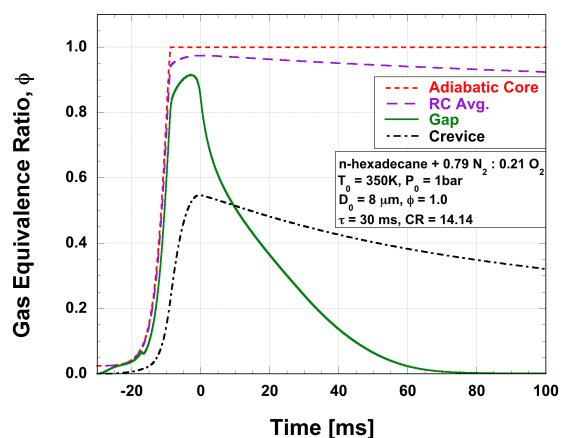


Figure 4.25: Simulated gas-phase equivalence ratios for an n-hexadecane $D_0 = 8 \mu\text{m}$ aerosol at $\phi = 1.0$ initially at $P_0 = 1$ bar and $T_0 = 350$ K.

Figures 4.24 and 4.25 illustrate the gas-phase equivalence ratios in each computational zone for both fuels at a stoichiometric *global* (i.e. liquid + gas) equivalence ratio. First, it is noted that the decay in piston gap and crevice gas equivalence ratio is completely due to convective mass transfer to the RCM surfaces and condensation. The sharp falloff in the gap equivalence ratio during compression is due to a rapid increase in convective velocity in the gap, which drives fuel transport to the wall.

As is evident here, the adiabatic core, gas-phase fuel equivalence ratio, after complete vaporization, remains unaltered for all of the conditions investigated in

this study. This is due to the fact that the species diffusion process from the core to the RC walls, where most fuel is in the condensed phase, is slow compared to a 100 ms delay period (ignition time). This is encouraging, and builds confidence that aerosol fuel loaded RCM experiments will be able to produce high fidelity chemical kinetic data. Contrary to the previous results a large deviation in the average RC gas equivalence ratio from the adiabatic core is observed for the n-hexadecane cases compared to the n-dodecane cases, where this is due to the lower vapor pressure of n-hexadecane, so that more fuel condenses in the boundary layer.

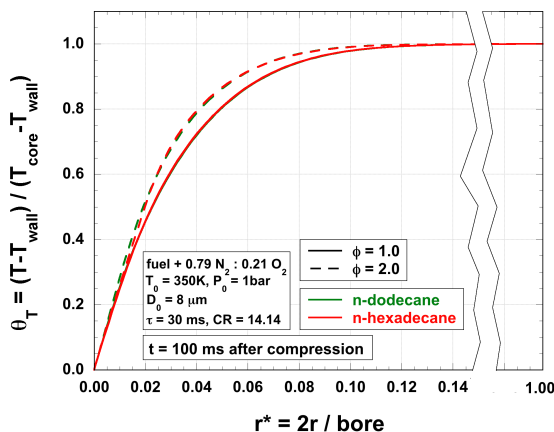


Figure 4.26: Simulated reaction chamber non-dimensional temperature gradients for a $D_0 = 8\text{ }\mu\text{m}$ aerosol at $\phi = 0.0$, 1.0 and 2.0 initially at $P_0 = 1\text{ bar}$ and $T_0 = 350\text{ K}$.

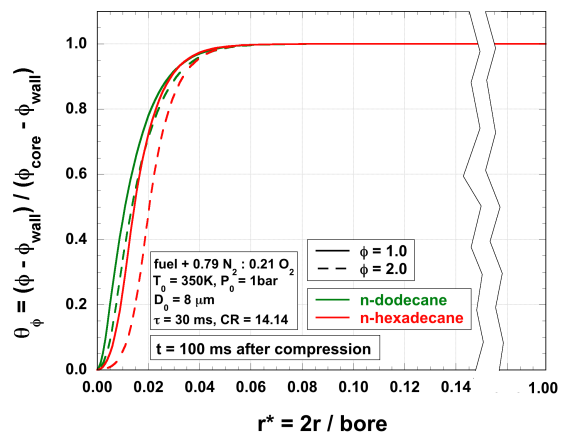


Figure 4.27: Simulated reaction chamber non-dimensional gas equivalence ratio gradients for a $D_0 = 8\text{ }\mu\text{m}$ aerosol at $\phi = 0.0$, 1.0 and 2.0 initially at $P_0 = 1\text{ bar}$ and $T_0 = 350\text{ K}$.

Figures 4.24 and 4.25 show the non-dimensional thermal and compositional boundary layers at the end of the 100 ms delay period for six cases simulated in this study. As can be seen, the thermal boundary layer is almost identical for both fuels, however the global equivalence ratio has a larger influence on the shape of the boundary layer. The sharper profile of the fuel rich simulations, compared to the stoichiometric, is due to the lowered gas mixture thermal

diffusivity by the introduction of more high specific heat fuel. The lowering of thermal diffusivity at rich conditions protracts the rate at which the thermal boundary layer is propagated into the core gases.

Fuel composition, as well as global equivalence ratio have a larger effect on the gas-phase equivalence ratio boundary layer than the thermal boundary layer. Fuel vapor pressure, binary diffusion coefficient of the fuel into the oxidizer + diluent mixture and the composition gradient across the RC are the parameters which control the curvature of the compositional boundary layer. The low-vapor pressure of the heavier fuel results in fuel condensation further into the thermal boundary layer, compared to more volatile n-dodecane. High fuel loadings have the effect of widening the compositional boundary layer, as increased gas-phase oversaturation drives a high potential for condensation in the thermal boundary layer. The fuel rich conditions also create a higher composition gradient from the core gases to the wall, which drives faster species diffusion across the reaction chamber.

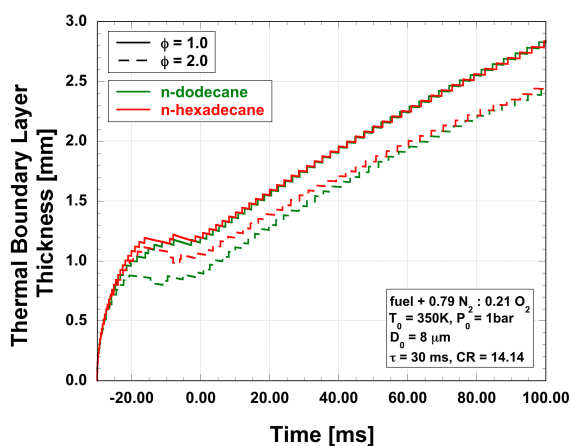


Figure 4.28: Simulated reaction chamber thermal boundary layer thickness for a $D_0 = 8 \mu\text{m}$ aerosol at $\phi = 0.0, 1.0$ and 2.0 initially at $P_0 = 1 \text{ bar}$ and $T_0 = 350 \text{ K}$.

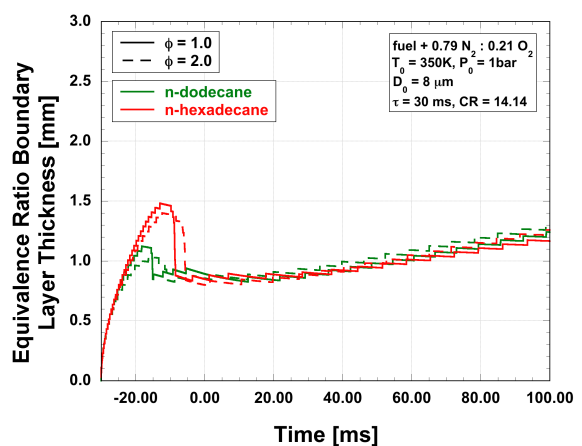


Figure 4.29: Simulated reaction chamber compositional boundary layer thickness for a $D_0 = 8 \mu\text{m}$ aerosol at $\phi = 0.0, 1.0$ and 2.0 initially at $P_0 = 1 \text{ bar}$ and $T_0 = 350 \text{ K}$.

Figures 4.28 and 4.29 present the thermal and compositional boundary layer growth in the reaction chamber. The large “steps” in the data is due to inadequate spatial resolution in the reaction chamber computational mesh (i.e. mesh coarseness). This artifact makes isolating changes in the boundary layer thickness from dynamic mesh rezoning difficult, however some trends may be inferred from these results. First, the thermal boundary layer propagates into the core gases at a faster rate than the fuel composition boundary layer for the cases investigated in this study. Also, there is little difference in the rate at which the equivalence ratio boundary layer propagates after complete vaporization is achieved for the cases investigated here. These features indicate that the species diffusion process for all of the cases is similar, and that differences in the compositional boundary layer are mainly controlled by fuel vapor pressure.

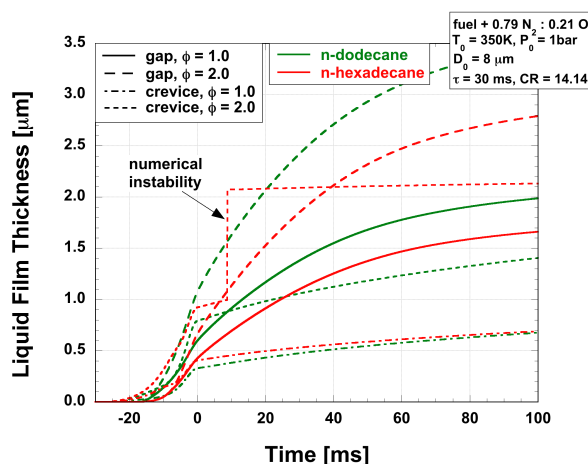


Figure 4.30: Simulated gap and crevice liquid film thickness for a $D_0 = 8 \mu\text{m}$ aerosol at $\phi = 0.0, 1.0$ and 2.0 initially at $P_0 = 1 \text{ bar}$ and $T_0 = 350 \text{ K}$.

Lastly, Figure 4.30 shows the liquid film thickness on the gap and crevice surfaces due to wall condensation and liquid droplet impingement on the surfaces. First, it should be noted that a numerical instability in the solution scheme led to an erroneous result for the fuel-rich, n-hexadecane case. This instability occurs for some fuel rich conditions and causes spikes in the gap exit

velocity, and is caused by a stiff coupling between cell pressure decrease due to rapid condensation and calculation of the velocity required to achieve pressure equilibrium throughout the zones.

The liquid thickness in the gap is completely due to convective species transport to the walls where fuel condenses. The fuel film in the crevice is due to wall condensation, as well as droplet impingement. The rapid rate of film growth in the gap compared to crevice, after the compression process is complete indicates that most of the fuel vapor condensation occurs in the gap, and this process is much slower in the crevice.

Chapter 5

Summary, Conclusions and Future Work

Summary

Rapid compression machine experiments are used to collect chemical kinetic validation targets for fuel decomposition and oxidation processes at engine relevant conditions. Conventionally, these experiments are limited to gas-phase or volatile fuels. Pre-heating the RCM and test gas has been a successful method to incorporate low-vapor pressure fuels into RCM experiments, however only for a narrow range of conditions as significant pre-test heating can cause fuel pyrolysis and degradation of machine seals. Even if pre-test fuel vaporization is achieved, fuel may condense during the experiment at the high pressure compressed conditions. Loading a test charge of a finely atomized fuel + diluent + oxidizer aerosol has been suggested to extend RCM experiments to involatile fuels, where vaporization and oxidizer mixing is achieved during the compression process. The effects of phase-change in aerosol and pre-heated fuel experiments on the well-defined RCM adiabatic core have not been investigated in previous work. The goal of this study is to assess the extent of thermal and compositional stratification within the RCM reaction chamber, to determine if an accurate comparison can be made between computationally-efficient 0D homogeneous reactor models and RCM experiments.

To facilitate this study a reduced-order, computationally-efficient multi-zone model for two-phase RCM experiments has been developed. This transient formulation separates the RCM into three computational zones; the reaction chamber, the piston gap and the piston crevice. The multi-phase model differs

from a previously developed RCM MZM, in that detailed species tracking, molecular and convective species transport and phase-change physics are taken into account. In addition to offering insight into the physics of these novel RCM experiments, the model is computationally tractable to provide energy and composition changes in the test charge to HRMs where detailed chemistry can be simulated.

The new model has been validated here against detailed simulations for droplet evaporation as well as the single-phase formulation of the MZM, and exhibits good agreement. For this study, the new model is used to obtain non-reactive predictions of bulk pressures as well as temperature and composition gradients for two commonly used diesel surrogates, n-dodecane and n-hexadecane.

Conclusions

For the conditions investigated here, the equivalence ratio of the adiabatic core is predicted to be unaltered after compression by the presence of involatile fuels in the RCM test charge. This provides confidence that high fidelity chemical data can be collected from RCM experiments with involatile fuels and adequately compared to tractable HRMs simulating detailed kinetics, for the conditions investigated in this study. In general the thickness of the gas-phase compositional boundary layer is found to be smaller than the thermal boundary layer inside the RCM reaction chamber. This suggests that, for these fuels and initial conditions, the species diffusion process to the reaction chamber walls is slower than the heat diffusion process. The effects on the experimentally accessible reaction chamber pressure traces by aerosol fuel loading has been assessed, where the predicted traces varied weakly as a function of molecular structure and strongly

as a function of the extent of fuel loading. Predictions for the temperature and composition in each zone of the new MZM have been made where these results seem reasonable as they follow the correct physical trends. Confidence in the quantitative validity of the data presented here, however, should be assessed as more detailed simulation results and experimental data sets become available.

Future Work

The majority of the effort of this work has been focused on developing and validating a physics-based model as well as software to simulate the multi-phase physics of RCM experiments that utilized heavy, transportation relevant fuels. The initial results presented here represent a starting point for interesting studies that could be undertaken using the new model. For instance, the MP-MZM could be updated to investigate the effects of preferential boiling in multi-component fuels. Also, the code could be updated to investigate, in more detail, aerosol dynamics (i.e. settling, impingement, coagulation, polydispersed droplets) that occur within the RCM. The effects of chemical reaction on transport processes could also be included so that comparisons could be made with experimental data sets.

BIBLIOGRAPHY

- [1] S. Manasra and D. Brueggemann. Effect of split injection on the combustion and in-cylinder soot formation characteristics of low compression ratio neat gas-to-liquid-fueled DI diesel engine. *SAE Paper*, 2012-01-0690, 2012.
- [2] A. Adam, T. Yatsufusa, T. Gomi, N. Irie, and Y. Kidoguchi. Analysis of droplets evaporation process of diesel spray at ignition delay period using dual nano-spark shadowgraph photography method. *SAE Paper*, 2009-32-0017, 2009.
- [3] W. A. Abdelghaffar, K. Karimi, and M. R. Heikal. Fuel spray penetration in high pressure diesel engines. *SAE Paper*, 2007-01-0066, 2007.
- [4] S. Schlatter, B. Schneider, Y.M. Wright, and K. Boulouchos. Comparative study of ignition systems for lean burn gas engines in an optically accessible rapid compression machine. *SAE Paper*, 2013-24-0112, 2013.
- [5] A. Kikusato, H. Fukasawa, K. Nomura, J. Kusaka, and Y. Daisho. A study on the characteristics of natural gas combustion at high compression ratio by using a rapid compression and expansion machine. *SAE Paper*, 2012-01-1651, 2012.
- [6] M. Katsumata, K. Morikawa, and M. Tanabe. Behavior of shock wave and pressure wave of SI knocking with super rapid compression machine. *SAE Paper*, 2011-01-1875, 2011.
- [7] S.S. Kee, M. Shioji, A. Mohammadi, M. Nishi, and Y. Inoue. Knock characteristics and their control with hydrogen injection using a rapid compression/expansion machine. *SAE Paper*, 2007-01-1829, 2007.
- [8] M. Ihme. On the role of turbulence and compositional fluctuations in rapid compression machines: Autoignition of syngas mixtures. *Combust. and Flame*, 159(4):1592 – 1604, 2012.
- [9] P. Guibert, A. Keromnes, and G. Legros. Development of a turbulence controlled rapid compression machine for HCCI combustion. *SAE Paper*, 2007-01-1869, 2007.
- [10] B.W. Weber, K. Kumar, Y. Zhang, and C.J. Sung. Autoignition of n-butanol at elevated pressure and low-to-intermediate temperature. *Combust. and Flame*, 158(5):809 – 819, 2011.
- [11] M. Crochet, R. Minetti, M. Ribaucour, and G. Vanhove. A detailed experimental study of n-propylcyclohexane autoignition in lean conditions. *Combust. and Flame*, 157(11):2078 – 2085, 2010.
- [12] K. Kumar and C.J. Sung. An experimental study of the autoignition characteristics of conventional jet fuel/oxidizer mixtures: Jet – A and JP – 8. *Combust. and Flame*, 157(4):676 – 685, 2010.

- [13] S. Gersen, A.V. Mokhov, J.H. Darneveil, and H.B. Levinsky. Ignition properties of n-butane and iso-butane in a rapid compression machine. *Combust. and Flame*, 157(2):240 – 245, 2010.
- [14] R. Grana, A. Frassoldati, C. Saggese, T. Faravelli, and E. Ranzi. A wide range kinetic modeling study of pyrolysis and oxidation of methyl butanoate and methyl decanoate – Note II: Lumped kinetic model of decomposition and combustion of methyl esters up to methyl decanoate. *Combust. and Flame*, 159(7):2280 – 2294, 2012.
- [15] S.M. Sarathy, S. Vranckx, K. Yasunaga, M. Mehl, P. Oßwald, W.K. Metcalfe, C.K. Westbrook, W.J. Pitz, K. Kohse-Höinghaus, R.X. Fernandes, and H.J. Curran. A comprehensive chemical kinetic combustion model for the four butanol isomers. *Combust. and Flame*, 159(6):2028 – 2055, 2012.
- [16] P. Diévart, S.H. Won, S. Dooley, F.L. Dryer, and Y. Ju. A kinetic model for methyl decanoate combustion. *Combust. and Flame*, 159(5):1793 – 1805, 2012.
- [17] S.M. Sarathy, C.K. Westbrook, M. Mehl, W.J. Pitz, C. Togbe, P. Dagaut, H. Wang, M.A. Oehlschlaeger, U. Niemann, K. Seshadri, P.S. Veloo, C. Ji, F.N. Egolfopoulos, and T. Lu. Comprehensive chemical kinetic modeling of the oxidation of 2-methylalkanes from C7 to C20. *Combust. and Flame*, 158(12):2338 – 2357, 2011.
- [18] U.S. Department of Energy. Report of the basic energy sciences workshop on basic research needs for clean and efficient combustion of 21st century transportation fuels. http://science.energy.gov/~media/bes/pdf/reports/files/ctf_rpt.pdf, 2006.
- [19] D. Lee and S. Hochgreb. Hydrogen autoignition at pressures above the second explosion limit (0.6-4.0 MPa). *Int. J. Chem. Kinet.*, 30(6):385–406, 1998.
- [20] G. Mittal, C.J. Sung, and R.A. Yetter. Autoignition of H₂/CO at elevated pressures in a rapid compression machine. *Int. J. Chem. Kinet.*, 38(8):516–529, 2006.
- [21] G. Mittal, M.P. Raju, and C.J. Sung. Computational fluid dynamics modeling of hydrogen ignition in a rapid compression machine. *Combust. and Flame*, 155(3):417 – 428, 2008.
- [22] S.M. Gallagher, H.J. Curran, W.K. Metcalfe, D. Healy, J.M. Simmie, and G. Bourque. A rapid compression machine study of the oxidation of propane in the negative temperature coefficient regime. *Combust. and Flame*, 153(1 - 2):316 – 333, 2008.
- [23] D. Healy, H.J. Curran, J.M. Simmie, D.M. Kalitan, C.M. Zinner, A.B. Barrett, E.L. Petersen, and G. Bourque. Methane/ethane/propane mixture

- oxidation at high pressures and at high, intermediate and low temperatures. *Combust. and Flame*, 155(3):441 – 448, 2008.
- [24] S. Gersen, H. Darneveil, and H. Levinsky. The effects of CO addition on the autoignition of H₂, CH₄ and CH₄/H₂ fuels at high pressure in an RCM. *Combust. and Flame*, 159(12):3472 – 3475, 2012.
 - [25] A. Cox, J.F. Griffiths, C. Mohamed, H.J. Curran, W.J. Pitz, and C.K. Westbrook. Extents of alkane combustion during rapid compression leading to single-and two-stage ignition. *P. Combust. Inst.*, 26(2):2685 – 2692, 1996.
 - [26] M. Ribaucour, R. Minetti, L.R. Sochet, H.J. Curran, W.J. Pitz, and C.K. Westbrook. Ignition of isomers of pentane: An experimental and kinetic modeling study. *P. Combust. Inst.*, 28(2):1671 – 1678, 2000.
 - [27] T. Faravelli, P. Gaffuri, E. Ranzi, and J.F. Griffiths. Detailed thermokinetic modelling of alkane autoignition as a tool for the optimization of performance of internal combustion engines. *Fuel*, 77(3):147 – 155, 1998.
 - [28] D. Healy, N.S. Donato, C.J. Aul, E.L. Petersen, C.M. Zinner, G. Bourque, and H.J. Curran. n-butane: Ignition delay measurements at high pressure and detailed chemical kinetic simulations. *Combustion and Flame*, 157(8):1526 – 1539, 2010.
 - [29] G. Kukkadapu, K. Kumar, C.J. Sung, M. Mehl, and W.J. Pitz. Experimental and surrogate modeling study of gasoline ignition in a rapid compression machine. *Combust. and Flame*, 159(10):3066 – 3078, 2012.
 - [30] C.K. Westbrook, W.J. Pitz, J.E. Boercker, H.J. Curran, J.F. Griffiths, C. Mohamed, and M. Ribaucour. Detailed chemical kinetic reaction mechanisms for autoignition of isomers of heptane under rapid compression. *P. Combust. Inst.*, 29(1):1311 – 1318, 2002.
 - [31] S. Tanaka, F. Ayala, and J.C. Keck. A reduced chemical kinetic model for HCCI combustion of primary reference fuels in a rapid compression machine. *Combust. and Flame*, 133(4):467 – 481, 2003.
 - [32] X. He, M.T. Donovan, B.T. Zigler, T.R. Palmer, S.M. Walton, M.S. Wooldridge, and A. Atreya. An experimental and modeling study of iso-octane ignition delay times under homogeneous charge compression ignition conditions. *Combust. and Flame*, 142(3):266 – 275, 2005.
 - [33] S. Dooley, H.J. Curran, and J.M. Simmie. Autoignition measurements and a validated kinetic model for the biodiesel surrogate, methyl butanoate. *Combust. and Flame*, 153(1 - 2):2 – 32, 2008.
 - [34] S.M. Walton, D.M. Karwat, P.D. Teini, A.M. Gorny, and M.S. Wooldridge. Speciation studies of methyl butanoate ignition. *Fuel*, 90(5):1796 – 1804, 2011.

- [35] K. HadjAli, M. Crochet, G. Vanhove, M. Ribaucour, and R. Minetti. A study of the low temperature autoignition of methyl esters. *P. Combust. Inst.*, 32(1):239 – 246, 2009.
- [36] S.S. Goldsborough, C. Banyon, and G. Mittal. A computationally efficient, physics-based model for simulating heat loss during compression and the delay period in rcn experiments. *Combust. and Flame*, 159(012):3476 – 3492, 2012.
- [37] K. Kumar, G. Mittal, and C.J. Sung. Autoignition of n-decane under elevated pressure and low-to-intermediate temperature conditions. *Combust. and Flame*, 156(6):1278 – 1288, 2009.
- [38] D.F. Davidson, D.R. Haylett, and R.K. Hanson. Development of an aerosol shock tube for kinetic studies of low-vapor-pressure fuels. *Combust. and Flame*, 155(1-2):108 – 117, 2008.
- [39] C. Allen, G. Mittal, C.J. Sung, E. Toulson, and T. Lee. An aerosol rapid compression machine for studying energetic-nanoparticle-enhanced combustion of liquid fuels. *P. Combust. Inst.*, 33(2):3367 – 3374, 2011.
- [40] U.S. Energy Information Administration. Annual energy review 2011. <http://www.eia.gov/totalenergy/data/annual/pdf/aer.pdf>, 2012.
- [41] National Renewable Energy Laboratory/U.S. Department of Energy. Power technologies energy data book - fourth edition. www.nrel.gov/analysis/power_databook/docs/pdf/39728_complete.pdf, 2006.
- [42] Lawrence Livermore National Laboratory/U.S. Department of Energy. U.S. energy flow. https://flowcharts.llnl.gov/content/energy/energy_archive/energy_flow_2012/2012USEnergy.png, 2013.
- [43] M.M. El-Wakil. *Power plant technology*. McGraw-Hill, 1985.
- [44] J.B. Heywood. *Internal combustion engine fundamentals*. McGraw-Hill, 1988.
- [45] N. Brinkman, M. Wang, T. Weber, and T. Darlington. Well-to-wheels analysis of advanced fuel/vehicle systems – a north american study of energy use, greenhouse gas emissions, and criteria pollutant emissions. www.transportation.anl.gov/pdfs/TA/339.pdf, 2005.
- [46] T.J. Wallington, E.W. Kaiser, and T.J. Farrell. Automotive fuels and internal combustion engines: a chemical perspective. *Chem. Soc. Rev.*, 35:335 – 347, 2006.
- [47] W.J. Pitz, N.P. Cernansky, F.L. Dryer, F.N. Egolfopoulos, J.T. Farrell, D.G. Friend, and H. Pitsch. Development of an experimental database and chemical kinetic models for surrogate gasoline fuels. *SAE Paper*, 2007-01-0175, 2007.

- [48] J.T. Farrell, N.P. Cernansky, F.L. Dryer, C.K. Law, D.G. Friend, C.A. Hergart, R.M. McDavid, A.K. Patel, C.J. Mueller, and H. Pitsch. Development of an experimental database and kinetic models for surrogate diesel fuels. *SAE Paper*, 2007-01-0201, 2007.
- [49] M. Colket, J.T. Edwards, S. Williams, N.P. Cernansky, D.L. Miller, F.N. Egolfopoulos, P. Lindstedt, K. Seshadri, F.L. Dryer, C.K. Law, D.G. Friend, D.B. Lenhert, H. Pitsch, A. Sarofim, M. Smooke, and W. Tsang. Development of an experimental database and kinetic models for surrogate jet fuels. 45th AIAA Aerospace Sciences Meeting and Exhibit, Reno, Nevada, Paper No. AIAA-2007-0770, 2007.
- [50] O.J. Handaller and J.M. Johnson. World fuel sampling program. *CRC Report*, No. 647, 2007.
- [51] S. Dooley, S.H. Won, M. Chaos, J. Heyne, Y. Ju, F.L. Dryer, K. Kumar, C.J. Sung, H. Wang, M.A. Oehlschlaeger, R.J. Santoro, and T.A. Litzinger. A jet fuel surrogate formulated by real fuel properties. *Combust. and Flame*, 157(12):2333 – 2339, 2010.
- [52] G. Vanhove, G. Petit, and R. Minetti. Experimental study of the kinetic interactions in the low-temperature autoignition of hydrocarbon binary mixtures and a surrogate fuel. *Combust. and Flame*, 145(3):521 – 532, 2006.
- [53] K. Kohse-Höinghaus, P. Oßwald, T. A. Cool, T. Kasper, N. Hansen, F. Qi, C. K. Westbrook, and P. R. Westmoreland. Biofuel combustion chemistry: from ethanol to biodiesel. *Angew. Chem. Int. Ed.*, 49:3572–3597, 2010.
- [54] S.D. Sanford, J.M. White, P.S. Shah, C. Wee, M.A. Valverde, and G.R. Meier. Feedstock and biodiesel characteristics report. Renewable Energy Group, Inc., www.regfuel.com, 2009.
- [55] O. Herbinet, W.J. Pitz, and C.K. Westbrook. Detailed chemical kinetic oxidation mechanism for a biodiesel surrogate. *Combust. and Flame*, 154(3):507 – 528, 2008.
- [56] O. Herbinet, W.J. Pitz, and C.K. Westbrook. Detailed chemical kinetic mechanism for the oxidation of biodiesel fuels blend surrogate. *Combust. and Flame*, 157(5):893 – 908, 2010.
- [57] T.J. Bruno, A. Wolk, and A. Naydich. Composition-explicit distillation curves for mixtures of gasoline with four-carbon alcohols (butanols). *Energy Fuels*, 23:2295 – 2306, 2009.
- [58] T.J. Bruno and E. Baibourine. Comparison of biomass-derived turbine fuels with the composition-explicit distillation curve method. *Energy Fuels*, 25:1847 – 1858, 2011.
- [59] T.M. Lovestead, B.C. Windom, and T.J. Bruno. Investigating the unique properties of cuphea-derived biodiesel fuel with the advanced distillation curve method. *Energy Fuels*, 24:3665 – 3675, 2010.

- [60] L.S. Ott and T.J. Bruno. Variability of biodiesel fuel and comparison to petroleum-derived diesel fuel: Application of a composition and enthalpy explicit distillation curve method. *Energy Fuels*, 22:2261 – 2868, 2008.
- [61] C. Cooney, T. Wallner, and S. McConnell. Development and demonstration of a prototype omnivorous engine. DEER 2009 – Directions in Engine – Efficiency and Emissions Research Conference, Dearborn, MI, 2009.
- [62] P.M. Najt and D.E. Foster. Compression-ignited homogeneous charge combustion. *SAE Paper*, 830264, 1983.
- [63] R.H. Thring. Homogeneous-charge compression-ignition engines. *SAE Paper*, 892068, 1989.
- [64] M. Christensen, B. Johansson, and P. Einewall. Homogeneous charge compression ignition (HCCI) using isooctane, ethanol and natural gas – a comparison with spark-ignition operation. *SAE Paper*, 972874, 1989.
- [65] T. Ogura, J.P. Angelos, W.H. Green, W.K. Cheng, T.E. Kenney, and Y. Xu. Primary reference fuel behavior in a HCCI engine near the low-load limit. *SAE Paper*, 2008-01-1667, 2008.
- [66] https://www-pls.llnl.gov/?url=science_and_technology-chemistry-combustion.
- [67] K.K. Kuo. *Principles of combustion*. Cambridge University Press, 2nd edition, 2005.
- [68] T.H. Ballinger and P.J. Andersen. Vehicle comparison of advanced three-way catalysts and hydrocarbon trap catalysts. *SAE Paper*, 2002-01-0730, 2002.
- [69] H.G. Groeer and W. Schmidt. New engine for the golf. *MTZ Motortechnische Zeitschrift*, 54(7/8), 1993. (in German).
- [70] O.A. Kutlar, H. Arslan, and A.T. Calik. Methods to improve efficiency of four stroke, spark ignition engines at part load. *Energy Convers. Manage.*, 45:3202 – 3220, 2005.
- [71] T.H. Ma. Effect of variable engine valve timing on fuel economy. *SAE Paper*, 880390, 1988.
- [72] F.G. Wirbeleit, K. Binder, and D. Gwinner. Development of piston with variable compression height for increasing efficiency and specific power output of combustion engines. *SAE Paper*, 900229, 1990.
- [73] Y. Iwamoto, K. Noma, O. Nakayama, T. Yamauchi, and H. Ando. Development of gasoline direct injection engine. *SAE Paper*, 970541, 1997.
- [74] C.K. Law. *Combustion physics*. Cambridge University Press, 1st edition, 2006.

- [75] M. Baus, A. Cook, and D. Schaller. Integrating new emissions engines into commercial vehicles: emissions, performance & affordability. *SAE Paper*, 2006-01-3545, 2006.
- [76] J.B. Heywood. Improving the spark-ignition engine. Engine Research Center, 2005 Symposium, Madison, WI, 2005.
- [77] C. Mueller. Non-traditional fuels for high-efficiency, clean-combustion engines. Western states section of the combustion institute, fall technical meeting, Livermore, CA, 2007.
- [78] T. Kanda, T. Hakozaiki, T. Uchimoto, J. Hatano, N. Kitayama, and H. Sono. Pcci operation with fuel injection timing set close to TDC. *SAE Paper*, 2006-01-0920, 2006.
- [79] C. Mueller and A. Upatnieks. Dilute clean diesel combustion achieves low emissions and high efficiency while avoiding control problems of HCCI. 11th Annual Diesel Engine Emissions Reduction (DEER) Conference, Chicago, IL, 2005.
- [80] U.S. Department of Energy. Homogeneous charge compression ignition (HCCI) technology, a report to the U.S. congress. www-erdc.llnl.gov/FuelsoftheFuture/pdf_files/hccirtc.pdf, 2001.
- [81] S. Juttu, S.S. Thipse, N.V. Marathe, and M.K.G. Babu. Homogeneous charge compression ignition (HCCI): A new concept for near zero nox and particulate matter (pm) from diesel engine combustion. *SAE Paper*, 2007-26-020, 2007.
- [82] N. Milovanovic, D. Blundell, S. Gedge, and J. Turner. SI – HCCI – SI mode transition at different engine operating conditions. *SAE Paper*, 2005-01-0156, 2005.
- [83] <http://c3.nuigalway.ie/facilities.html>.
- [84] I. Celik, I. Yavuz, and A. Smirnov. Large eddy simulations of in-cylinder turbulence for internal combustion engines: a review. *Int. J. Engine Research*, 2(2):119 – 123, 2001.
- [85] J. Chen. Direct numerical simulation of turbulence-chemistry interactions: fundamental science toward predictive models. Accelerating Computational Science Symposium 2012, Washington D.C., 2012.
- [86] S.S. Goldsborough. A chemical kinetically based ignition delay correlation for iso-octane covering a wide range of conditions including the NTC region. *Combust. and Flame*, 156(6):1248 – 1262, 2009.
- [87] F. Maroteaux and L. Noel. Development of a reduced n-heptane oxidation mechanism for HCCI combustion modeling. *Combustion and Flame*, 146(1 - 2):246 – 267, 2006.

- [88] H.J. Curran, P. Gaffuri, W.J. Pitz, and C.K. Westbrook. A comprehensive modeling study of n-heptane oxidation. *Combust. and Flame*, 114(1-2):149–177, 1998.
- [89] W. H. Green, P. I. Barton, B. Bhattacharjee, D. M. Matheu, D. A. Schwer, J. Song, R. Sumathi, H.-H. Carstensen, A. M. Dean, and J. M. Grenda. Computer construction of detailed chemical kinetic models for gas-phase reactors. *Ind. Eng. Chem. Res.*, 40(23):5362–5370, 2001.
- [90] A.J. Gianola, T. Ichino, R.L. Hoenigman, S. Kato, V.M. Bierbaum, and W.C. Lineberger. Thermochemistry and electronic structure of the pyrrolyl radical. *J. Phys. Chem. A*, 108(46):10326, 2004.
- [91] S.W. Benson. *Thermochemical kinetics*. Wiley, 2nd edition, 1976.
- [92] <http://crf.sandia.gov/index.php/combustion-research-facility/combustion-chemistry/flame-chemistry/#.Ud9nNRpDsWM>.
- [93] http://hanson.stanford.edu/index.php?loc=facilities_kst.
- [94] <http://www.icare.cnrs-orleans.fr/spip.php?rubrique117&lang=en>.
- [95] Y. Zhang and A.L. Boehman. Experimental study of the autoignition of C₈H₁₆O₂ ethyl and methyl esters in a motored engine. *Combust. and Flame*, 157(3):546 – 555, 2010.
- [96] J.I. Steinfeld, J.S. Francisco, and W.L. Hase. *Chemical kinetics and dynamics*. Prentice Hall, 2nd edition, 1998.
- [97] M.T. Donovan, X. He, B. Zigler, T.R. Palmer, S.M. Walton, and M.S. Wooldridge. Experimental investigation of silane combustion and particle nucleation using a rapid-compression facility. *Combust. and Flame*, 141(4):360 – 370, 2005.
- [98] K. Kohse-Höinghaus, R. S. Barlow, M. Aldén, and J. Wolfrum. Combustion at the focus: laser diagnostics and control. *Proc. Combust. Inst.*, 30:89–123, 2005.
- [99] U. Struckmeier, A. Lucassen, N. Hansen, T. Wada, N. Peters, and K. Kohse-Höinghaus. Demonstration of a burner for the investigation of partially premixed low-temperature flames.
- [100] Recent contributions of flame-sampling molecular-beam mass spectrometry to a fundamental understanding of combustion chemistry. *Prog. Energ. Combust.*, 35, 2009.
- [101] P. Dagaut, M. Cathonnet, J.P. Rouan, R. Foulatier, A. Quilgars, J.C. Boettner, F. Gaillard, and H. James. A jet-stirred reactor for kinetic studies of homogenous gas-phase reactions at pressures up to ten atmospheres (~ 1 MPa). *J. Phys. E. Sci. Instrum.*, (19):207 – 209, 1986.

- [102] C.V. Callahan. Autoignition and emissions-related chemistry of primary reference fuels and gasoline components: flow reactor experiments at 9.6 and 12.5 atmospheres pressure. Master's thesis, Princeton University, 1995.
- [103] R.S. Tranter, D. Fulle, and K. Brezinsky. Design of a high-pressure single pulse shock tube for chemical kinetic investigations. *Rev. Sci. Instrum.*, 72:3046, 2001.
- [104] E.L. Petersen. *A shock tube and diagnostics for chemistry measurements at elevated pressures with application to methane ignition*. PhD thesis, Stanford University, 1998.
- [105] D. Darcy, C.J. Tobin, K. Yasunaga, J.M. Simmie, J. Würmel, W.K. Metcalfe, T. Niass, S.S. Ahmed, C.K. Westbrook, and H.J. Curran. A high pressure shock tube study of n-propylbenzene oxidation and its comparison with n-butylbenzene. *Combust. and Flame*, 159(7):2219 – 2232, 2012.
- [106] Z. Hong, D.F. Davidson, S.S. Vasu, and R.K. Hanson. The effect of oxygenates on soot formation in rich heptane mixtures: A shock tube study. *Fuel*, 88(10):1901 – 1906, 2009.
- [107] T. Malewicki, S. Gudiyaella, and K. Brezinsky. Experimental and modeling study on the oxidation of jet a and the n-dodecane/iso-octane/n-propylbenzene/1,3,5-trimethylbenzene surrogate fuel. *Combust. and Flame*, 160(1):17 – 30, 2013.
- [108] P. Beeley, P. Gray, and J.F. Griffiths. *Combust. and Flame*, 39, 1980.
- [109] G. Mittal. *A rapid compression machine – design, characterization, and autoignition investigations*. PhD thesis, Case Western Reserve University, 2006.
- [110] P. Park. *Rapid compression machine measurements of ignition delays for primary reference fuels*. PhD thesis, Massachusetts Institute of Technology, 1990.
- [111] M. Ribaucour, R. Minetti, M. Carlier, and L.R. Sochet. Autoinflammation à haute pression. Conception, réalisation et test d'une machine à compression rapide. *J. Chim. Phys.*, 89:2127 – 2152. (in French).
- [112] M.T. Donovan, X. He, B.T. Zigler, T.R. Palmer, M.S. Wooldridge, and A. Atreya. Demonstration of a free-piston rapid compression facility for the study of high temperature combustion phenomena. *Combust. and Flame*, 137(3):351 – 365, 2004.
- [113] S.S. Goldsborough, G. Mittal, and C. Banyon. Methodology to account for multi-stage ignition phenomena during simulations of RCM experiments. *P. Combust. Inst.*, 34(1):685 – 693, 2012.
- [114] S.M. Walton, X. He, B.T. Zigler, M.S. Wooldridge, and A. Atreya. An experimental investigation of iso-octane ignition phenomena. *Combust. and Flame*, 150(3):246 – 262, 2007.

- [115] C. Allen, E. Toulson, T. Edwards, and T. Lee. Application of a novel charge preparation approach to testing the autoignition characteristics of JP – 8 and camelina hydroprocessed renewable jet fuel in a rapid compression machine. *Combust. and Flame*, 159(9):2780 – 2788, 2012.
- [116] S.S. Goldsborough, M.V. Johnson, G.S. Zhu, and S.K. Aggarwal. Gas-phase saturation and evaporative cooling effects during wet compression of a fuel aerosol under RCM conditions. *Combust. and Flame*, 158(1):57 – 68, 2011.
- [117] S.S. Goldsborough, M.V. Johnson, G.S. Zhu, and S.K. Aggarwal. Fuel and diluent property effects during wet compression of a fuel aerosol under RCM conditions. *Fuel*, 93:454 – 467, 2012.
- [118] www.marinetechology.ie.
- [119] www.transportation.anl.gov/rcmworkshop/1st_workshop/images/organizations.png.
- [120] C.V. Callahan, T.J. Held, F.L. Dryer, R. Minetti, M. Ribaucour, L.R. Sochet, T. Faravelli, P. Gaffuri, and E. Rani. Experimental data and kinetic modeling of primary reference fuel mixtures. *P. Combust. Inst.*, 26(1):739 – 746, 1996.
- [121] Vladislav G. Slutsky, Sergei A. Tsyganov, and Eugeny S. Severin. The mechanism of high-temperature oxidation of carborane C₂B₄H₆ by water vapor. *P. Combust. Inst.*, 27(1):405 – 411, 1998.
- [122] C.K. Westbrook, H.J. Curran, W.J. Pitz, J.F. Griffiths, C. Mohamed, and S.K. Wo. The effects of pressure, temperature, and concentration on the reactivity of alkanes: Experiments and modeling in a rapid compression machine. *P. Combust. Inst.*, 27(1):371 – 378, 1998.
- [123] M. Ribaucour, R. Minetti, and L.R. Sochet. Autoignition of n-pentane and 1-pentene: Experimental data and kinetic modeling. *P. Combust. Inst.*, 27(1):345 – 351, 1998.
- [124] M. Ribaucour, O. Lemaire, and R. Minetti. Low-temperature oxidation and autoignition of cyclohexene: A modeling study. *P. Combust. Inst.*, 29(1):1303 – 1310, 2002.
- [125] G. Vanhove, M. Ribaucour, and R. Minetti. On the influence of the position of the double bond on the low-temperature chemistry of hexenes. *P. Combust. Inst.*, 30(1):1065 – 1072, 2005.
- [126] W.J. Pitz, C.V. Naik, T. Ní Mhaoldúin, C.K. Westbrook, H.J. Curran, J.P. Orme, and J.M. Simmie. Modeling and experimental investigation of methylcyclohexane ignition in a rapid compression machine. *P. Combust. Inst.*, 31(1):267 – 275, 2007.

- [127] W. Wang, Z. Li, M.A. Oehlschlaeger, D. Healy, H.J. Curran, S.M. Sarathy, M. Mehl, W.J. Pitz, and C.K. Westbrook. An experimental and modeling study of the autoignition of 3-methylheptane. *P. Combust. Inst.*, 34(1):335 – 343, 2012.
- [128] D.J. Cook and H. Pitsch. Enthalpy-based flamelet model for HCCI applied to a rapid compression machine. *SAE Paper*, 2005-01-3735, 2005.
- [129] J.F. Griffiths, R. Piazzesi, E.M. Sazhina, S.S. Sazhin, P.A. Glaude, and M.R. Heikal. CFD modelling of cyclohexane auto-ignition in an RCM. *Fuel*, 96:192 – 203, 2012.
- [130] T. Tsujimura, W.J. Pitz, F. Gillespie, H.J. Curran, B.W. Weber, Y. Zhang, and C.J. Sung. Development of isopentanol reaction mechanism reproducing autoignition character at high and low temperatures. *Energy Fuels*, 26(8):4871–4886, 2012.
- [131] G. Vanhove, R. Minetti, S. Touchard, R. Fournet, P.A. Glaude, and F. Battin-Leclerc. Experimental and modeling study of the autoignition of 1-hexene/isooctane mixtures at low temperatures. *Combust. and Flame*, 145(1 - 2):272 – 281, 2006.
- [132] D. Healy, N.S. Donato, C.J. Aul, E.L. Petersen, C.M. Zinner, G. Bourque, and H.J. Curran. Isobutane ignition delay time measurements at high pressure and detailed chemical kinetic simulations. *Combust. and Flame*, 157(8):1540 – 1551, 2010.
- [133] B. Husson, R. Bounaceur, K. Tanaka, M. Ferrari, O. Herbinet, P.A. Glaude, R. Fournet, F. Battin-Leclerc, M. Crochet, G. Vanhove, R. Minetti, C.J. Tobin, K. Yasunaga, J.M. Simmie, H.J. Curran, T. Niass, O. Mathieu, and S.S. Ahmed. Experimental and modeling study of the oxidation of n-butylbenzene. *Combust. and Flame*, 159(4):1399 – 1416, 2012.
- [134] J. Lavy, J.C. Dabadie, C. Angelberger, P. Duret, J. Willand, A. Juretzka, J. Schäfflein, T. Ma, Y. Lendresse, A. Satre, C. Schulz, H. KrÄdmer, H. Zhao, and L. Damiano. Innovative ultra-low NOx controlled auto-ignition combustion process for gasoline engines: the 4 – SPACE project. 2000-01-1837, 2000.
- [135] Y. Moriyoshi, S.H. Choi, and T. Tsunekawa. Instantaneous gas temperature measurement inside a combustion chamber using a two-wire thermocouple. *SAE Paper*, 2006-01-1344, 2006.
- [136] Y. Kim, K. Min, M.S. Kim, S.H. Chung, and C. Bae. Development of a reduced chemical kinetic mechanism and ignition delay measurement in a rapid compression machine for CAI combustion. *SAE Paper*, 2007-01-0218, 2007.
- [137] Y. Watanabe, K. Morikawa, T. Kuwahara, and M. Tanabe. Evaluation of homogeneous charge compression ignition at high engine speeds using a super rapid compression machine. *SAE Paper*, 2008-01-2403, 2008.

- [138] G. Mittal and S. Gupta. Computational assessment of an approach for implementing crevice containment in rapid compression machines. *Fuel*, 102(0):536 – 544, 2012.
- [139] A.K. Das, M. Uddi, and C.J. Sung. Two-line thermometry and H₂O measurement for reactive mixtures in rapid compression machine near 7.6 micron. *Combust. and Flame*, 159(12):995 – 1011, 2012.
- [140] R. Minetti, M. Carlier, M. Ribaucour, E. Therssen, and L.R. Sochet. A rapid compression machine investigation of oxidation and auto-ignition of n-heptane: Measurements and modeling. *Combust. and Flame*, 102(3):298 – 309, 1995.
- [141] J.F. Griffiths, P.A. Halford-Maw, and C. Mohamed. Spontaneous ignition delays as a diagnostic of the propensity of alkanes to cause engine knock. *Combust. and Flame*, 111(4):327 – 337, 1997.
- [142] C. Mohamed. Suppression of reaction during rapid compression and its effect on ignition delay. *Combust. and Flame*, 112(3):438 – 444, 1998.
- [143] R. Minetti, A. Roubaud, E. Therssen, M. Ribaucour, and L.R. Sochet. The chemistry of pre-ignition of n-pentane and 1-pentene. *Combust. and Flame*, 118(1 - 2):213 – 220, 1999.
- [144] A. Roubaud, O. Lemaire, R. Minetti, and L.R. Sochet. High pressure auto-ignition and oxidation mechanisms of o-xylene, o-ethyltoluene, and n-butylbenzene between 600 and 900 K. *Combust. and Flame*, 123(4):561 – 571, 2000.
- [145] O. Lemaire, M. Ribaucour, M. Carlier, and R. Minetti. The production of benzene in the low-temperature oxidation of cyclohexane, cyclohexene, and cyclohexa-1,3-diene. *Combust. and Flame*, 127(1 - 2):1971 – 1980, 2001.
- [146] S. Shiga, S. Ozone, H.T.C. Machacon, T. Karasawa, H. Nakamura, T. Ueda, N. Jingu, Z. Huang, M. Tsue, and M. Kono. A study of the combustion and emission characteristics of compressed-natural-gas direct-injection stratified combustion using a rapid-compression-machine. *Combust. and Flame*, 129(1 - 2):1 – 10, 2002.
- [147] J.F. Griffiths and B.J. Whitaker. Thermokinetic interactions leading to knock during homogeneous charge compression ignition. *Combust. and Flame*, 131(4):386 – 399, 2002.
- [148] S. Tanaka, F. Ayala, J.C. Keck, and J.B. Heywood. Two-stage ignition in HCCI combustion and HCCI control by fuels and additives. *Combust. and Flame*, 132:219 – 239, 2003.
- [149] X. He, B.T. Zigler, S.M. Walton, M.S. Wooldridge, and A. Atreya. A rapid compression facility study of OH time histories during iso-octane ignition. *Combust. and Flame*, 145(3):552 – 570, 2006.

- [150] G. Mittal and C.J. Sung. Autoignition of toluene and benzene at elevated pressures in a rapid compression machine. *Combust and Flame*, 150(4):355 – 368, 2007.
- [151] K. Kumar, G. Mittal, C.J. Sung, and C.K. Law. An experimental investigation of ethylene/O₂/diluent mixtures: Laminar flame speeds with preheat and ignition delays at high pressures. *Combust. and Flame*, 153(3):343 – 354, 2008.
- [152] D. Healy, H.J. Curran, S. Dooley, J.M. Simmie, D.M. Kalitan, E.L. Petersen, and G. Bourque. Methane/propane mixture oxidation at high pressures and at high, intermediate and low temperatures. *Combust. and Flame*, 155(3):451 – 461, 2008.
- [153] G. Mittal and C.J. Sung. Homogeneous charge compression ignition of binary fuel blends. *Combust. and Flame*, 155(3):431 – 439, 2008.
- [154] G. Mittal and C.J. Sung. Autoignition of methylcyclohexane at elevated pressures. *Combust. and Flame*, 156(9):1852 – 1855, 2009.
- [155] R. DiSante. Measurements of the auto-ignition of n-heptane/toluene mixtures using a rapid compression machine. *Combust. and Flame*, 159(1):55 – 63, 2012.
- [156] S. Dooley, S.H. Won, J. Heyne, T.I. Farouk, Y. Ju, F.L. Dryer, K. Kumar, X. Hui, C.J. Sung, H. Wang, M.A. Oehlschlaeger, V. Iyer, S. Iyer, T.A. Litzinger, R.J. Santoro, T. Malewicki, and K. Brezinsky. The experimental evaluation of a methodology for surrogate fuel formulation to emulate gas phase combustion kinetic phenomena. *Combust. and Flame*, 159(4):1444 – 1466, 2012.
- [157] C. Strozzi, A. Mura, J. Sotton, and M. Bellenoue. Experimental analysis of propagation regimes during the autoignition of a fully premixed methane-air mixture in the presence of temperature inhomogeneities. *Combust. and Flame*, 159(11):3323 – 3341, 2012.
- [158] P.D. Teini, D.M.A. Karwat, and A. Atreya. The effect of CO₂/H₂O on the formation of soot particles in the homogeneous environment of a rapid compression facility. *Combust. and Flame*, 159(3):1090 – 1099, 2012.
- [159] G. Mittal, M. Chaos, C.J. Sung, and F.L. Dryer. Dimethyl ether autoignition in a rapid compression machine: Experiments and chemical kinetic modeling. *Fuel Process. Technol.*, 89(12):1244 – 1254, 2008.
- [160] C.M. Allen, E. Toulson, D.L.S. Hung, H. Schock, D. Miller, and T. Lee. Ignition characteristics of diesel and canola biodiesel sprays in the low-temperature combustion regime. *Energy Fuels*, 25(7):2896–2908, 2011.
- [161] X. Hui, K. Kumar, C.J. Sung, T. Edwards, and D. Gardner. Experimental studies on the combustion characteristics of alternative jet fuels. *Fuel*, 98:176 – 182, 2012.

- [162] M.R. Turner, S.S. Sazhin, J.J. Healey, C. Crua, and S.B. Martynov. A breakup model for transient diesel fuel sprays. *Fuel*, 97:288 – 305, 2012.
- [163] K. Kumar and C.J. Sung. A comparative experimental study of the autoignition characteristics of alternative and conventional jet fuel/oxidizer mixtures. *Fuel*, 89(10):2853 – 2863, 2010.
- [164] S. Heyne, A. Roubaud, M. Ribaucour, G. Vanhove, R. Minetti, and D. Favrat. Development of a natural gas reaction mechanism for engine simulations based on rapid compression machine experiments using a multi-objective optimisation strategy. *Fuel*, 87(13 - 14):3046 – 3054, 2008.
- [165] S. Sazhin, C. Crua, D. Kennaird, and M. Heikal. The initial stage of fuel spray penetration. *Fuel*, 82(8):875 – 885, 2003.
- [166] J.F Griffiths, J.P MacNamara, C.G.W Sheppard, D.A Turton, and B.J Whitaker. The relationship of knock during controlled autoignition to temperature inhomogeneities and fuel reactivity. *Fuel*, 81(17):2219 – 2225, 2002.
- [167] K. Kumar and C.J. Sung. Autoignition of methanol: Experiments and computations. *Int. J. Chem. Kinet.*, 43(4):175–184, 2011.
- [168] A. Brassat, M. Thewes, M. Mütther, S. Pischinger, C. Lee, R. Xavier F., H. Olivier, and Y. Uygun. Analysis of the effects of certain alcohol and furan-based biofuels on controlled auto ignition. *SAE Paper*, 2012-01-1135, 2012.
- [169] A.C.S. Villela, S.L. Braga, J.C.C. Egúsquiza, and G.B. Machado. Rapid compression machine tests for brazilian Otto cycle fuels. *SAE Paper*, 2011-36-0349, 2011.
- [170] A.C.S. Villela, N.R. Moura, J.C.C. Egúsquiza, S.L. Braga, and C.V.M. Braga. Experimental investigation of the natural gas / diesel dual-fuel combustion using a rapid compression machine. *SAE Paper*, 2011-36-0360, 2011.
- [171] T. Hasegawa, M. Kinoshita, T. Arima, K. Sato, and M. Tanabe. Characteristics of HCCI combustion in homogenized temperature fields using a super rapid compression machine. *SAE Paper*, 2011-01-1761, 2011.
- [172] M. Katsumata, K. Morikawa, and M. Tanabe. Behavior of shock wave and pressure wave of SI knocking with super rapid compression machine. *SAE Paper*, 2011-01-1875, 2011.
- [173] M. Ohtomo, K. Nishikawa, T. Suzuoki, H. Miyagawa, and M. Koike. Auto-ignition characteristics of biofuel blends for SI engines. *SAE Paper*, 2011-01-1989, 2011.
- [174] S.B. Gupta, M. Biruduganti, B. Bihari, and R.R. Sekar. An overview of ARES research. *SAE Paper*, 2011-26-0085, 2011.

- [175] D. Shirota and N. Iida. An investigation of the potential of thermal and mixing stratifications for reducing pressure rise rate on HCCI combustion by using rapid compression machine. *SAE Paper*, 2009-32-0085, 2009.
- [176] K. Hashimoto. Inhibition effect of ethanol on homogeneous charge compression ignition of heptane. *SAE Paper*, 2008-01-2504, 2008.
- [177] H. Nakano, O.T. Lim, and N. Iida. An investigation of the effect of thermal stratification on HCCI combustion by using rapid compression machine. *SAE Paper*, 2007-01-1870, 2007.
- [178] K. Hashimoto. Effect of ethanol on the HCCI combustion. *SAE Paper*, 2007-01-2038, 2007.
- [179] K. Hotta, Y. Yoshikawa, K. Okuma, O. Moriue, and E. Murase. Characteristics of combustion in lean mixtures initiated by an imploding detonation plug. *SAE Paper*, 2007-01-1911, 2007.
- [180] O.T. Lim, H. Nakano, and N. Iida. The research about the effects of thermal stratification on n-heptane/iso-octane-air mixture HCCI combustion using a rapid compression machine. *SAE Paper*, 2009-01-3319, 2006.
- [181] S. Shiga, M. Araki, T. Obokata, Z. Huang, H. Ishti, T. Ueda, M. Tsue, and M. Kono. Basic aspect of combustion of CNG in cylinder direct-injection with spark-ignition. *SAE Paper*, 2005-26-352, 2005.
- [182] I. Saanum, M. Bysveen, T. AlmÅes, and O. K. SÅynju. Ignition and combustion characterization of hydrogen/methane mixtures by visualization in a rapid compression machine (RCM). *SAE Paper*, 2005-24-009, 2005.
- [183] G. Barroso, A. Escher, and K. Boulouchos. Experimental and numerical investigations on HCCI- combustion. *SAE Paper*, 2005-24-038, 2005.
- [184] S.B. Gupta, B. Bihari, R.S., G.M. Klett, and M. Ghaffarpour. Ignition characteristics of methane-air mixtures at elevated temperatures and pressures. *SAE Paper*, 2005-01-2189, 2005.
- [185] M. Hunzinger, S. Merkel, A. Nauwerck, A. Velji, and U. Spicher. Turbulent flame propagation with cold walls during lean combustion in SI-engines. *SAE Paper*, 2005-01-0238, 2005.
- [186] O.T. Lim, N. Sendoh, and N. Iida. Experimental study on HCCI combustion characteristics of n-heptane and iso-octane fuel/air mixture by the use of a rapid compression machine. *SAE Paper*, 2004-01-1968, 2004.
- [187] M. Furutani, T. Isogai, and Y. Ohta. Ignition characteristics of gaseous fuels and their difference elimination for SI and HCCI gas engines. *SAE Paper*, 2003-01-1857, 2003.

- [188] J. Jarosinski, J. Podfilipski, and A. Gorczakowski. Influence of turbulence on catalytic combustion in spark ignition engine. *SAE Paper*, 2003-01-0626, 2003.
- [189] E. Murase and K. Hanada. Control of the start of HCCI combustion by pulsed flame jet. *SAE Paper*, 2002-01-2867, 2002.
- [190] T. Kawakami and S. Okajima. A study of combustion characteristics of hydrocarbon-air mixtures at high temperature and pressure by using rapid compression machine. *SAE Paper*, 2001-28-0010, 2001.
- [191] K. Tanaka, H. Endo, A. Imamichi, Y. Oda, Y. Takeda, and T. Shimada. Study of homogeneous charge compression ignition using a rapid compression machine. *SAE Paper*, 2001-01-1033, 2001.
- [192] K.A. Heufer, J. Bugler, and H.J. Curran. A comparison of longer alkane and alcohol ignition including new experimental results for n-pentanol and n-hexanol. *P. Combust. Inst.*, 34(1):511 – 518, 2013.
- [193] G. Kukkadapu, K. Kumar, C.J. Sung, M. Mehl, and W.J. Pitz. Autoignition of gasoline and its surrogates in a rapid compression machine. *P. Combust. Inst.*, 34(1):345 – 352, 2013.
- [194] S. Vranckx, C. Lee, H.K. Chakravarty, and R.X. Fernandes. A rapid compression machine study of the low temperature combustion of cyclohexane at elevated pressures. *P. Combust. Inst.*, 34(1):377 – 384, 2013.
- [195] S. Gersen, A.V. Mokhov, J.H. Darneveil, H.B. Levinsky, and P. Glarborg. Ignition-promoting effect of NO₂ on methane, ethane and methane/ethane mixtures in a rapid compression machine. *P. Combust. Inst.*, 33(1):433 – 440, 2011.
- [196] G. Mittal, C.J. Sung, M. Fairweather, A.S. Tomlin, J.F. Griffiths, and K.J. Hughes. Significance of the HO₂ + CO reaction during the combustion of CO + H₂ mixtures at high pressures. *P. Combust. Inst.*, 31(1):419 – 427, 2007.
- [197] E.J. Silke, H.J. Curran, and J.M. Simmie. The influence of fuel structure on combustion as demonstrated by the isomers of heptane: a rapid compression machine study. *P. Combust. Inst.*, 30(2):2639 – 2647, 2005.
- [198] R. Minetti, M. Carlier, M. Ribaucour, E. Therssen, and L.R. Sochet. Comparison of oxidation and autoignition of the two primary reference fuels by rapid compression. *P. Combust. Inst.*, 26(1):747 – 753, 1996.
- [199] E. Ranzi, T. Faravelli, P. Gaffuri, A. Sogaro, A. D’Anna, and A. Ciajolo. A wide-range modeling study of iso-octane oxidation. *Combust. and Flame*, 108(1 - 2):24 – 42, 1997.
- [200] H.J. Curran, P. Gaffuri, W.J. Pitz, and C.K. Westbrook. A comprehensive modeling study of n-heptane oxidation. *Combust. and Flame*, 114(1 - 2):149 – 177, 1998.

- [201] S. Granata, T. Faravelli, and E. Ranzi. A wide range kinetic modeling study of the pyrolysis and combustion of naphthenes. *Combust. and Flame*, 132(3):533 – 544, 2003.
- [202] S. Liu, J.C. Hewson, J.H. Chen, and H. Pitsch. Effects of strain rate on high-pressure nonpremixed n-heptane autoignition in counterflow. *Combust. and Flame*, 137(3):320 – 339, 2004.
- [203] J. Andrae, D. Johansson, P. Björnbom, P. Risberg, and G. Kalghatgi. Co-oxidation in the auto-ignition of primary reference fuels and n-heptane/toluene blends. *Combust. and Flame*, 140(4):267 – 286, 2005.
- [204] F. Buda, R. Bounaceur, V. Warth, P.A. Glaude, R. Fournet, and F. Battin-Leclerc. Progress toward a unified detailed kinetic model for the autoignition of alkanes from C4 to C10 between 600 and 1200 K. *Combust. and Flame*, 142(1 - 2):170 – 186, 2005.
- [205] M. Mehl, G. Vanhove, W.J. Pitz, and E. Ranzi. Oxidation and combustion of the n-hexene isomers: A wide range kinetic modeling study. *Combust. and Flame*, 155(4):756 – 772, 2008.
- [206] J.C.G. Andrae, T. Brinck, and G.T. Kalghatgi. HCCI experiments with toluene reference fuels modeled by a semidetailed chemical kinetic model. *Combust. and Flame*, 155(4):696 – 712, 2008.
- [207] C.K. Westbrook, W.J. Pitz, O. Herbinet, H.J. Curran, and E.J. Silke. A comprehensive detailed chemical kinetic reaction mechanism for combustion of n-alkane hydrocarbons from n-octane to n-hexadecane. *Combust. and Flame*, 156(1):181 – 199, 2009.
- [208] J.M. Anderlohr, R. Bounaceur, A. Pires Da Cruz, and F. Battin-Leclerc. Modeling of autoignition and NO sensitization for the oxidation of IC engine surrogate fuels. *Combust. and Flame*, 156(2):505 – 521, 2009.
- [209] M.I. Strelkova, A.A. Safonov, L.P. Sukhanov, S.Y. Umanskiy, I.A. Kirillov, B.V. Potapkin, H.J. Pasman, and A.M. Tentner. Low temperature n-butane oxidation skeletal mechanism, based on multilevel approach. *Combust. and Flame*, 157(4):641 – 652, 2010.
- [210] S.P. Medvedev, G.L. Agafonov, S.V. Khomik, and B.E. Gelfand. Ignition delay in hydrogen-air and syngas-air mixtures: Experimental data interpretation via flame propagation. *Combust. and Flame*, 157(7):1436 – 1438, 2010.
- [211] Y. Ra and R.D. Reitz. A combustion model for IC engine combustion simulations with multi-component fuels. *Combust. and Flame*, 158(1):69 – 90, 2011.
- [212] I.Gy. Zsély, T. Nagy, J.M. Simmie, and H.J. Curran. Reduction of a detailed kinetic model for the ignition of methane/propane mixtures at gas turbine conditions using simulation error minimization methods. *Combust. and Flame*, 158(8):1469 – 1479, 2011.

- [213] J.C. Prince and F.A. Williams. Short chemical-kinetic mechanisms for low-temperature ignition of propane and ethane. *Combust. and Flame*, 159(7):2336 – 2344, 2012.
- [214] G. Lodier, C. Merlin, P. Domingo, L. Vervisch, and F. Ravet. Self-ignition scenarios after rapid compression of a turbulent mixture weakly-stratified in temperature. *Combust. and Flame*, 159(11):3358 – 3371, 2012.
- [215] W. K. Metcalfe, S. Dooley, and F. L. Dryer. Comprehensive detailed chemical kinetic modeling study of toluene oxidation. *Energy Fuels*, 25(11):4915 – 4936, 2011.
- [216] E. Toulson, C.M. Allen, D.J. Miller, J. McFarlane, H.J. Schock, and T. Lee. Modeling the autoignition of fuel blends with a multistep model. *Energy Fuels*, 25(2):632 – 639, 2011.
- [217] E. Toulson, C.M. Allen, D.J. Miller, H.J. Schock, and T. Lee. Optimization of a multi-step model for the auto-ignition of dimethyl ether in a rapid compression machine. *Energy Fuels*, 24(6):3510 – 3516, 2010.
- [218] D. Healy, M.M. Kopp, N.L. Polley, E.L. Petersen, G. Bourque, and H.J. Curran. Methane/n-butane ignition delay measurements at high pressure and detailed chemical kinetic simulations. *Energy Fuels*, 24(3):1617 – 1627, 2010.
- [219] D. Healy, D.M. Kalitan, C.J. Aul, E.L. Petersen, G. Bourque, and H.J. Curran. Oxidation of C1&LSC5 alkane quinary natural gas mixtures at high pressures. *Energy Fuels*, 24(3):1521 – 1528, 2010.
- [220] E. Toulson, C.M. Allen, D.J. Miller, and T. Lee. Modeling the auto-ignition of oxygenated fuels using a multistep model. *Energy Fuels*, 24(2):888 – 896, 2010.
- [221] C. Huang, X. Lu, and Z. Huang. New reduced chemical mechanism for homogeneous charge combustion ignition combustion investigation of primary reference fuels. *Energy Fuels*, 22(2):935 – 944, 2008.
- [222] F. Buda, B. Heyberger, R. Fournet, P.A. Glaude, V. Warth, and F. Battin-Leclerc. Modeling of the gas-phase oxidation of cyclohexane. *Energy Fuels*, 20(4):1450 – 1459, 2006.
- [223] E.M. Sazhina, S.S. Sazhin, M.R. Heikal, and C.J. Marooney. The shell autoignition model: applications to gasoline and diesel fuels. *Fuel*, 78(4):389 – 401, 1999.
- [224] M. Jia and M. Xie. A chemical kinetics model of iso-octane oxidation for HCCI engines. *Fuel*, 85(17 - 18):2593 – 2604, 2006.
- [225] H. Xu, C. Yao, and G. Xu. Chemical kinetic mechanism and a skeletal model for oxidation of n-heptane/methanol fuel blends. *Fuel*, 93:625 – 631, 2012.

- [226] M.P. Burke, M. Chaos, Y. Ju, F.L. Dryer, and S.J. Klippenstein. Comprehensive H₂/O₂ kinetic model for high-pressure combustion. *Int. J. Chem. Kinet.*, 44(7):444 – 474, 2012.
- [227] A. Saylam, M. Ribaucour, W.J. Pitz, and R. Minetti. Reduction of large detailed chemical kinetic mechanisms for autoignition using joint analyses of reaction rates and sensitivities. *Int. J. Chem. Kinet.*, 39(4):181 – 196, 2007.
- [228] J. Li, Z. Zhao, A. Kazakov, M. Chaos, F.L. Dryer, and J.J. Scire. A comprehensive kinetic mechanism for CO, CH₂O, and CH₃OH combustion. *Int. J. Chem. Kinet.*, 39(3):109 – 136, 2007.
- [229] M. Cord, B. Sirjean, R. Fournet, A. Tomlin, M. Ruiz-Lopez, and F. Battin-Leclerc. Improvement of the modeling of the low-temperature oxidation of n-butane: Study of the primary reactions. *J. Phys. Chem. A*, 116(24):6142 – 6158, 2012.
- [230] X. You, H. Wang, E. Goos, C.J. Sung, and S.J. Klippenstein. Reaction kinetics of CO + HO₂ → products: ab initio transition state theory study with master equation modeling. *J. Phys. Chem. A*, 111(19):4031 – 4042, 2007. PMID: 17388389.
- [231] E.J. Silke, W.J. Pitz, C.K. Westbrook, and M. Ribaucour. Detailed chemical kinetic modeling of cyclohexane oxidation. *J. Phys. Chem. A*, 111(19):3761 – 3775, 2007. PMID: 17388266.
- [232] S.S. Goldsborough, T.A. Smith, M.V. Johnson, and S.S. McConnell. Evaluation of ignition timing predictions using control-oriented models in kinetically-modulated combustion regimes. *SAE Paper*, 2012-01-1136, 2012.
- [233] T. Tsujimura, W.J. Pitz, Y. Yang, and J.E. Dec. Detailed kinetic modeling of HCCI combustion with isopentanol. *SAE Paper*, 2011-24-0023:257–270, 2011.
- [234] K.V. Puduppakkam, C.V. Naik, C. Wang, and E. Meeks. Validation studies of a detailed kinetics mechanism for diesel and gasoline surrogate fuels. *SAE Paper*, 2010-01-0545, 2010.
- [235] M. Mehl, W.J. Pitz, M. Sjöberg, and J.E. Dec. Detailed kinetic modeling of low-temperature heat release for PRF fuels in an HCCI engine. *SAE Paper*, 2009-01-1806, 2009.
- [236] M. Mehl, T. Faravelli, E. Ranzi, F. Giavazzi, P. Scorletti, D. Terna, G. D’Errico, T. Lucchini, and A. Onorati. Kinetic modelling study of octane number and sensitivity of hydrocarbon mixtures in CFR engines. *SAE Paper*, 2005-24-077, 2005.
- [237] K. Nishiwaki, Y. Yoshihara, and K. Saijyo. Numerical analysis of the location of knock initiation in S.I. engines. *SAE Paper*, 2000-01-1897, 2000.

- [238] M. Mehl, W.J. Pitz, C.K. Westbrook, and H.J. Curran. Kinetic modeling of gasoline surrogate components and mixtures under engine conditions. *P. Combust. Inst.*, 33(1):193 – 200, 2011.
- [239] M. Mehl, W.J. Pitz, C.K. Westbrook, K. Yasunaga, C. Conroy, and H.J. Curran. Autoignition behavior of unsaturated hydrocarbons in the low and high temperature regions. *P. Combust. Inst.*, 33(1):201 – 208, 2011.
- [240] P. Diévart and P. Dagaut. The oxidation of n-butylbenzene: Experimental study in a JSR at 10 atm and detailed chemical kinetic modeling. *P. Combust. Inst.*, 33(1):209 – 216, 2011.
- [241] C.V. Naik, C.K. Westbrook, O. Herbinet, W.J. Pitz, and M. Mehl. Detailed chemical kinetic reaction mechanism for biodiesel components methyl stearate and methyl oleate. *P. Combust. Inst.*, 33(1):383 – 389, 2011.
- [242] R. Bounaceur, V. Warth, B. Sirjean, P.A. Glaude, R. Fournet, and F. Battin-Leclerc. Influence of the position of the double bond on the autoignition of linear alkenes at low temperature. *P. Combust. Inst.*, 32(1):387 – 394, 2009.
- [243] Y. Sakai, A. Miyoshi, M. Koshi, and W.J. Pitz. A kinetic modeling study on the oxidation of primary reference fuel-toluene mixtures including cross reactions between aromatics and aliphatics. *P. Combust. Inst.*, 32(1):411 – 418, 2009.
- [244] S. Honnet, K. Seshadri, U. Niemann, and N. Peters. A surrogate fuel for kerosene. *P. Combust. Inst.*, 32(1):485 – 492, 2009.
- [245] C. Cavallotti, R. Rota, T. Faravelli, and E. Ranzi. Ab initio evaluation of primary cyclo-hexane oxidation reaction rates. *P. Combust. Inst.*, 31(1):201 – 209, 2007.
- [246] S. Touchard, R. Fournet, P.A. Glaude, V. Warth, F. Battin-Leclerc, G. Vanhove, M. Ribaucour, and R. Minetti. Modeling of the oxidation of large alkenes at low temperature. *P. Combust. Inst.*, 30(1):1073 – 1081, 2005.
- [247] J.F. Griffiths, K.J. Hughes, and R. Porter. The role and rate of hydrogen peroxide decomposition during hydrocarbon two-stage autoignition. *P. Combust. Inst.*, 30(1):1083 – 1091, 2005.
- [248] G. Mittal, M.P. Raju, and A. Bhari. A numerical assessment of the novel concept of crevice containment in a rapid compression machine. *Combust. and Flame*, 158(12):2420 – 2427, 2011.
- [249] G. Mittal, M.P. Raju, and C.J. Sung. CFD modeling of two-stage ignition in a rapid compression machine: Assessment of zero-dimensional approach. *Combust. and Flame*, 157(7):1316 – 1324, 2010.

- [250] J. Wurmel, E.J. Silke, H.J. Curran, M.S. O Conaire, and J.M. Simmie. The effect of diluent gases on ignition delay times in the shock tube and in the rapid compression machine. *Combust. and Flame*, 151(1 - 2):289 – 302, 2007.
- [251] G. Mittal and C.J. Sung. Aerodynamics inside a rapid compression machine. *Combust. and Flame*, 145(1 - 2):160 – 180, 2006.
- [252] J. Wurmel and J.M. Simmie. CFD studies of a twin-piston rapid compression machine. *Combust. and Flame*, 141(4):417 – 430, 2005.
- [253] J. Clarkson, J.F. Griffiths, J.P. MacNamara, and B.J. Whitaker. Temperature fields during the development of combustion in a rapid compression machine. *Combust. and Flame*, 125(3):1162 – 1175, 2001.
- [254] L. Brett, J. Macnamara, P. Musch, and J.M. Simmie. Simulation of methane autoignition in a rapid compression machine with creviced pistons. *Combust. and Flame*, 124(1 - 2):326 – 329, 2001.
- [255] D. Lee and S. Hochgreb. Rapid compression machines: Heat transfer and suppression of corner vortex. *Combust. and Flame*, 114(3 - 4):531 – 545, 1998.
- [256] G. Mittal, M.P. Raju, and C.J. Sung. Vortex formation in a rapid compression machine: Influence of physical and operating parameters. *Fuel*, 94:409 – 417, 2012.
- [257] K.G. Falk. The ignition temperatures of gaseous mixtures. *J. Am. Chem. Soc.*, 29(11):1536 – 1557, 1907.
- [258] K.G. Falk. The ignition temperatures of hydrogen-oxygen mixtures. *J. Am. Chem. Soc.*, 28(2):1517 – 1534, 1906.
- [259] H.B. Dixon, L. Bradshaw, and C. Campbell. The firing of gases by adiabatic compression. part i. photographic analysis of the flame. *J. Chem. Soc.*, (105):2027 – 2035, 1914.
- [260] H.B. Dixon and J.M. Crofts. The firing of gases by adiabatic compression. part ii. the ignition-points of mixtures containing electrolytic gas. *J. Chem. Soc.*, (105):2036 – 2053, 1914.
- [261] H.T. Tizard and D.R. Pye. Experiments on the ignition of gases by sudden compression. *Philos. Mag.*, 44(259):79 – 121, 1922.
- [262] An opposed piston rapid compression machine for preflame reaction studies. *Proc. Instn. Mech. Engrs.*, 183(19):183 – 365, 1968.
- [263] A. Bhari. A rapid compression machine with the novel concept of crevice containment. Master’s thesis, University of Akron, 2009.

- [264] S.S. Goldsborough, S.A. Ciatti, C. Banyon, and M.V. Johnson. Rapid compression machine experiments of transportation relevant fuels. First international RCM workshop, Argonne, IL, 2012.
www.transportation.anl.gov/rcmworkshop/1st_workshop/posters/SGoldsborough.ANL.RCM.pdf.
- [265] M. Uddi, A.K. Das, and C.J. Sung. Temperature measurements in a rapid compression machine using mid-infrared H₂O absorption spectroscopy near 7.6 μm . *Appl. Opt.*, 51(22):5464 – 5476, 2012.
- [266] D. Darcy, H. Nakamura, C.J. Tobin, M. Mehl, W.K. Metcalfe, W.J. Pitz, C.K. Westbrook, and H.J. Curran. A high-pressure rapid compression machine study of n-propylbenzene ignition. *Combust. and Flame*, 161(1):65 – 74, 2014.
- [267] W.A. Sirignano. *Fluid dynamics and transport of droplets and sprays*. Cambridge University Press, 1999.
- [268] W. Kays, M. Crawford, and B. Weigand. *Convective heat and mass transfer*. McGraw Hill, fourth edition, 2005.
- [269] K.K. Adane and M.F. Tachie. Numerical investigation of three-dimensional laminar wall jet of Newtonian and non – Newtonian fluids. *AIAA*, 46(11):2868 – 2880, 2008.
- [270] J.M. Villafruela, F. Castro, and M.T. Parra. Experimental study of parallel and inclined turbulent wall jets. *Exp. Thermal Fluid Sci.*, 33(1):132 – 139, 2008.
- [271] G.S. Zhu and S.K. Aggarwal. Fuel droplet evaporation in a supercritical environment. *J. Eng. Gas Turb. Power*, 124(4):762 – 770, 2002.
- [272] A.F. Polley. Droplet behavior in dense, low velocity aerosols. Master’s thesis, Marquette University, 2012.
- [273] B.E. Poling, J.M. Prausnitz, and J.P. O’Connell. *The properties of gases and liquids*. McGraw-Hill, 5th edition, 2001.
- [274] B.J. McBride, S. Gordon, and M.A. Reno. NASA report TM – 4513. 1993.
ntrs.nasa.gov/archive/nasa/casi.ntrs.nasa.gov/19940013151_1994013151.pdf.
- [275] A. Bondi. *Physical properties of molecular crystals, liquids and glasses*. Wiley, 1968.
- [276] V. Rùzicka and E.S. Domalski. Estimation of the heat capacities of organic liquids as a function of temperature using group additivity. I. hydrocarbon compounds. *J. Phys. Chem. Ref. Data*, 22(3):597 – 618, 1993.
- [277] K. Wark. *Advanced thermodynamics for engineers*. McGraw-Hill, 1994.
- [278] T. Yamada and R.D. Gunn. Saturated liquid molar volumes. the Rackett equation. *J. Chem. Eng. Data*, 18:234 – 236, 1973.

- [279] P.L. Chueh and J.M. Prausnitz. Vapor-liquid equilibria at high pressures. vapor fugacity coefficients in nonpolar and quantum-gas mixtures. *Ind. Eng. Chem. Fundam.*, 6(4):492 – 498, 1967.
- [280] T.H. Chung, L.L. Lee, and K.E. Starling. Applications of kinetic gas theories and multiparameter correlation for prediction of dilute gas viscosity and thermal conductivity. *Ind. Eng. Chem. Fundam.*, 23:8 – 13, 1984.
- [281] T.H. Chung, M. Ajlan, L.L. Lee, and K.E. Starling. Generalized multiparameter correlation for nonpolar fluid transport-properties. *Ind. Eng. Chem. Res.*, 27:671 – 679, 1988.
- [282] P.D. Neufeld, A.R. Janzen, and R.A. Aziz. Empirical equations to calculate 16 of the transport collision integrals for the Lennard-Jones (12-6) potential. *J. Chem. Phys.*, 57:1100 – 1102, 1972.
- [283] C.R. Wilke. A viscosity equation for gas mixtures. *J. Chem. Phys.*, 18(4):517 – 519, 1950.
- [284] R.B. Bird, W.E. Stewart, and E.W. Lightfoot. *Transport phenomena*. Wiley, 2nd edition, 2006.

Appendices

Appendix A

Thermophysical and Transport Properties

This appendix outlines the various thermophysical and transport property models utilized by the new MP-MZM. A few modifications have been made to the referenced specific heat fits in order to accommodate the scheme used here to calculate two-phase intensive energies. Details of this modification are provided below. Models for transport coefficients have mainly been employed based on the suggestions of ref. [273], where these details are also provided in this appendix.

Specific Heat

Gas-phase specific heat is evaluated for each species from the ideal gas (IG) NASA polynomial fits [274], which have the functional form of Eq. (A.1).

$$\frac{C_{p,j}^o}{R} = a_{NASA,j} + b_{NASA,j}T + c_{NASA,j}T^2 + d_{NASA,j}T^3 + f_{NASA,j}T^4 \quad (\text{A.1})$$

The numerical coefficients a through f are obtained from ref. [274]. For the new model only the low-temperature fits of specific heats are utilized, where both low-temperature and high-temperature fits are available. This is due to slightly non-monotonic behavior in specific heats at the splitting temperatures (typically ~ 1000 - 1500 K), which causes numerical instabilities when inferring temperatures from gas internal energies and also artificial energy increases near the fit splitting temperatures. Also, the low-temperature fits for gas specific

heats have been extrapolated beyond their suggested low-temperature limit (typically ~ 300 K), in order to calculate liquid-phase specific heats.

Currently, liquid-phase specific heats are calculated as a departure from IG specific heats by employing the corresponding states principle (CSP). More specifically, the form given by ref. [275], i.e. Eq. (A.2), is used with the modified coefficients suggested by ref. [273] to better match experimental data for liquid Ar, which is often used as a gas diluent in RCM experiments.

$$\begin{aligned} \frac{C_{p,l,j}}{R} = 1.586 + \frac{0.49}{1 - T_{r,j}} + \omega_j \left[4.2775 + \frac{6.3(1 - T_{r,j})^{1/3}}{T_{r,j}} \right. \\ \left. + \frac{0.4355}{1 - T_{r,j}} \right] + \frac{C_{p,j}^o}{R} \end{aligned} \quad (\text{A.2})$$

The RHS of Eq. (A.2) has been slightly modified to achieve a computationally-efficient MP-MZM framework. As will become apparent shortly, enthalpies are calculated by integrating specific heats with respect to temperature. An analytic solution for $\int 6.3(1 - T_{r,j})^{1/3}/T_{r,j} dT$ does not exist, thus a computationally expensive numerical integration method must be employed to evaluate enthalpies from Eq. (A.2). For the work presented in this thesis, an analytic solution for internal energy is obtained by fitting the problematic term in Eq. (A.2) to a polynomial, which is given by Eq. (A.3). From inspection of Figure A.1 the error introduced by modifying this term is thought to be small compared to the error associated with using the original CSP fit.

$$\begin{aligned} 6.3(1 - T_{r,j})^{1/3} \approx 0.9882 - 0.1013 T_{r,j} - 1.3324 T_{r,j}^2 + 2.2870 T_{r,j}^3 \\ - 1.5661 T_{r,j}^4 \end{aligned} \quad (\text{A.3})$$

A parabolic functional form, i.e. Eq. (A.4), for evaluating liquid specific heat, as suggested by ref. [276], was also investigated for use in the MP-MZM.

$$\frac{C_{p,l,j}}{R} = a_{RD,j} + b_{RD,j} \frac{T}{100} + d_{RD,j} \left(\frac{T}{100} \right)^2 \quad (\text{A.4})$$

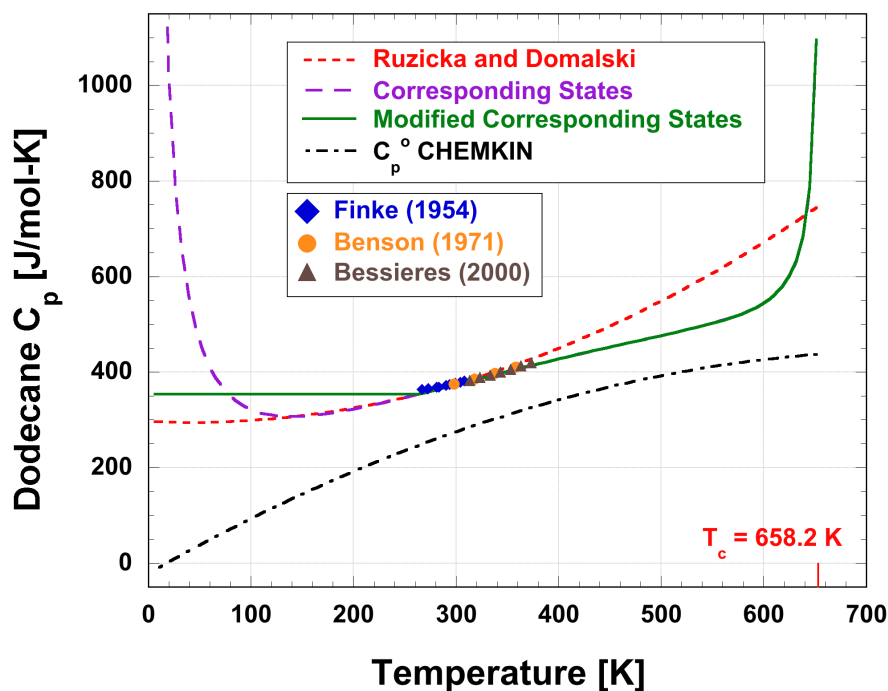


Figure A.1: A schematic of the multi-phase flow through the piston crevice.

Here the coefficients a , b and d are estimated using Benson-style group additivity methods. While having a much simpler form this correlation was found to be ill-suited for the MP-MZM, where typically Eq. (A.4) poorly predicts values for specific heat at temperatures that greatly deviate from the normal boiling temperature.

This departure is demonstrated in Figure A.1, where Eqs. (A.1), (A.2), (A.2)+(A.3) and (A.4) are used to calculate the specific heat of n-dodecane. The parabolic fit of Ruzicka and Domalski does a reasonable job approximating the liquid specific heat over the limited temperature range where experimental validation data is available. However, the fit does a poor job of capturing the rapid increase in liquid specific heat near the critical point, while CSP fit has previously been shown to correctly predict the physics in this region [273]. The CSP model blows up as temperatures approaches zero, which is numerically problematic for the MP-MZM when root-solving for temperatures from internal energies. Even though RCM gases do not reach these temperatures during

experiments, a very low temperature (~ 40 K) is selected for a thermodynamic reference state so that diluent, oxidizer and fuels share a common (liquid) phase from where energies are referenced. To facilitate a stable solution scheme for gas and liquid temperatures, a constant liquid specific heat is utilized below temperatures of $T_{r,j}=0.4$.

Energy

Liquid enthalpies are calculated from the definition of specific heat at constant pressure (i.e. $dh/dT = C_p$), and more specifically for this formulation by Eq. (A.5).

$$h_{l,j} = (T_{split,j} - T_{ref})C_{p,l,j}\Big|_{T_{split,j}} + \int_{T_{split,j}}^T C_{p,l,j} dT^{**} + h_{ref} \quad (\text{A.5})$$

Here a constant liquid specific heat, evaluated at $T_{split,j} = 0.4T_{crit,j}$, is used to calculate liquid enthalpies at low temperatures (i.e. $T < T_{split,j}$) for the reasons discussed above. At temperatures above $T_{split,j}$ Eq. (A.2), with the modification presented by Eq. (A.3) is analytically integrated to obtain enthalpies. A single reference temperature and enthalpy are chosen to be consistent between all species, which ensures a consistent reference (liquid) phase between diluents, oxidizers and fuels. For the simulations presented in this thesis, a reference temperature of $T_{ref}=40$ K and reference enthalpy of $h_{ref}=1000$ J/mol were used.

Calculating gas-phase enthalpies that are consistent with the liquid phase by employing property models is a bit more challenging. This approach was originally undertaken instead of calculating thermophysical properties from a state equation so that a wide variety of chemical species can be investigated, where state equations with few parameters are typically only rigorously validated for a few types of species. While a consistent framework for gas-phase enthalpy

was successfully developed and demonstrated by utilizing property models, more elegant state equation methods for calculating thermodynamic properties may be explored in the future.

Gas-phase enthalpies are calculated in a manner similar to the liquid-phase enthalpies, using Eq. (A.6), where Eq. (A.1) is analytically integrated with respect to temperature.

$$h_{v,j} = h_{l,j}(T = \bar{T}_{b,j}) + \Delta h_{vap,j}(T = \bar{T}_{b,j}) + \int_{\bar{T}_{b,j}}^T C_{p,j}^o dT^{**} \quad (\text{A.6})$$

In addition to gas-phase sensible heating, the gas-phase enthalpies also carry information about the sensible heating prior to vaporization as well as the phase-change temperature and energy. In this sense, the enthalpies calculated from Eq. (A.6) are *total* gas-phase enthalpies. This complex tracking of the conditions prior to vaporization is required to ensure that energies are conserved during two-phase simulations. Evaluating total gas-phase enthalpies is achieved by integrating the liquid specific heat from the reference state to the boiling temperature, adding the vaporization enthalpy at the boiling temperature and finally integrating the gas specific heat to account for sensible gas-phase heating.

Diluent and oxidizer species (e.g. N₂, Ar, O₂, etc.) are loaded into the reaction chamber in the gas phase, and are not allowed to condense in the MP-MZM. For these species the normal boiling temperature is used to evaluate the pre-vaporization sensible heating and vaporization enthalpy, which assumes that the species were vaporized at atmospheric pressure before being loaded into the machine.

Determining a boiling temperature for fuel species that can be used in Eq. (A.6) is more challenging. A rigorous approach would be to track the amount and temperature of each vaporizing fuel species at each time step, however this approach is infeasible. The memory requirements to store this information would limit the number of computational zones and species able to

be simulated. Also, root solving gas temperature from Eq. (A.6) would be numerically challenging and computationally expensive. Thus, a computationally-efficient, reduced order approach is utilized in the MP-MZM framework, given by Eq. (A.7).

$$\bar{T}_{b,j} = \frac{\int_{t_0}^t T_{b,j} \dot{n}_{PC,j} dt^{**}}{\int_{t_0}^t \dot{n}_{PC,j} dt^{**}} \quad (\text{A.7})$$

Here a rolling average boiling temperature is used for each species, where this molar weighted temperature is updated at every time step based on the cumulative amount of fuel vaporized at a given temperature.

Vaporization enthalpies are calculated from a Lee-Kessler fit given by Eq. (A.8), where coefficients from ref. [277] are used.

$$\Delta h_{vap,j} = [7.08(1 - \bar{T}_{b,r,j})^{0.354} + 10.95 \omega_j (1 - \bar{T}_{b,r,j})^{0.456}] T_{crit,j} R \quad (\text{A.8})$$

Intensive internal energies are calculated from the thermodynamic relation $h = u + P/\rho$. Liquid internal energies are calculated from Eq. (A.9), where compressability effects are assumed to be small.

$$u_{l,j} = h_{l,j} \quad (\text{A.9})$$

Gas-phase internal energies are calculated by Eq. (A.10), where the ideal gas equation of state has been employed (i.e. $P/\rho = RT$).

$$u_{v,j} = h_{v,j} - RT \quad (\text{A.10})$$

At each time step, a secant root solver is employed to determine liquid-phase temperature from Eqs. (A.5) and (A.9) and gas-phase temperature from Eqs. (A.6)-(A.8) and (A.10).

Equation of State

The ideal gas equation of state, i.e. Eq. (A.11), is employed at each time step after species and energies to calculate pressures in each computational zone.

$$P_j = \rho_j RT \quad (\text{A.11})$$

Thus, real gas effects are neglected in the MP-MZM framework, which becomes important for fuels during vaporization.

The liquid mixture density is a function of liquid temperature, where a compressability factor is used to calculate the departure in density from the ideal gas value, i.e. Eq. (A.12), where the mixing rule suggested by Li [273] is utilized.

$$\rho_{l,mix} = \left[R \left(\sum_{j=1}^{N_{sp}} \frac{\chi_{l,j} T_{crit,j}}{P_{crit,j}} \right) Z_{mix}^{1+(1-T_{r,mix})^{0.2857}} \right]^{-1} \quad (\text{A.12})$$

The mixture departure function is evaluated based on the correlation in ref. [278], i.e. Eq. (A.13).

$$Z_{mix} = \sum_{j=1}^{N_{sp}} \chi_{l,j} (0.29056 - 0.08775\omega_j) \quad (\text{A.13})$$

The mixing rule suggested by ref. [279], i.e. Eq. (A.14), is used to calculate the mixture critical temperature.

$$T_{crit,mix} = \sum_{i=1}^{N_{sp}} \sum_{j=1}^{N_{sp}} \frac{\chi_{l,i} V_{crit,i}}{\sum_{j=1}^{N_{sp}} \chi_{l,j} V_{crit,j}} \frac{\chi_{l,j} V_{crit,j}}{\sum_{j=1}^{N_{sp}} \chi_{l,j} V_{crit,j}} (T_{crit,i} T_{crit,j})^{1/2} \quad (\text{A.14})$$

Viscosity

Gas-phase viscosities are calculated by utilizing the method of Chung et al. [280,281], i.e. Eq. (A.15), where the low-pressure formulation is extrapolated to high pressures in the MP-MZM.

$$\mu_j = 40.785 \frac{F_j^* (MW_j T)^{1/2}}{V_{crit,j}^{2/3} \Omega_j} \quad (\text{A.15})$$

In Eq. (A.15), F_j^* is a factor to account for varying molecular structures, and is given by Eq. (A.16).

$$F_j^* = 1 - 0.2756 \omega_j + 0.059035 \mu_{DP,r,j}^4 + \kappa \quad (\text{A.16})$$

The dimensionless species dipole moments $\mu_{DP,r,j}$ are calculated via Eq. (A.17), as suggested by ref. [273].

$$\mu_{DP,r,j} = 131.3 \frac{\mu_{DP,j}}{V_{crit,j} \Omega_j} \quad (\text{A.17})$$

The empirical correlation proposed by ref. [282] is used to estimate the species collision integrals, and is given by Eq. (A.18).

$$\begin{aligned} \Omega_j = & 1.16145 \left(\frac{k_b T}{\epsilon_j} \right)^{-0.14874} + 0.52487 \exp \left[-0.77320 \left(\frac{k_b T}{\epsilon_j} \right) \right] \\ & + 2.16178 \exp \left[-2.43787 \left(\frac{k_b T}{\epsilon_j} \right) \right] \end{aligned} \quad (\text{A.18})$$

Mixture viscosities are calculated via a simple mixing rule derived from kinetic gas theory, i.e. Eq. (A.19), that was proposed by ref. [283].

$$\mu_{mix} = \sum_{i=1}^{N_{sp}} \frac{\chi_i \mu_i}{\sum_{j=1}^{N_{sp}} \chi_j \eta_{i,j}} \quad (\text{A.19})$$

Where,

$$\eta_{i,j} = \frac{[1 + (\mu_i/\mu_j)^{1/2}(MW_j/MW_i)^{1/4}]^2}{[8(1 + MW_i/MW_j)]^{1/2}} \quad (\text{A.20})$$

Thermal Conductivity

The method of Chung et al. [280, 281], i.e. Eq. (A.21), is also used to calculate thermal conductivities.

$$k_j = \frac{3.75R\Psi_j\mu_jC_v}{MW_j} \quad (\text{A.21})$$

The variable Ψ_j in Eq. (A.21) is given by Eq. (A.22).

$$\Psi_j = 1 + \alpha_j \frac{0.215 + 0.28288 \alpha_j - 1.061 \beta_j + 0.26665 Z_j}{0.6366 + \beta_j Z_j + 1.061 \alpha_j \beta_j} \quad (\text{A.22})$$

The molecular parameters α_j and β_j are given by Eq. (A.23) and (A.24), respectively.

$$\alpha_j = \frac{C_{v,j}}{R} - \frac{3}{2} \quad (\text{A.23})$$

$$\beta_j = 0.7862 - 0.7109 \omega_j + 1.3168 \omega_j^2 \quad (\text{A.24})$$

Z is the number of collisions required to convert molecular rotational energy to transitional energy, and is given by Eq. (A.25).

$$Z_j = 2.0 + 10.5 T_{r,j}^2 \quad (\text{A.25})$$

Gas mixture thermal conductivity is evaluated using the Wassiljewa mixing

rule, i.e. Eq. (A.26), with the Mason and Saxena modification, i.e. Eq. (A.27), [273].

$$k_{mix} = \sum_{i=1}^{N_{sp}} \frac{\chi_i k_i}{\sum_{j=1}^{N_{sp}} \chi_j A_{ij}} \quad (\text{A.26})$$

$$A_{ij} = \frac{[1 + (k_{tr,i}/k_{tr,j})^{1/2} (MW_i/MW_j)^{1/4}]^2}{[8(1 + MW_i/MW_j)]^{1/2}} \quad (\text{A.27})$$

Diffusion Coefficient

Gas diffusion coefficients are calculated using the method of Wilke and Lee [273], given by Eq. (A.28).

$$\mathcal{D}_{ij} = \frac{[3.03 - (0.98/MW_{ij})]T^{3/2}}{MW_{ij}^{1/2} \sigma_{ij}^2 \Omega_{ij,D} P} \quad (\text{A.28})$$

Where the diffusion collision integral is estimated by the fit proposed by ref. [282], i.e. Eq. (A.29).

$$\begin{aligned} \Omega_{ij,D} = & \frac{1.06036}{\left(\frac{k_b T}{\epsilon_{ij}}\right)^{0.15610}} + \frac{0.19300}{\exp\left[0.47635 \left(\frac{k_b T}{\epsilon_{ij}}\right)\right]} + \frac{1.03587}{\exp\left[1.52996 \left(\frac{k_b T}{\epsilon_{ij}}\right)\right]} \\ & + \frac{1.76474}{\exp\left[3.89411 \left(\frac{k_b T}{\epsilon_{ij}}\right)\right]} \end{aligned} \quad (\text{A.29})$$

As suggested by ref. [273], the Lennard-Jones parameter σ_j is estimated from the species saturated liquid density via Eq. (A.30).

$$\sigma_j = 1.18 \rho_{b,j}^{1/3} \quad (\text{A.30})$$

Simple binary mixing rules are applied per the suggestions of ref. [273].

$$\epsilon_{ij} = (\epsilon_i \epsilon_j)^{1/2} \quad (\text{A.31})$$

$$MW_{ij} = \frac{2}{1/MW_i + 1/MW_j} \quad (\text{A.32})$$

$$\sigma_{ij} = \frac{\sigma_i + \sigma_j}{2} \quad (\text{A.33})$$

Diffusion coefficients for a single species diffusing into the gas mixture are estimated utilizing Blanc's Law [284], i.e. Eq. (A.34).

$$\mathcal{D}_{j,mix} = \left[\sum_{i \neq j}^{N_{sp}} \frac{\chi_i}{\mathcal{D}_{ij}} \right]^{-1} \quad (\text{A.34})$$